Technische Universität München
Fakultät für Chemie

Electrospun polymeric electrolytes and their use in All-Solid state batteries

Bernhard Christian Springer

Vollständiger Abdruck der von der Fakultät für Chemie der Technischen Universität München zur Erlangung eines

Doktors der Naturwissenschaften (Dr. rer. nat.)

genehmigten Dissertation.

Vorsitz: Prof. Dr. Hubert A. Gasteiger

Prüfer*innen der Dissertation:

1. Prof. Dr. Tom Nilges
2. Prof. Dr. Karl-Heinz Pettinger

Die Dissertation wurde am 18 . 07 . 2022 bei der Technischen Universität München eingereicht und durch die Fakultät für Chemie am 26 . 08 . 2022 angenommen.

„The pursuit of knowledge is hopeless and eternal. Hooray!”

Prof. Hubert J. Farnsworth, Futurama Season 6 Episode 26

Abstract

This thesis focuses on the use and development of electrospinning for manufacturing polymeric electrolytes for secondary solid-state lithium metal full cells and the electrochemical performance of these cells. Solid-state lithium metal batteries are in the focus of many researchers globally, especially due to their intrinsic advantages, e.g., enhanced safety and improved energy density compared to standard lithium-ion batteries. Unfortunately, solid electrolytes have drawbacks regarding the ion migration and conduction. Electrospinning can be one mean to improve.

In this study two different polymeric electrolyte systems are investigated.

Polyethylene oxide-based electrolytes are used to compare solution-casted and electrospun electrolytes within a lithium metal full cell set-up using different electrochemical and physical analysis methods.

Development work is carried out to achieve an optimized Polyfluoric sulfonic acid-based electrolyte in the second part of this thesis.

Kurzfassung

Diese Arbeit befasst sich hauptsächlich mit der Verwendung und Entwicklung des Elektrospinnings zur Herstellung von polymerischen Feststoffelektrolyten für sekundäre Lithiummetall-Vollzellen sowie der elektrochemischen Performance solcher Zellen. Feststoffelektrolyte-Lithiummetallzellen erregen das Interesse von Forschern weltweit, besonders aufgrund ihrer intrinsischen Vorteile, z.B. einer erhöhten Sicherheit und einer verbesserten Energiedichte verglichen mit Standard-Lithiumionen Batterien. Leider haben Feststoffelektrolyte Nachteile in Bezug auf Ionenmigration und -Leitfähigkeit. Elektrospinning kann einen Weg darstellen, dies zu verbessern

In dieser Studie werden zwei unterschiedliche polymerische Elektrolytesysteme untersucht.

Polyethyleneoxid-basierte Elektrolyte werden verwendet, um die Eigenschaften von gegossenen und elektrogesponnenen Elektrolyten in Lithiummetall-Vollzellen mithilfe verschiedener elektrochemischer und physikalischer Analytik zu untersuchen.

Es wird im zweiten Teil dieser Arbeit Entwicklungsarbeit geleistet, um einen optimierten Elektrolyten auf Polyfluorsulfonsäure-Basis zu entwickeln.

Acknowledgement

This thesis was enabled by collaboration between the Technology Centre for Energy at the University of Applied Sciences Landshut and Chair for Syntheses and Characterization of Innovative Materials at the Technical University of Munich.

I would like to thank Prof. Dr. Karl-Heinz Pettinger and Prof. Dr. Tom Nilges for their excellent guidance and the opportunity to work in their corresponding research groups. I especially appreciate the freedom and support given to realize my own research according to my fields of interest.

I want to thank Patrick Walke for his support in the experiments conducted at the facilities of the TUM chemistry department.

A special thanks to Martin Frankenberger, Alexander Dinter, Hans-Konrad Weber, Christina Toigo, René Müller, Victoria Peterbauer, Katharina Pfefferl, Yu Xie, Jonathan Florez-Montano and further colleagues at the TZE for their support, their time invested in discussions and creating an inspiring, creative and harmonic atmosphere.

At last, I want to thank my wife Christina, my parents Othmar and Martina and my sister Rebecca for the unconditional support at any time in my life. This thesis is dedicated to you.

Contents

1. Motivation

One of the greatest challenges in modern history is posed by the climatic change. Extreme weather phenomena have been recorded with an increasing rate and have caused increased awareness towards the global warming caused by the increasing emission of greenhouse gases, such as CO_2, CH_4 and CF_4 [1]. These gases have been related to human activities since the industrial revolution. To lessen or even prevent damages to humans, infrastructure and economies, a maximum temperature increase of 1.5 °C, in reference to temperature levels before industrial revolution, has been proposed by the IPCC [1] and was adopted by the Paris agreement as an global goal [2].

To achieve this goal, emission of greenhouse gases must be reduced, especially using technologic means. Replacing fossil fuels with clean energy from renewable sources, e.g. wind or solar power, is crucial therefore. Sterchele et al. [3] discuss possible developments for energy systems in Germany to fulfill the goal of a CO_2-emission reduction of up to 95 % by the year of 2050. In this study, technical feasibility as well as social implications are studied. Two of the most important findings in this study are: 1. The climate goals can be achieved based on renewable energies from a technical point of view [3] and 2. In case wind power cannot be used in an optimal way, solar power can be a suitable substitute; this indeed leads to an increased demand for energy storage systems (values of 50 - 400 GWh_e are assumed) and higher costs [3]. According to data publicly provided by the Fraunhofer ISE institute, 52.4 % of the net public electricity generation for Germany in 2020 was already provided by renewable energy sources (see Figure 1).

Another point where a high potential for CO_2-reduction is possible is the mobility sector. Especially, battery-electrical cars play an important role in achieving the set goals. The german government aims to raise the number of electric cars to 10 million in the year 2030 [4]. According to the Kraftfahrtbundesamt (Federal Motor Transport Authority) in share of electric cars was roughly 1 % in 2018 [3].

Not only in Germany electromobility becomes more and more important. For the global electric vehicle market, McKinsey & Company assumed an annual growth of 60 % for 2015-2018. Especially in Asian markets, demand for electric cars is on the rise [5].

From these points it can be seen that energy storage plays an important role. Especially for electromobility application a high energy and power density, long battery life and low costs are desired. Lithium-Ion Batteries (LIBs) fulfill these requirements to a satisfactory level.

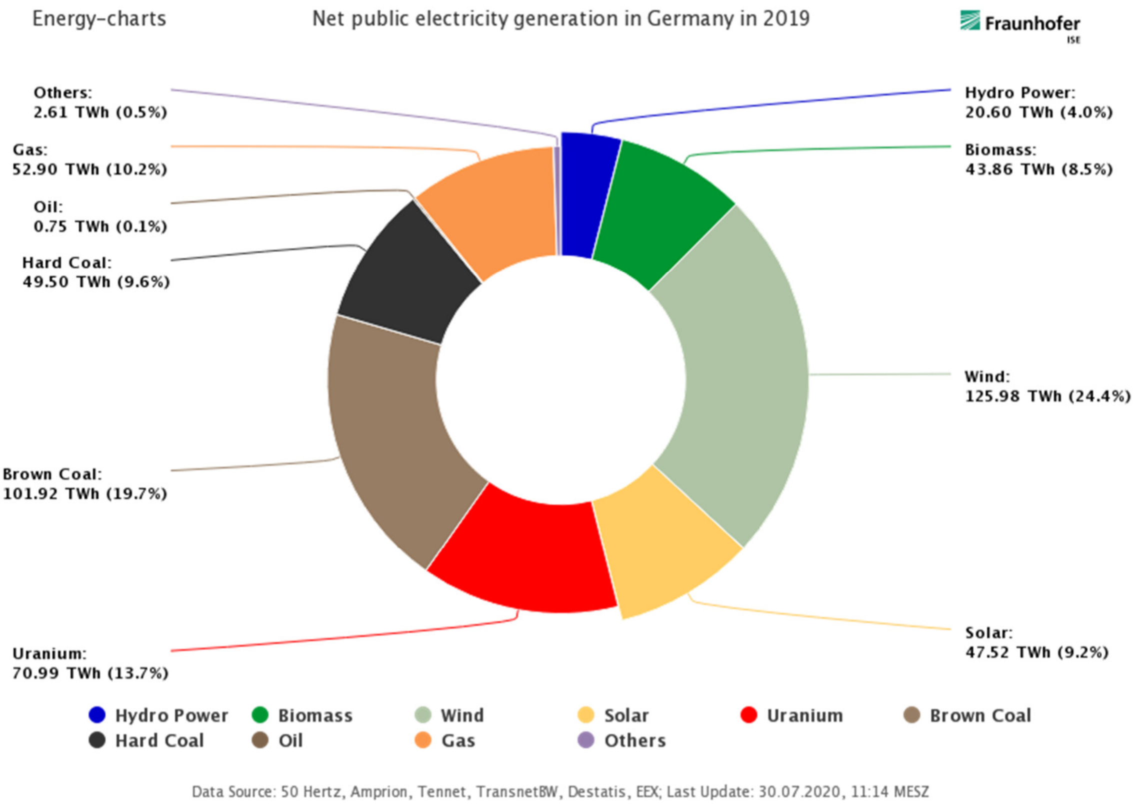

Figure 1 Net public electricity generation in Germany 2020 - Source: https://energycharts.info/charts/energy_pie/chart.htm?l=en&c=DE&year=2019

The characteristics of the element lithium explain its feasibility for electrochemical storage. With a molecular weight of 6,94 g/mol and a density of 0,53 g/cm^3 it is a very lightweight material, thus boosting high energy densities. It is the most electronegative of all metals, with a voltage of -3,04 V against the standard hydrogen electrode and therefore enables high cell voltages. Its small ionic radius enables high power densities by allowing fast (de-)intercalation reactions in electrode materials.

Approaches to lithium ion batteries date back as early as the 1970s, when first primary lithium ion batteries were assembled [6]. These batteries became popular for small, portable applications like watches or calculators. The findings of intercalation materials for electrodes enabled the manufacturing of secondary lithium ion batteries, with a first commercially available battery by Sony, market introduced in 1991 [6]. Since then, researchers all around the world are trying to improve these batteries or create new concepts based on the lithium chemistry. The importance of the lithium-ion battery was emphasized by the Nobel prize committee, awarding the 2019 Nobel prize in chemistry to John Goodenough, Stanley Whittingham and Akira Yoshino for their groundbreaking research on the field.

1.1 Advantages of All-solid-state Lithium-ion batteries (ASSBs)

Among the many interesting fields in lithium-ion battery research and development, solid state electrolytes receive an increasing interest due to its advantage over liquid or gel electrolytes. The main difference between a liquid electrolyte lithium-ion battery cell and an ASSB is the complete omission of organic solvents in the finalized ASSB cell; during manufacturing organic solvents can still be used, but all components have to be dry after assembly of the cell. This leads to an obvious improvement in cell safety, as no flammable liquids can lead to fire or build up explosive gases [7–11].

Using solid-state electrolytes can also enable new innovative cell formats and designs [11]. Another advantage compared to liquid electrolytes is an increase in energy density [7–11]. Conventional Lithium-ion batteries using intercalation electrodes are currently approaching their theoretical limit regarding specific energy and energy density [10]. One way to solve this problem is the usage of metallic lithium as an anode. This approach has also been tried for liquid electrolyte systems and it can in principle be applied [10]. These battery cells unfortunately suffer from dendrite growth resulting in short circuiting and accordingly show a poor cycling efficiency [10]. Solid electrolytes can be designed to suppress Lithium dendrite formation on metallic Lithium anodes [12].

In addition, solid electrolytes can have a selective ion mobility, meaning that only the lithium ion is mobile. This enables battery cells to have a transport number near unity [13].

Last but not least, ASSBs can have a wider operation temperature range, a long cycle life, a higher charge rate and a higher power density [10, 11].

1.2 Challenges of All-solid-state Lithium-ion batteries

Although All-solid-state lithium ion batteries receive an increased interest in the 2000s and 2010s, first approaches date back until 1957, when experiments on the ionic conductivity of Li_3N have been conducted [14]. From then, three main types of solid-state electrolytes have been developed: polymeric, inorganic, and composite electrolytes.

Research on polymeric electrolytes started, when Fenton et al. found Polyethylene oxide (PEO)/alkali-metal salts complexes are ionically conductive and Armand used these as solid polymeric electrolytes [14]. This research sparked the attempts for using solid electrolytes based on PEO.

Electrolyte	**Ionic conductivity [S/cm]**	**Source**
PEO/EC/PC/TiO_2/$LiClO_4$ (electrospun electrolyte)	$12.73 - 85.13 \times 10^{-6}$	[15]
PEO/EC/PC/TiO_2/$LiClO_4$ (solution casted electrolyte)	$6.40 - 6.80 \times 10^{-6}$	[15]
PEO/EC/MWCNT/$LiClO_4$ (electrospun electrolyte)	$9.60 - 48.00 \times 10^{-6}$	[16]
PEO/EC/MWCNT/$LiClO_4$ (solution-casted electrolyte)	11.00×10^{-6}	[16]
PEO/EC/various Li-salts (electrospun electrolyte)	$9.00 - 330.00 \times 10^{-6}$	[17]
PEO/SN/$LiBF_4$ (electrospun electrolyte)	$\sim 5 - 200.00 \times 10^{-6}$	[18]
PEO/LiTFSI (electrospun electrolyte)	$4.87 - 18.36 \times 10^{-6}$	This thesis
PEO/LiTFSI (solution-casted electrolyte)	$2.35 - 4.10 \times 10^{-6}$	This thesis

Table 1 Ionic conductivities for different PEO-based electrolytes at room temperature

The advantages of ASSBs mentioned above are very intriguing for academia as well as for industry. Nevertheless, developing ASSBs has many challenges to be solved in order commercialize the technology:

- Solid-state electrolytes suffer from a low ionic conductivity at room temperature (see Table 1) or below [14]. This is a major drawback for the technology and a huge amount of research has already been put into it. There are some methods on tackling this issue:
  - Development of new electrolyte materials for all electrolyte types [14, 19, 20]
  - Doping electrolyte materials with solid or liquid dopants (e.g. nanotubes or ionic liquids) [14, 21–23]
  - Modifying the morphology and structure of the electrolytes by special production methods [15, 16, 24, 25]

- Large interfacial resistances at the electrode-electrolyte interface pose a problem for ASSBs [14, 26]. Resolving this issue is in fact very complex, due to different possible causes for it [14, 26]. There four requirements to the electrode-electrolyte interface:
    - Physically adequate contact and contact area [14, 26]: Surface roughness of the electrodes and the electrolyte can lead to a small effective contact area. Volume changes of electrode materials during cycling can worse this effect [14]. Possible solutions to this problem depend strongly on the used type of electrolyte. For example, temperature and pressure are known to improve interfacial impedances in sulfide-based solid-state electrolytes [26]. Also, different electrode deposition techniques can be used, e.g. thin film deposition of electrodes for LiPON-based systems, but lack of scalability and cost-effectiveness [26].
    - Compatibility of electrode and electrolyte materials [14, 26]: Incompatibilities between electrode an electrolyte often result from space-charge effects, chemical or electrochemical instabilities or interdiffusion [14]. Known approaches from literature for this issue are the introduction of either a buffer layer coating or an artificial SEI [14].
    - Interfacial stress variation [14]: Stress induced by the volumetric changes of the electrodes during cycling pose a great problem for ASSBs. They can result in the loss of contact area as well as in degradation of the electrolyte and/or electrode material by formation of a new SEI layer. Introducing a layer between the interfaces can resolve this problem [14], with the advantage, that this interlayer can be engineered to resolve other problems like the incompatibilities mentioned above [14]. Another approach is to structure the electrodes or an electrode matrix [14].
    - Migration and diffusion of chemical elements [14]: The mutual diffusion of elements between the electrode and the electrolyte can result in a degradation of the interface. Solutions indicated by literature include the surface modification, e.g. by nanoparticles, and using an interlayer [14].

Electrospinning has become more and more popular in the research community and therefore there have been approaches to use in battery research. Especially the works from Freitag et al., Walke et al. and Banitaba et al. have to be mentioned here [15, 16, 18, 24, 25]. This thesis aims to deepen the understanding of the impact of the fiber morphology on the characteristics of polymeric solid-state electrolytes and their behavior in NMC_{111}/Solid-State Electrolyte/Li -Full cells. In addition, a different material combination will be optimized for the electrospinning process and tested for its feasibility as a solid-state electrolyte.

2. Theory and experimental methods

2.1 Electrospinning Background

2.1.1 Introduction

Electrospinning uses the forces of electrical fields to generate micro- to nano-fibers from solutions or melts [27]. Although patented already in 1900 by John Francis Cooley [28], it has become more popular due to the huge variety of fiber modifications and polymers possible, e.g. porous or bi-component fibers with different morphologies [27]. In general, an electrospinning set-up consists of a solution or melt reservoir, a feed towards a conductive emitter connected to a high-voltage source and a grounded collector (see Figure 2). The solution or melt is pumped from the reservoir to the emitter. The strong electrostatic forces deform the liquid into a cone shape, the so-called Taylor-Cone [27] until the surface tension is overcome and a fiber jet is formed. The jet is then guided by the electric field towards the grounded collector, forming instabilities essential for fiber elongation and diameter narrowing [27]. During the process the solvent evaporates, and dry fibers form a non-woven mat on the collector.

Correct process parameters are crucial to the characteristic of the resulting fiber mat.

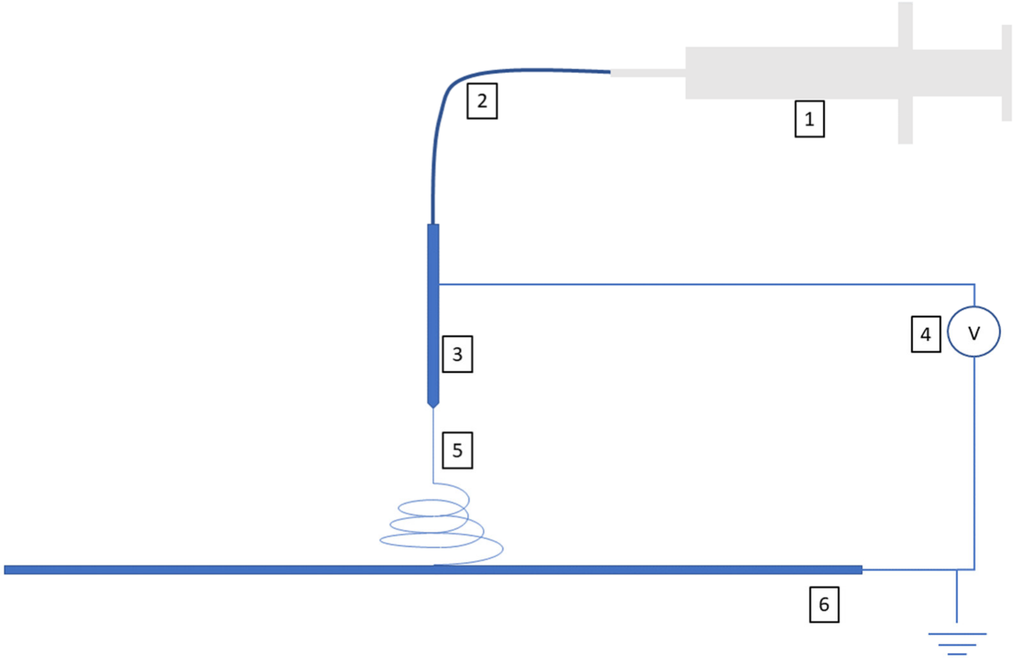

Figure 2 Schematic of a single-needle electrospinning set-up consisting of a solution or melt reservoir (1), a feed (2), a conductive needle (3) connected to a high-voltage source (4) and a grounded plate collector (6). A schematic fiber jet is also shown (5).

Important parameters are voltage, flow rate of the liquid, rheology of the solution, ambient conditions (e.g., relative humidity and temperature) and distance between emitter and collector. These are mainly machine parameters and can therefore be controlled and altered during the process. The parameters of the solution cannot be controlled during spinning and have to be chosen carefully, since the concentration, the used solvent and the dispersant (e.g. molecular weight in case of a polymer solution [27]) have a huge impact on the process and the result.

2.1.2 Application and research areas

A wide range of applications is nowadays open for the use of electrospinning mainly due to the possibility of modifying and engineering the fibers quite precisely. Some examples will be given here.

Different characteristics of the resulting fiber mats are interesting to many different research fields. The high surface-to volume ratio makes electrospinning interesting for applications like filtration, catalysis or sensors and medical applications. Even in agricultural research Electrospinning is used, for example as carrier for pesticides or fertilizers [27]. In catalysis applications fibers are often used as a support or mold for catalyst particles [27]. In medical applications electrospun fibers are often used as scaffolds for tissue engineering, wound dressings or drug-release [27].

Electrospinning also finds increasing use in energy conversion and storage applications [29–34]. Especially for fuel cells and photovoltaics electrospinning shows application potential by providing fibrous materials in an easy way, e.g. in form of electrospun electrocatalyst or separator membranes in fuel cells [31, 33, 35].

Energy storage systems show a great application potential, too. Besides supercapacitors, batteries provide a growing playground for electrospinning applications [31, 33, 36]. Lithium-ion batteries, as one of the most popular storage systems, and their derivates like lithium-sulfur or lithium-air batteries are in the scope of researchers to be improved using electrospinning technology [31, 33]. For LIBs using liquid electrolytes, cathodes, anodes and separators have been manufactured or modified using electrospinning technique [29, 31, 33, 37–42]. Some research is presented here:

- Cathodes: Various materials have been studied as electrospun cathode candidates, like $LiCoO_2$, NMC_{111} and LiFeO [29, 31, 43]. In addition, a variety of fiber morphologies (e.g. hollow, co-axial and porous) have been tested [29]. The electrospun cathodes showed improvements on terms of rate capabilities, reversibility and cycling performance [29, 31, 43] proving electrospinning to be beneficial to battery manufacturing.
- Anodes: Nanofibrous anodes have been in use for some time, although they show disadvantages like a low energy density and rate capability [31]. Research has targeted these issues using different electrospinning methods (e.g. coaxial electrospinning [29, 31]), modifications of the materials afterwards (e.g. thermal treatment [29, 31]) and addition of defects [31] or nanoparticles (e.g. Nano-Si-particles [29, 43]).
- Separators: Due to the intrinsic high surface area and pore sizes, the use of electrospun separators can tackle the problems of separator wettability and ionic conductivity [29]. Furthermore, electrospinning allows to modify the resulting separators to improve thermal stability [29].

Electrospinning was also used to manufacture different solid-state electrolytes. Especially the works of Freitag et al., Walke et al. and Banitaba et al. have to be mentioned here [15–18, 24, 25, 44].

2.1.3 Challenges

The rise of the electrospinning technique in many different fields leads consecutively to many different challenges according to these fields. Nevertheless, most there are general problems to be faced for all applications of the technique. Therefore, in this subchapter only general challenges regarding the electrospinning will be presented.

The first general problem is the finding a suitable solution. Although this problem seems to be quite individual to the specific application, it is to be solved for all. In this thesis this problem will be clarified for one specific solution.

The second challenge is a problem especially in the scope of industrializing electrospinning. Electrospinning, in case of a standard single needle, is a very slow process. Dry fiber deposition of 0,01-0,1 g/h [27] is normal for this process. Therefore, speeding up the process is of strong interest. There are basically three ways to resolve this challenge. One the one hand it is possible to used multiple emitters of one kind, e.g., an array of needle emitters. This is an easy approach, but it has some drawbacks e.g. influencing the electric field different emitter concepts [27]. A small choice of emitter concepts is mentioned in Table 2, along with the reported dry fiber deposition rates.

Emitter Concept	Dry Fiber Deposition Rate	Source
Rotating cylinder in solution reservoir	30 g/h	[45]
Rotating cone	600 g/h	[46]
Rotating disc in solution reservoir	~11 g/h	[47]
Rotating spiral coil in solution reservoir	23 g/h	[47]
Twisted wire spinneret (wire axis vertical, solution fed by gravity)	~1 g/h	[48]
Tilted plate edge	0.27 g/h	[49]
Bowl edge	Up to 0.684 g/h	[50]
Carrier-fed wire spinneret	~1.2 g/h	[51]

Table 2 Comparison of dry fiber depositions rates for various emitter concepts

This challenge was also in the scope of the „SpinnAP" project at the HAW Landshut parallel to this thesis. Here a rotating cone emitter was designed and tested, similar to what Lu et al. have published [46]. Especially for solid electrolyte applications, which require a certain thickness of the electrolyte to prevent cell failures, a fast and reliable emitter concept is of great interest in possible later industrial applications.

2.2 Materials of different battery components

2.2.1 Electrode materials

2.2.1.1 Cathode material

Requirements for modern cathode materials are highly complex and diverse. The material's crystal lattices must be stable in both lithiated and delithiated states, a high specific capacity must be reached, and the materials must have a high potential against lithium metal. In addition, safety during battery operation must be provided and production costs must be low.

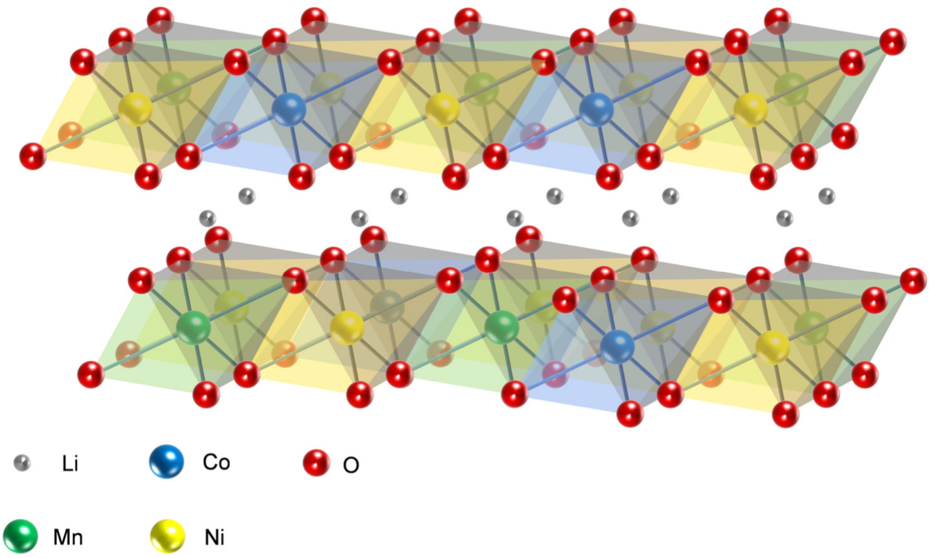

Figure 3 NMC 111 crystal lattice

A materials class which is up to task are transition metals-based crystal structures. Examples for materials of this class used in modern battery application are $LiCoO_2$ (LCO), $LiNiO_2$ (LNO), $LiNi_xCo_yAl_{1-x-y}O_2$ (NCA) and $LiNi_xMn_yCo_{1-x-y}O_2$ (NMC or NCM). Especially NMC and its stochiometric derivatives are in the focus of research and industry interest [52]. NMC combines three transition metals and their advantages as cathode materials: Ni provides a high capacity, Co and Mn provide safety and structural stability of the crystal lattice [6, 52]. The first NMC material available in commercial battery cells was NMC_{111}, which was already quite successful [52]. In order to achieve the above-mentioned targets with such a material, nickel-rich NMC (NMC_{532}, NMC_{622} and NMC_{811}) derivates have been developed [6, 52]. NMC_{111} shows a layered crystal structure (see Figure 3) which benefits the transport of lithium with the active material [53]. In comparison to an olivine structure, e.g. for $LiFePO_4$, diffusion pathways can be found in two dimensions and therefore the activation energy for the ion transport is reduced [53].

The main disadvantages of NMC materials are the health hazard posed by the active materials, possible thermal runaway and the use of cobalt with all the socio-economic indications coming alongside [54].

2.2.1.2 Conductive additives

Layered oxide materials like NMC_{111} often show a limited electronic conductivity [55, 56], leading to a decrease in battery performance [57–59]. To tackled this problem, active materials are often used in small particle sizes, covered by a functionalized coating or conductive additives are used [59–63]. A commonly used conductive additive is carbon black. It provides a high electronic conductivity and a high surface area [64]. The high surface area leads to high viscosities of the prepared slurries and therefore a suitable mixing procedure with high shear forces has to be chosen [64]. The viscosity also impacts the production techniques of the electrodes, e.g. coating of the slurry onto a metal current collector. To ease difficulties due to high slurry viscosities, a mixture of conductive additives and therefore a mixture of different particle sizes can be used [64].

2.2.1.3 Anode material

Central requirements to anode materials are low electrochemical potentials, a high specific capacity and safety during use of the battery cell. Lithium metal anodes fulfill the first two requirements par excellence with a specific capacity of 3860 mAh/g and the lowest negative electrochemical potential of -3.04 V against the standard hydrogen electrode, it shows enormous electropositivity even in non-aqueous systems [65]. Unfortunately, lithium metal anodes have shown severe safety issues in regard of the use in liquid as well as solid electrolyte battery cells mainly resulting from the high reactivity of lithium metal [10, 65–70]. The main safety problem arising from lithium metal anodes is the dendrite formation during charging, both for liquid and solid electrolytes; therefore, this poses a great challenge for researchers around the globe [10, 65–67, 69–83]. As already mentioned, solid electrolytes show lithium dendrite growth too [75, 79, 81, 84–86]. Therefore, improvements are desired. The research done on this intriguing topic has also brought upon some promising approaches, which will be mentioned in the following:

- Electrolyte additives for liquid electrolytes [65]
- Artificial SEI for liquid electrolytes [65, 85]
- Reduction of the interfacial resistance [85]
- Nanostructured liquid and solid electrolytes or anodes [65, 85]

2.2.2 Polymeric electrolytes

The advantages and challenges of ASSBs have been discussed earlier (see chapter 1), also mentioning the three general categories of solid electrolytes: polymeric, inorganic and hybrid electrolytes.

This thesis focuses on the use of polymeric electrolytes in lithium-ion metal anode cells, particularly on the effect of full-cell performance for electrospun polymeric electrolyte cells. A detailed description of all educts, methods and compositions can be found in chapters 2.3 and 2.4.

According to Agarwal et al., polymeric electrolytes can be classified into five basic categories [87]:

- *Conventional or dry polymer-salt complexes*: This class is restricted to polymers with the capability of complexing or dissolving lithium salts.
- *Plasticized polymer-salt complexes*: This class shows an enhanced ionic conductivity using plasticizers, with disadvantages to the mechanical and chemical stability.
- *Polymer gel electrolytes*: In difference to plasticized polymer-salt complexes, this class incorporates liquid electrolytes for an enhanced ionic conductivity, with the same disadvantages.
- *Rubbery electrolytes*: This class differentiates tremendously from before-mentioned classes, since the amount of salt exceeds the amount of polymer, bearing the risk of crystallization and thus losing their ionic conductivity; in the first three classes mentioned before, the main component is the polymer.
- *Composite electrolytes*: Composite electrolytes are primarily polymer-salt complexes with a small amount of inorganic filler involved. These fillers are intended to enhance both mechanical stability and ionic conductivity.

In this thesis, polymeric solid electrolytes are referred to conventional or dry polymer-salt complexes.

2.2.2.1 Polyethylene Oxide-based electrolytes

Polyethylene oxide-based solid state electrolytes are among the most investigated and used in contemporary polymeric solid state electrolytes [14, 88], mainly due to their early discovery in the 1970s [89] and their compliance to the main requirements for solid electrolytes [88]. Thanks to the polar nature of its backbone, PEO is capable of complexing lithium salts [89, 90]. In addition, the low glass transition temperature ensures flexibility of the PEO chains, allowing to transport lithium ions along and across the chains [90, 91]. In addition, PEO shows an satisfactory electrochemical stability against lithium metal [88]; against high-voltage cathode materials (more than 4 V against lithium), PEO can be problematic, sparking research efforts to develop solutions [92]. Other commonly known disadvantages of PEO that hinder its use as a polymeric electrolyte are its low transference number at room temperature [88, 93, 94] and its tendency to partially crystallize at room temperature, leading to a decreased ionic conductivity [88] and inspiring research ambitions. Some approaches will be mentioned in the following.

There are a variety of approaches to improve PEO as a polymeric electrolyte; the range goes from modifications on the molecular level to structuring the material on meso- and microscopic levels [15–18, 24, 25, 44, 88]. Most common approaches are:

- *Copolymerization*: It can be used to add mechanical strength and/or decrease the crystallinity of the PEO matrix and improve the ionic conductivity by grafting two polymer chains with special characteristics together [88, 95].
- *Crosslinking*: In contrast to copolymerization, crosslinking does not involve a second polymer but rather the same polymers and crosslinking agents. The aims of the two methods are the same [88].
- *Hyperbranching*: This method targets the crystallinity of the polymers and shows the potential to greatly reduced it, leading to an immense improvement of ionic conductivity [88]. It is sometime combined with crosslinking [88].
- *Blending*: It is one of the simplest approaches to suppress the crystallinity in polymers. Unfortunately, indentations in terms of mechanical stability have to be accepted [88].
- *Composite electrolytes*: Adding inorganic particles to the corresponding polymer electrolytes has been one of the most used methods to tune electrolyte characteristics [44, 88, 96–106]. Advantages are the improvement of ionic conductivity and mechanical strength without losses in terms of mechanical flexibility.
- *Structuring of the electrolyte*: Structuring the electrolyte can take place on different levels: meso- and microscopic. On mesoscopic level, structuring can often be found as an side effect of copolymerization or blending [107]. Structuring the electrolyte on a microscopic level is a more recent approach, often combined with electrospinning [15–18, 24, 25, 44].

2.2.2.2 Perfluorosulfonic Acid-based electrolytes (PFSA)

Perfluorosulfonic acid, also used in Nafion®, finds most most of its applications in fuel cells [108, 109]. The idea behind using PFSA derivates as electrolytes in lithium ion cells lies within the transference number. Polymers like PEO have quite low transference numbers due to the mobility of the anion, as mentioned above. PFSA and Nafion®, both ionomeres and ion exchange materials are able to reduce the mobility of the anions within the electrolyte, thus increasing the transference numbers dramatically [110].During the early 2000s, first attempts on using PFSA in lithium ion batteries have been conducted [111]. Liang et al. used lithiated Nafion® swollen with different carbonates to use as an separator/electrolyte system within LCO/PFSA/Li cells [111]. Results for reported for lithium-sulfur batteries also indicate a reduction of lithium dendrites due to the single-ion conducting nature of PFSA-based electrolytes [112]. It has to be noted, that most applications of PFSA in lithium-based battery chemistries rely on swelling the polymer electrolyte in organic solvents [110–114].

2.3 Cell component production and assembly

2.3.1 Machines

2.3.1.1 Laboratory electrode coater

Figure 4 Laboratory coating machine used in this thesis

The laboratory coating machine used to coat the electrodes is shown in Figure 4. It consists mainly of the following parts:

- Braked unwinder: The substrate foils are placed on a mechanically braked axle. The braking force is adjusted using a screw.
- Dancer roll: This is used to ensure a constant tensile force on the substrate during coating
- Doctor blade: An adjustable slit ensures a homogenous coating of the slurry on the substrate
- Drying tunnel: It contains four individually controlled heating plates. In this thesis the first two and the last two heating plates are set to same respective temperatures. A flue attached to the drying tunnel takes the solvent fumes outside.
- Track edge control
- Winding drive: Here a core is inserted to a driven axle to wind the electrode to a coil. The substrate speed is controlled this device.

With this machine the most important process parameters can be adjusted: Tensile force of the substrate, coating slit and drying temperatures and times.

2.3.1.2 Electrospinning machine

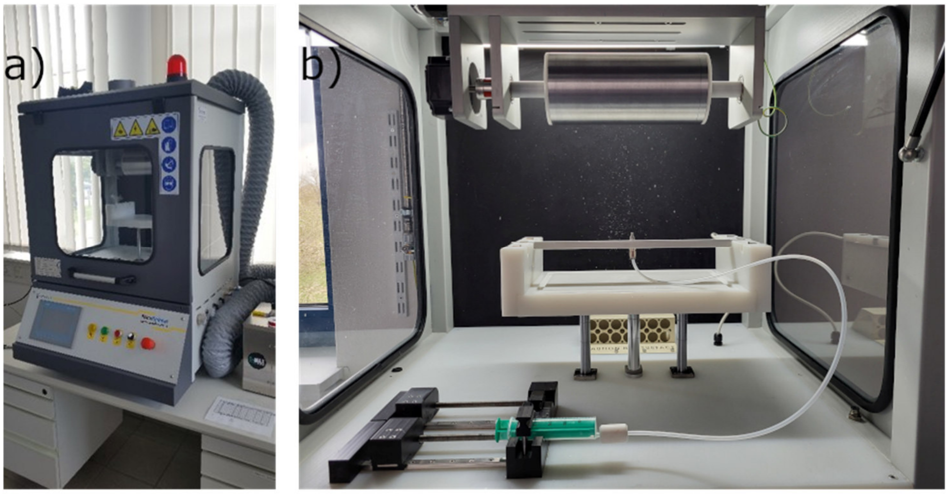

Figure 5 a) Electrospinning machine Inovenso NE-300XP b) Spinning chamber

All electrospinning experiments in this thesis are conducted on an Inovenso NE-300XP (see Figure 5). This laboratory machine allows to produce fibers with various modifications and morphologies. The most important parts are:

- Syringe pumps: The machine features two syringe pumps; it is therefore possible to spin two solutions simultaneously. The feed rate can be controlled for both individually and is corrected for the used syringe type.
- Emitter portal: The portal is used to adjust the Emitter-Collector distance. It is corrected for different Emitter types (e.g., Nozzles, medical syringe tips, Core-Shell-Nozzle) as well as for different collector types. In this thesis, only nozzle emitters and the drum collector are used; this leads to a distance range from 32 up to 200 mm. Nine nozzles can be equipped at maximum. The voltage is applied to the nozzles and can reach 40 kV at maximum; the collector portal is grounded and has no voltage applied.
- Collector portal: The portal can be equipped with several collectors (Drum collector, plate collector, vacuum plate collector, Rotating-axle-collector). Only the drum collector is used in this thesis. The drum can rotate at 100 rpm up to 500 rpm. To ensure a more homogeneous fiber coating, the portal can be moved perpendicular to the rotation direction; the range for movement is from 5 to 120 mm at a speed ranging from 2 to 15 mm/s.

- Humidity control system: The humidity inside the chamber can be adjusted to values between 20 and 100 % relative humidity. It is controlled by a humidity sensor inside the chamber. In relation to the adjusted and the measured value, a dehumidifier is activated when the humidity inside the chamber exceeds to set limit.

2.3.1.3 Laminator

Figure 6 Roll laminator BLE 282 D

All lamination processes in the framework of this thesis have been conducted with the roll laminator shown in Figure 6. It mainly consists of the following parts:

- Stainless steel bands: These bands move the samples through the heating areas to the lamination rolls. The band speed ranges from 0.023 to 0.230 m/s
- Heating elements: Each band track (upper and lower) features three heating plates (six in total). These can be controlled individually up to 160°C using PID controllers.
- Lamination rolls: The lamination rolls sit behind the last heating plate on both band tracks. The distance between the rolls can be adjusted manually. The line force exerted on the sample by the rolls can be adjusted manually with two screws, one on each side of the lower band track. The force is measured by two scales in kg, one for each side of the band track.

2.3.2 Educts

Solids		
$LiNi_{1/3}Mn_{1/3}Co_{1/3}O_2$	NM-3102h	BASF TODA America, *USA*
Carbon black	Super C65	Imerys, *Switzerland*
Polyethylene Oxide	PEO M_n = 300000	Sigma Aldrich, *Germany*
Lithium bis(trifluoromethanesulfonyl)imide	LiTFSI	Sigma Aldrich, *Germany*
Polyvinyldene difluoride	Solef® 5130	Solvay, *Italy*
Lithium	Li-foil 0.4 mm	Gelon LIB, *China*
Perfluorosulfonic Acid	PFSA 725 EW	3M Dyneon, *Germany*
Liquids		
N-methyl-pyrrolidone	NMP	Overlack, *Germany*
Acetonitrile	Acetonitrile	Sigma Aldrich, *Germany*
Ethanol	Ethanol	Sigma Aldrich, *Germany*
Deionized water	Deionized water	-
Gases		
Argon	Argon 5.0	Westfalen, *Germany*

Table 3 Educts used in this thesis

All educts used for electrode and electrolyte production in this thesis can be found in Table 3.

2.3.3 Electrode preparation

Solid-state cathode			
Material	Purpose	Percentage	Mass [g]
NMC_{111}	Active cathode material	75.13 wt%	68.00
PEO	Ion-conductive matrix	8.41 wt%	7.61
PVDF	Adhesion additve	2.53 wt%	2.29
Super C65	Electronic conduction additive	9.94 wt%	9.00
LiTFSI	Ion-conduction additive	3.99 wt%	3.61
NMP	Solvent	-	180.24

Table 4 Cathode composition

Electrodes have to fulfill diverse requirements for the use in battery cells; for electrodes in liquid electrolyte cells, adhesion to the current collector, cohesion within the electrode coating and electronic conductivity are the most important. In case of solid-state electrolyte, the electrodes must be redesigned, since the requirement of ionic conductivity has to be

Solid-state cathode mixing

Step	Added material	Mass [g]	Mixing/Degassing speed [rpm]	Mixing/Degassing /Cooling time [min]
Premixing	Stock solution	180.24	2000	0.5
Mixing	Super C65	9.00	2000	2
Degassing	-	-	2000	1
Mixing	LiTFSI	22341	2000	2
Degassing	-	-	2000	1
Mixing	-	-	2000	2
Degassing	-	-	2000	1
Mixing	-	-	2000	2
Degassing	-	-	2000	1
Mixing	NMC111	68.00	2000	2
Degassing	-	-	2000	1
Cooling	-	-	-	90
Mixing	-	-	2000	2
Degassing	-	-	2000	1
Cooling	-	-	-	10
Mixing	-	-	2000	2
Degassing	-	-	2000	1
Cooling	-	-	-	10
Mixing	-	-	2000	2
Degassing	-	-	2000	1
Cooling	-	-	-	10
Mixing	-	-	2000	2
Degassing	-	-	2000	1
Cooling	-	-	-	10
Mixing	-	-	2000	2
Degassing	-	-	2000	1
Cooling	-	-	-	10
Mixing	-	-	2000	2
Degassing	-	-	2000	1
Cooling	-	-	-	10
Mixing	-	-	2000	2
Degassing	-	-	2000	1
Cooling	-	-	-	10

added due to the lack of a liquid electrolyte within the pores of the electrode. To meet this requirement, composite electrodes consisting or the active materials dispersed in an solid-state ionic conductive matrix are often used [115–117].

Additionally, it is necessary to prevent agglomerates to ensure a good electrode quality during coating. Therefore, a mixing method with high energy input is needed.

All electrodes used in this thesis have been prepared using a planetary mixer (ARE-250, Thinky, *USA*), all electrodes used have been prepared from one batch of electrode slurry and have been coated in one continuous procedure. The compositions of the electrode slurry can be found in Table 4.

After weighing the materials into the mixing cup, a stock solution using polyethylene oxide, LiTFSI and NMP was added. This solution was prepared a day in advance, consisted from 2.28 g PVDF, 7.61 g PEO and 120.04 g NMP and was stirred at 120°C under reflux overnight.

A full description of the sequential steps for slurry preparation can be found in Table 5.

After degassing the slurry and checking for agglomerates, the electrode is coated using the laboratory coating machine shown in Figure 4. The coating parameters can be found in Table 6.

Coating parameter			
Gap [µm]	Coating speed [mm/s]	Drying tunnel temperature 1 [°C] / Length [m]	Drying tunnel temperature 2 [°C] / Length [m]
200	4.0	135 / 1.20	150 / 1.20

Table 6 Coating parameters

2.3.4 Electrolyte preparation

PEO stock solution composition			
Material	Purpose	Percentage	Mass [g]
PEO	Ion-conductive matrix	11.81 wt%	68.18
LiTFSI	Ion-conduction additive	1.59 wt%	9.16
Acetonitrile	Solvent	86.60 wt%	499.99

Table 7 PEO stock solution composition

The solid electrolytes used in this thesis are all polymer-based. Ceramic electrolytes are not considered in this thesis but may be in future research (see “Future research aspects regarding ASSBs”). Two materials are used as ionic conductors: Polyethylene Oxide and Perfluorosulfonic acid.

Polyethylene Oxide is one of the most known and used polymeric ion conductors (see Polymeric electrolytes”). Many different formulations for PEO-based, spinnable solutions are known from literature [15–18, 24, 44]. Unfortunately, these solutions are mostly coupled to the electrospinning setup used for the respective research, e.g., the tubing diameter can pose as a bottleneck for the solution viscosity. Therefore, the solution composition used in this thesis may be similar to literature [18, 24] but had to be adapted for the use to spinning setup (NE-300XP, Inovenso, *USA*) shown in Figure 5. The used stock solution composition can be found in Table 7.

The LiTFSI content was chosen to equal one lithium ion per ten ethylene oxide monomers. The stock solution composition was also chosen to be similar in lithium content to the ion conductive matrix used in the cathode to prevent ion migration driven by a concentration gradient.

Interlayer spinning parameters	
Parameter	Value
Syringe	BD20
Nozzle type	Single nozzle
Drum collector rotational speed	400 rpm
Travel homogenization portal	80 mm
Speed homogenization portal	2 mm/s
Voltage	30 kV
rel. Humidity	0,35
Flow rate	0,8 ml/h
Emitter-collector distance	150 mm
Effective spinning time	12 h
Temperature	room temperature (~25°C)

Table 8 Interlayer spinning parameters

For PFSA-based electrolytes, a spinnable formulation had to be conducted first. The corresponding method scheme can be found in chapter 4.2.1. As pre-tests determined, PFSA needed an additive polymer to be spinnable. For this thesis, PEO was chosen, due to its ability to dissolve lithium salt and its rather high molecular weight; the same PEO was used as for the other experiments. TFSI was used as a lithium salt. Deionized water and ethanol and mixtures between have been used as solvents, since both solvents dissolved all materials used for the experiment in a satisfactory way; for some additional spinning tests dimethyl sulfoxide was used as an aprotic alternative solvent. The solutions have been prepared under normal atmosphere and were stirred overnight in a water bath at 60°C prior to electrospinning. The parameters of the solutions can be found in Table 12.

Laminator parameters			
Feed speed [mm/s]	Temperature heating stage 1/2/3 [°C]	Line force [N/cm]	Gap [µm]
21	60/60/65	12,26	0

Table 9 Laminator parameters

Two different types of electrolytes have been prepared for this thesis: electrospun and solution-casted electrolytes.

Solution-casted electrolytes have been prepared by coating the stock solution onto a glass substrate inside an argon filled glovebox with an average water content of 0.2 ppm (MB 200 B ECO, MBraun, *Germany*) using a box-type doctor blade with a 400 µm slit. The coating must be repeated four times to achieve a dry thickness of the film of 70-80 µm. After drying for at least 24 h inside the glovebox, samples with a diameter of 15 mm have been cut out using a scalpel.

Electrospun electrolytes have been applied directly to the cathode, meaning the fiber mat was spun directly to the active coating. Prior to the actual fibrous electrolyte an interlayer is spun onto the electrodes. This interlayer is also applied to the electrodes used for solution casted electrolyte cells. The idea behind this layer is to homogenize the ion flow coming from the electrolyte fibers and form an improved interface to the cathode coating. To spin the interlayer the same stock solution as for the electrolyte is used. Interlayer spinning parameters for the electrospinning setup used (NE-300XP, Inovenso, *USA*) can be found in Table 8.

After applying the interlayer, the electrodes are laminated using a roll laminator (BLE 282 D, Manz Italy, *Italy*) shown in Figure 6. The idea behind this step is to improve the interface between the cathode coating and the interlayer and to melt the fibers to provide a thin homogeneous layer to homogenize the ion current density. Therefore, the lamination temperatures are chosen to be above the melting temperature for PEO crystallites. The parameters used on the laminator can be found in Table 9.

After the interlayer application the electrodes are stored in a Glove box under argon gas atmosphere. Electrodes meant for the use in cells with an electrospun electrolyte are further processed using the electrospinning setup shown in Figure 5 (NE-300XP, Inovenso, *USA*). The electrolyte is spun directly onto the cathode. Therefore, the cathode is attached to the drum collector of the electrospinning setup in a way that the cathode coating is central above the electrospinning emitter.

To investigate the impact of different electrospinning parameters on the electrolyte and cell characteristics, different parameter sets are defined and applied to the spinning setup. To ensure a suitable electrolyte thickness, the effective spinning time is chosen to be 24 h, divided into two spinning sessions á 12 h.

The used spinning parameters can be seen in Table 10.

Electrolyte spinning parameters		
	Electrode #17	**Electrode #18**
Syringe	BD20	
Nozzle type	Single nozzle	
Drum collector rotational speed	500 rpm	
Travel homogenization portal	80 mm	
Speed homogenization portal	2 mm/s	
Voltage	20 kV	30 kV
rel. Humidity	35%	
Flow rate	0.8 ml/h	
Emitter-collector distance	150 mm	100 mm
Effective spinning time	36 h (Electrolyte+Interlayer)	
Temperature	room temperature (~25°C)	
	Electrode #21	**Electrode #24**
Syringe	BD20	
Nozzle type	Single nozzle	
Drum collector rotational speed	500 rpm	
Travel homogenization portal	80 mm	
Speed homogenization portal	2 mm/s	
Voltage	30 kV	20 kV
rel. Humidity	35%	
Flow rate	0.8 ml/h	
Emitter-collector distance	150 mm	100 mm
Effective spinning time	36 h (Electrolyte+Interlayer)	
Temperature	room temperature (~25°C)	

Table 10 Spinning parameters for electrolytes

PFSA-based solutions spinning parameters	
Parameter	**Value**
Syringe	BD20
Nozzle type	Single nozzle
Drum collector rotational speed	500 rpm
Travel homogenization portal	0 mm
Speed homogenization portal	0 mm/s
Voltage	10,20,30 kV
rel. Humidity	35%
Flow rate	Variable, dependent on solution viscosity
Emitter-collector distance	100,150,200 mm
Effective spinning time	10 min
Temperature	room temperature (~25°C)

Table 11 Spinning parameters for PFSA-based solution electrospinning experiments

For PFSA-based spinning solutions a suitable set of parameters must be determined first. Therefore, a variation of voltages, distances and drum collector rotational speeds have been combined and tested. The corresponding parameter matrix is shown in Table 11.

2.3.5 Used cell formats and their assembly

Another important factor for the commercial success of lithium-ion batteries is the wide range of possible cell formats. Lithium-ion batteries can be assembled in different ways and come in a variety of casings. The main categories of casings are [6]:

- Cylindric cells: These casings can be found for many different applications on the market, e.g. Laptops, PHEVs, EVs or power tools
- Prismatic cells: Prismatic casings can be found in mobile electronics, e.g., cell phones
    - Rigid casings
    - Flexible casings, e.g., Pouch-casings
- Coin-Cells: These are especially used for small electronics, e.g., in small remote controls; mostly these cells are primary cells

In scientific research, many other different casings are known for special experimental applications, e.g. in-situ measurements in scanning electron microscopes or scattering experiments [118].

Due to experimental limitations, this thesis uses small battery casings like coin cells and T-cells.

2.3.4.1 Coin cells

For cycling experiments and impedance measurements coin cells of the format CR2032 have been used. This cell format is very well known, both in scientific research as well as for commercial cells powering small electronic devices.

Coin cells show some advantages against T- and Pouch cells in regard for this thesis. In comparison to pouch cells, the use of lithium metal anode is easily implemented while pouch cells must be optimized, especially for the use of electrospun electrolytes (see subchapter 6.2.6).

T-cells (see Figure 50) have this advantage too. Unfortunately, first experiments with electrospun electrolytes used in T-cells showed, especially for higher cycle numbers, not satisfactory data quality; this finding is in strong contrast to the data quality achieved for cyclovoltammetry. In addition, T-cells using an electrospun electrolyte showed a higher number of cell failures before or during early stages of electrochemical testing, a problem solved nearly immediately after switching to coin cells.

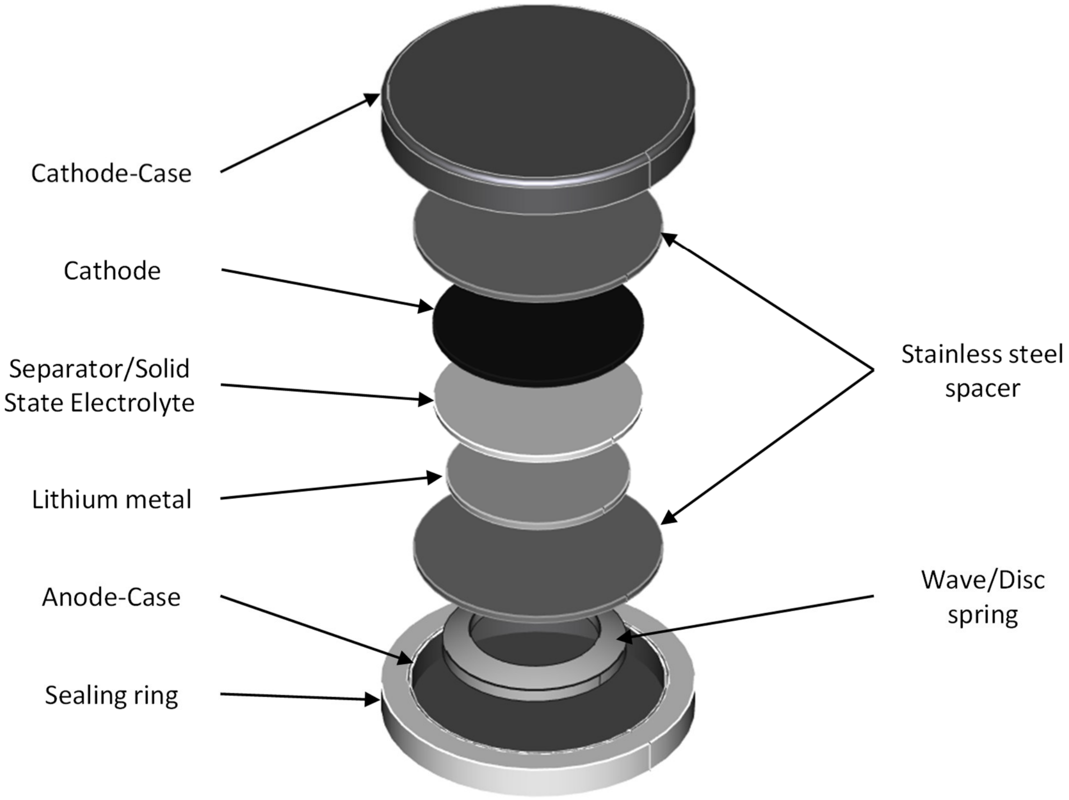

Figure 7 Exploded view schematic of a Coin Cell used in this thesis

One question to be asked when using coin cell setup with electrospun electrolyte is the mechanical pressure to the cell components and a possible destruction of the fibers. To check this problem, some cells have been opened under argon atmosphere and the electrolyte has been probed under a microscope. No change induced by the pressing force has been found.

A schematic of the used setup is shown in Figure 7. The cells consist of a cathode and an anode casing to contact the cell electrically. The anode casing is additionally surrounded by a polymeric sealing ring. On the anode side of the cell, a wave spring is placed to provide slight pressure and electrical contact to both the anode casing as well as the cell on the anode side. On each side a stainless-steel spacer with a thickness of 0.5 mm is used to ensure a homogeneous pressure and electrical contact to the cell components. In between the spacers, the cell consisting of a lithium metal anode, the electrolyte (solution casted or electrospun) and the cathode is placed.

2.4 Analysis techniques

2.4.1 Scanning Electron Microscopy (SEM)

It has become obvious that for a detailed insight on the fiber morphology, a more sophisticated method has to be used. For this case SEM is the method of choice.
Scanning Electron Microscopy utilizes, in difference to optical microscopy, electrons instead of photons. The wavelength of the electrons is then defined by

$$\lambda = \frac{h}{\sqrt{2m_e \cdot e \cdot U_a}} \qquad \textit{Eq. 1}$$

where λ are the wavelength, m_e the mass of the electron, h is the Planck's constant and U_a is the acceleration voltage. Since the Abbe-limit is also valid for other types of radiation, it is possible to distinguish finer fiber features, e.g. pores on the fiber surfaces or embedded nanoparticles.

2.4.2 Electrochemical impedance spectroscopy (EIS)

In research on batteries and other electrochemical appliances like fuel cells interest is focused on analytical methods for probing bulk materials as well as interfaces (both solid-solid and solid-liquid). Therefore, it is only logical that electrochemical impedance spectroscopy has gained more interest, since it can provide insights to the above-mentioned points. In addition, EIS can be applied to a great range of materials, regardless of their properties: liquids and solids, ionically, electronically or mixed conductive, semi-conductive and insulating [119].
Due to these characteristics, EIS becomes a standard method for research in many fields, especially in all-solid-state battery (ASSB) research. In this specific application interest often lies within the question of the ionic bulk conductivity of the solid electrolytes as well as in the different interface resistances inside an ASSB (e.g. interfacial resistances between cathode and the electrolyte).
There are several variants to the EIS measurement [119]. The first approach is to simply apply a voltage step and measure the corresponding time-dependent current. This quite easy method yields one problem: to switch from a time-dependent regime to a frequency dependent (which is the usual definition for impedance), a Fourier- or Laplace

transformation has to be applied. These transformation leads to a distortion of the result, since the signal was not periodic. It has to be corrected in by windowing and therefore the desired frequency range may not be fully probed in a sufficient way [119].

The second method is to apply white noise as a signal and again measure the current response of the system. The white noise signal leads to less distortions when transformed in the frequency domain and, since nearly all frequencies can be applied at once, data gathering is quite fast. The disadvantage of this method is to generate true white noise. In addition, the signal-to-noise ratio might be not sufficient [119].

The most common method is applying a single frequency signal to the sample and measure the response. This approach possesses the best signal-to-noise ratio and single frequency signals can be easily produced. Therefore, many different experimental instruments using this method are readily available and are most user friendly [119].

Given a single-frequency voltage signal and its corresponding response [119]:

$v(t) = V_0 \cdot \sin(\omega \cdot t)$, with $\omega = \nu \cdot 2\pi$	*Eq. 2*
$i(t) = I_0 \cdot \sin(\omega \cdot t + \theta)$, with $\omega = \nu \cdot 2\pi$	*Eq. 3*

The phase shift between the voltage and the current signal is denominated θ, ν is the applied frequency. Depending on the on the system of interest, time derivatives of these equations form a differential equation system that has to be solved. Using Fourier-transformation, these equation systems can be simplified. From there a correlation between voltage and current can be made, similar to Ohm’s law, and hereby define the impedance [119]:

$Z(i \cdot \omega) = \frac{F\{v(t)\}}{F\{i(t)\}}, F\{\,\}: Fourier - Transformation$	*Eq. 4*

The impedance, mostly used as a complex quantity, can then be written as such [119]:

$Z(\omega) = Re(Z) + i \cdot Im(Z)\ , Re(Z) = \lvert Z \rvert \cdot \cos\theta\ , Im(Z) = \lvert Z \rvert \cdot \sin\theta$	*Eq. 5*

To further characterize the system measured by impedance, it is a common method to develop an equivalent circuit model and fit the parameters according to the experimental data. To build such models, combinations of circuit elements can be used. Some of the most known elements are: resistances (R), capacitances (C), inductances (L) and constant phase elements (CPE) [119]. Constant phase elements pose as a non-ideal variant of capacitances and are quite useful in modelling battery applications.

2.4.3 Charge/Discharge cycling

Cycling tests play an important role in characterizing and testing a battery cell. The exact details of testing procedures depend strongly on the aim of the corresponding research interest. In general, cycling tests consist of cycles, which are sequences of charging, discharging and pauses, repeated for either a certain amount of time or for a defined number of cycles. The data measured are the cell voltage, the current and sometimes the temperature of the cell housing. An example of a typical voltage and current curve over time for a cycle is shown in Figure 8.

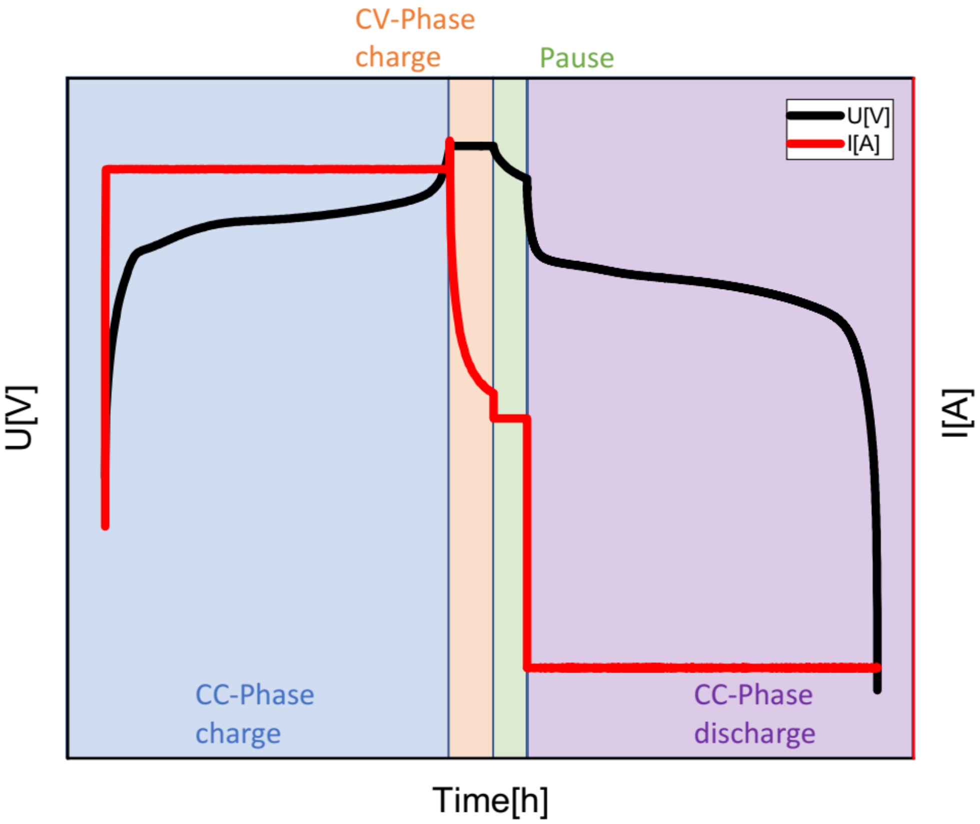

Figure 8 Exemplary Charge/Discharge cycle

The constant current (CC) phase at the beginning is very sensitive to the chemistry of the cathode and can deliver interesting data on it [6]. It is followed by a constant voltage (CV) phase, to fully ensure a state-of-charge (SOC) of 100 %. Afterwards, a short pause is added, to enable the cell to reach its relaxation voltage and to be able to calculate the internal resistance of the cell from the voltage drop. The pause is followed by a CV-discharge phase. From the charge and discharge phases important key figures can be derived, such as the coulombic efficiency and the discharge capacity. Further, by calculating the derivative of capacitance over voltage (dQ/dV), insights into the electrochemical reactions during cycling, similar to cyclovoltammetry, can be received.

In this thesis cycling tests are used in two different ways: cycling tests and C-Rate-Tests.

During cycling tests, the key parameters of the cycles (like charging/discharging currents or cut-off voltages) remain unchanged for a high number of cycles. These tests are used in this thesis to determine aging phenomena and possible cell failures.

C-Rate-Tests are used in this thesis to determine the response of the cell system to different charging/discharging currents.

A more detailed description of the cycling and C-Rate-Tests used for this work can be found in subchapter 3.2.

3. Influence of fiber production parameters on PEO-based ASSB characteristics

3.1 Introduction

In the following chapter the influence of fiber morphology on resulting electrospun polymeric electrolyte was investigated. Therefore, a PEO/LiTFSI-solution was electrospun using different parameters which are known to influence the fiber morphology greatly. The scope was especially on the influence of the electric field. To achieve a variation in the fiber morphology, the voltage and distance between the emitter and the collector was varied (see chapter 2.3.4). Cells using a solution casted electrolyte have been produced for comparison to the electrospun electrolytes. The resulting fibers were analyzed in regard to their morphology using optical and scanning electron microscopy methods. Electrochemical characteristics have been determined using impedance measurements and electrochemical cycling, both in full cell configuration. In addition, XRD and DSC data has been taken from pristine and cycled electrodes to gain insight into the structure and crystallinity of the used electrodes.

3.2 Experimental

In this chapter, the used analyzers and their settings will be shown and discussed.

3.2.1 Scanning electron microscopy

For scanning electron microscopy, a Zeiss Merlin VP compact (Carl Zeiss Jena GmbH, Jena, Germany) with a secondary electron detector was used. The acceleration voltage for the electrons was chosen to be in the range of 1 to 1.5 kV in order to avoid electrostatic charging on the polymers. The chosen aperture size was 30 µm for all experiments. All experiments have been conducted under high vacuum.

The samples for both optical and scanning electron microscopy have been prepared under normal atmosphere, but storage as well as transport have been conducted under argon atmosphere. SEM samples have been prepared in two different ways. Electrodes have been punched out using an EL-CELL punch (EL-CELL GmbH, Hamburg, Germany) with a diameter of 14 mm; it is the same punch used for preparing electrodes for electrochemical

tests. These electrodes have then been punched using a punching iron of 10 mm diameter to fit the sample holders used in the SEM. As a reference, samples have also been punched using only the punching iron to gain insights on the effect of the EL-CELL punch on the electrolyte morphology. The SEM samples have not been subjected to sputtering.
For analyzing microscopy data freeware software Fiji and ImageJ have been used.

3.2.2 Impedance measurement

Impedance measurements have been conducted using an Autolab PGSTAT204 (Metrohm AG, Herisau, Switzerland) potentiostat. The frequency range for all PEIS experiments was set to be 100 kHz to 10 mHz. The cells were connected to the potentiostat either by a jack plug (used for T-cells) or by using a coin cell holder as shown in Figure 9.
Impedance measurements included the following steps:

1. Open circuit voltage (OCV) measurement
2. Charging the cell with a constant current of 5 µA
3. Relaxation period for two hours; accompanied with an OCV measurement
4. Impedance measurement

The charging step is meant to ensure a similar state of charge for all measured cells.
The data analysis and fitting were conducted with EC-Lab V10.44 software (Biologic, Seyssinet-Pariset, France) using its Z-Fit function.

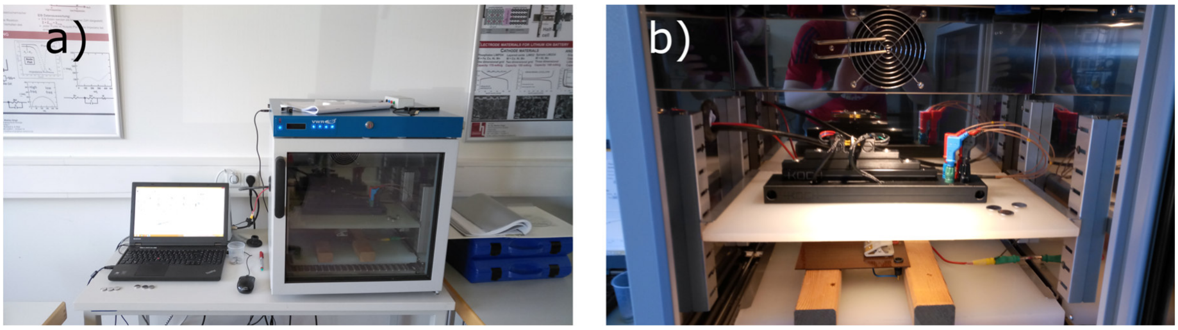

Figure 9 a) Impedance measurement equipment with temperature chamber b) Coin-cell holder used in impedance measurements within the temperature chamber

3.2.3 Electrochemical cycling

All electrochemical cycling experiments have been conducted with BaSyTec CTS-LAB test systems (BaSyTec GmbH, Asselfingen, Germany) using the corresponding control software BaSyTest V6.1.10.2 (BaSyTec GmbH, Asselfingen, Germany). Due to a system update, some data were gathered using BaSyTest V6.2.26.2 (BaSyTec GmbH, Asselfingen, Germany). The system update did not affect the gathering or the quality of the data, therefore all the data presented in this study is coherent.

Generally, the charge/discharge cycle shown in chapter 2.4.3 is implemented to the software using a subroutine. The structure of this subroutine is used in every electrochemical cycling experiment presented here. Such subroutines always have the following structure:

1. CC-charging step: The cells are charged with a constant current (I_{CC}) up to a predefined upper cut-off voltage (U_{UCV}). The voltage is measured during this step.
2. CV-charging step: The cells are held at U_{UCV} until a certain current (I_{CV}) is reached. The current is measured during this step.
3. Pause: No voltage or current are applied but both are measured.
4. CC-discharge step: The cells are discharged with a constant current (I_{DC}) until a certain lower cut-off voltage (U_{LCV}) is reached. The voltage is measured during this step.
5. Pause

All parameters for the subroutine are defined within the paramount test procedure.

For all cell tests cut-off voltages have been set to 2.5 V and 4.4 V as lower and upper cut-off voltages. Constant voltage charging was conducted until the measured current dropped below 0.1C.

As described in chapter 2.4.3, cycling and C-rate tests have been conducted. These tests followed a specific order:

1. Cycling test “Formation”: A formation of the cells has been conducted at the beginning of all electrochemical cycling testing. It consisted of three cycles (aforementioned subroutines) using the cut-off voltages mentioned above and a fixed CC-charge/discharge current of 1µA. This cycling step is meant to generate knowledge on the capacity of the cathode, which is needed to define the charging/discharging currents for all following experiments.
2. C-rate test: C-rate tests can be divided into a charge and a discharge test containing cycles with varying charge/discharge currents (0.2C, 0.5C, 1C, 2C, 3C, 5C). For charge C-rate tests the discharge current remains set to 0.2C and vice versa. This is meant to ensure a reproducible starting point for each new cycle, regardless how much capacitance was actually used in the step beforehand.

3. “Conditioning”: During first tests it became obvious that the capacity of the cells behaved in an unexpected way, especially during formation. This led to major differences in measured capacities between the different cell series. To account for this and to generate comparable data, a conditioning step was introduced. This can be seen as a second formation which is limited by the measured capacity. Therefore, all cells have the same capacity of 90 µAh after completing this step. Conditioning consists of at least 50 cycles with a fixed charge/discharge current of 5 µA. Depending on the state of the cells after the C-rate test, conditioning can take more or less than the previous mentioned cycles, but it will always end at the capacity threshold.
4. C-rate test after conditioning: Conditioning will be followed by a second C-rate test to monitor the change in rate capability caused by the conditioning step. For C-rate tests conducted after the conditioning step, additional steps are implemented after the charge and the discharge test cycles, using a fixed charge/discharge current of 5 µA; these steps are used to monitor the impact of high currents on the cells by comparing to the data gained during the conditioning.
5. Cycling test 0.35C/0.5C/1C: Independent, meaning each test is separated by an impedance measurement, cycling tests over 50 cycles with a charge/discharge current of 0.35C/0.5C/1C (equals 31.5µA/45µA/90µA) is conducted. These 50 cycles are followed by 5 cycles with a charge/discharge current of 5 µA to monitor changes compared to the starting point after conditioning.
6. End-of-test analysis: At the end of the testing procedure a conclusive impedance measurement is taken. Some few cells are also disassembled for end-of-life tests, such as XRD and measurements.

Between each step of the cycling tests an impedance measurement is conducted to monitor possible changes in the internal resistances of the cells.

All cells measured in this study have been prepared according to chapter 2.3.5.

Since some of the cycling steps require very small currents in the range of 1µA, a short discussion on the stability of the current provided by the BasyTec system will be conducted here. To gain insight into this topic, the Signal-to-Noise ratio (SNR) is calculated by dividing the mean value of the measured currents during the formation by the standard deviation of these values. This leads to SNR values in the range from 25 to 42, showing that the currents are stable enough to gain measurement signals distinct from the noise.

3.2.4 XRD

For XRD measurements a Stoe STADI P (Stoe & Cie GmbH, Darmstadt, Germany) is used. It utilizes a Ge(111)-monochromator for copper K_α radiation (λ=1.54056 Å). The diffraction signals are detected using a Dectris MYTHEN DCS 1K (Dectris AG, Baden-Daettwil, Switzerland). Samples are prepared and fixated the XRD using Magic Tape^{TM} 810 (Scotch®, Seefeld, 3M Deutschland GmbH). The diffractograms are measured with an angular resolution of 1°, measuring for 10 s per step. Overall, an angular range of 2° to 80° is covered.

3.3 Results and Discussion

3.3.1 Fiber morphology

In the following chapter the morphology of the electrospun fibers will be discussed. The used spinning parameters have been described above in Table 10 and assigned to the corresponding electrode number in the same table. Throughout this chapter it will be referred only to the aforementioned electrode numbers (see Table 10). All SEM pictures are chosen to be representative. Raw SEM data can be found in the appendix.

To further be able to recognize the impact of electrospinning the electrolyte in polymeric solid-state batteries, reference cells have been built using solution-casting method (see chapter 2.3.4). The electrodes used for these cells have been prepared exactly like the electrodes used for electrospun cell experiments, meaning these electrodes have also been treated with a laminated electrospun PEO/LiTFSI layer prior to punching and cell assembly (as described in chapter 2.3.4). The resulting electrode surface can be seen in Figure 10.

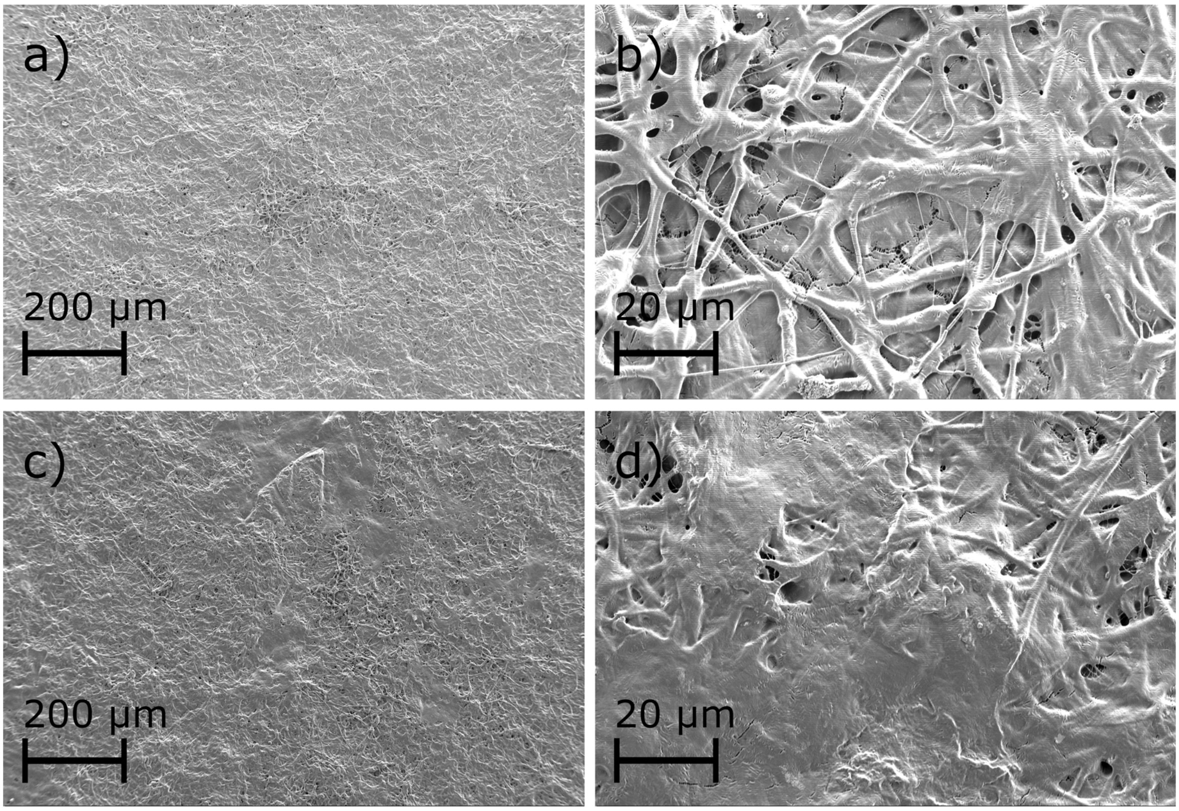

Figure 10 SEM pictures of electrode with laminated interlayer (Magnification: a,c) 100, b,d) 1000)

It can be seen from Figure 10 that despite the lamination the fibrous structure of the interlayer is still obtained, at least for some of the upper layers. Figure 10 a) and b) have been prepared using a punching iron, while Figure 10 c) and d) have been prepared using the actual EL-CELL punch. It can be seen that the punching device has a small effect to the electrode surface since the pictures shown in c) and d) show some areas with smoother surface compared to a) and b). This might have been suspected, since the EL-CELL punch has a closed surface and is able to put pressure on the electrode surface, thus flattening the surface.

The fibers themselves are molten to a certain point and form a web-like structure on the surface with some pores still remaining. From this it can be seen that the lamination parameters may have been too mild, since it is not the smooth surface desired for the experiments. Optimizing the lamination parameters and their impact on the performance of the cells may become the center of attention for further studies (see chapter 6).

Figure 11 shows SEM pictures of all electrodes modified with an electrospun electrolyte. To observe the fiber morphology right after the spinning process, samples have been prepared using a punching iron. Despite the changes in the spinning parameters (see Table 10), no serious differences in the fiber morphology can be spotted. Interestingly, the fiber morphology shows a strong variety; especially flat ribbon-like fibers and round fibers dominate the morphology. It can also be noticed that some of the ribbons show signs of longitudinal stress fine web-like structures can be found. In addition, fine web-like structures can be found. These may originate from flat ribbons which have been teared apart during the spinning process. Therefore, it is assumed, that originally the morphology of the fibers has been ribbon-like, all other morphologies are remnant of teared ribbons. Similar effects, like flat ribbon formation and fiber branching/splitting, have been found and described by Koombhongse et al. [120].

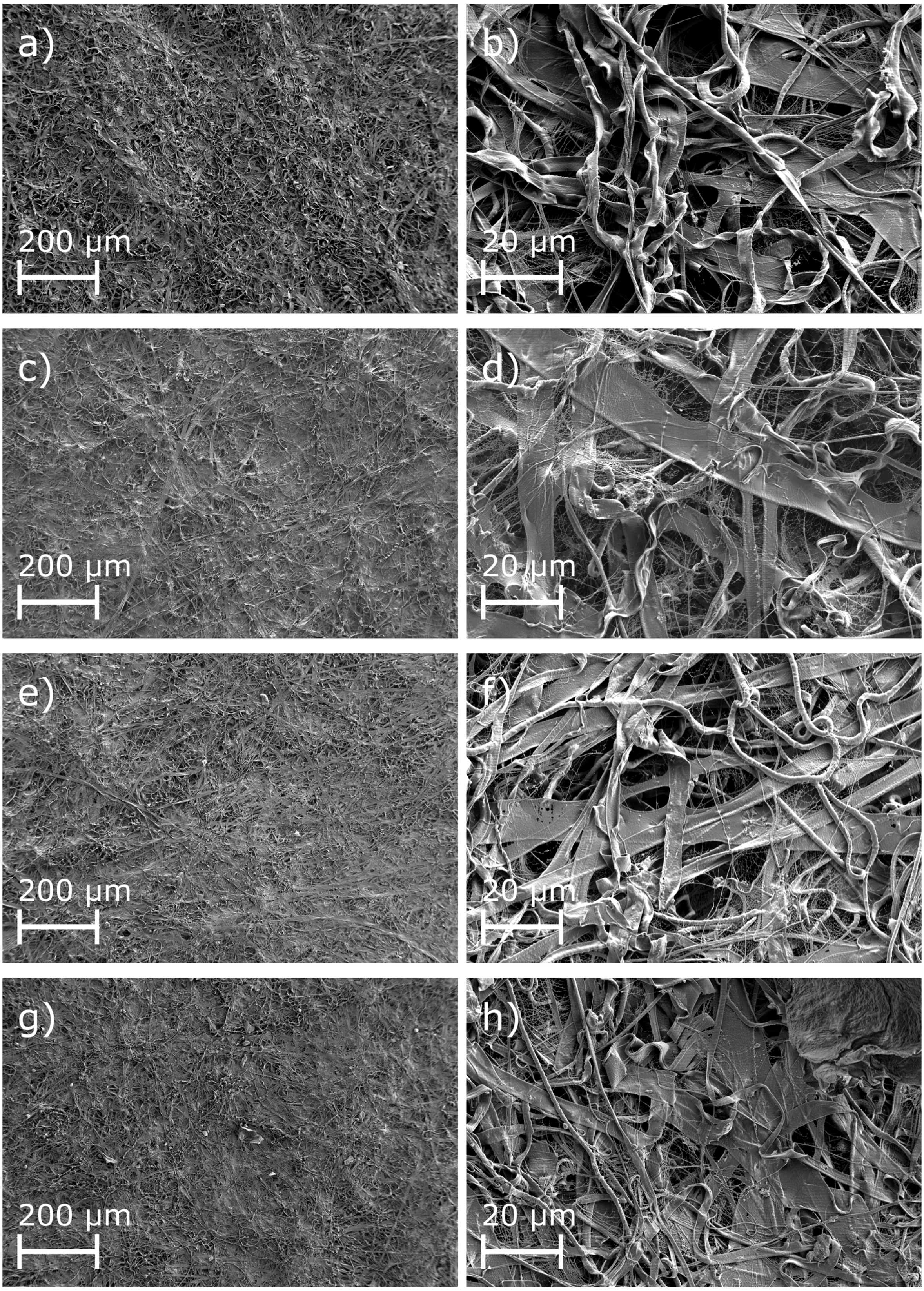

Figure 11 SEM pictures of electrode a, b) #17, c,d) #18, e,f) #21 and g,h) #24; Pictures a,c,e,g) are magnification 100, b,d,f,h) are magnification 1000; all samples have been prepared using a punching iron; Electrode numbers refer to Table 10

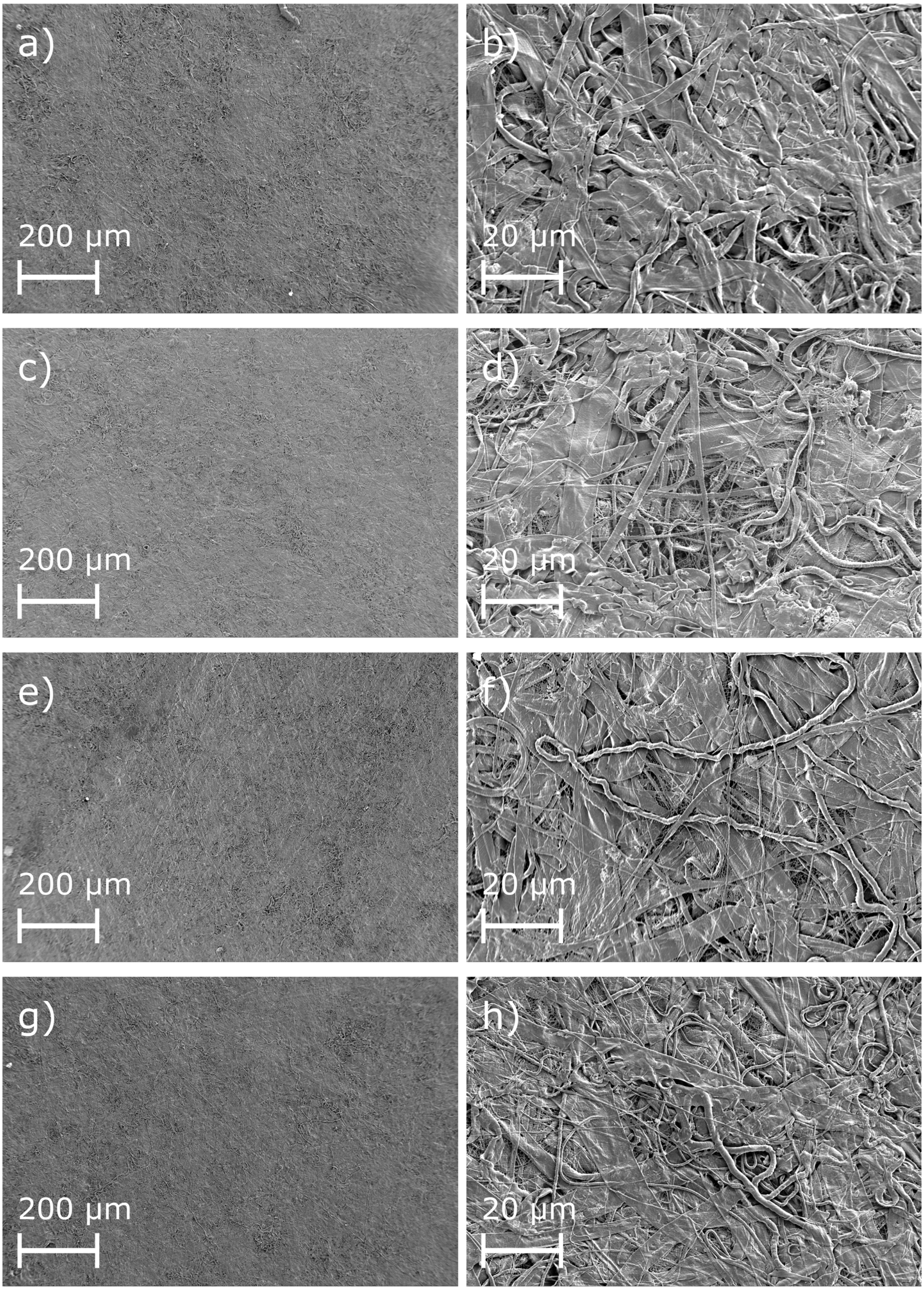

Figure 12 SEM pictures of electrode a, b) #17, c,d) #18, e,f) #21 and g,h) #24; Pictures a,c,e,g) are magnification 100, b,d,f,h) are magnification 1000; all samples have been prepared using an EL-CELL punching; Electrode numbers refer to Table 10

Figure 12 shows SEM pictures of all used electrodes after punching using an EL-CELL punch. It can clearly be seen that the closed EL-CELL punch has a large impact on the surface of the electrode due to its closed punching area. This leads to a compression of the fibers and therefore smoothens the surface.

Nevertheless, the fiber morphology in Figure 12 resembles the morphology found in Figure 11. It can still be seen that the fibers mainly form flat ribbons, with round fibers and fine web structure due to flat ribbon disassembly.

Interestingly, Figure 12 also shows areas upon the electrolyte surface with a significant change in density and pore areas. The reason for these areas is again found in the punching device. The electrospun electrolyte was not perfectly homogenous after the spinning process.

The electrolyte surface was further investigated in regard to the fiber diameter and the fiber diameter distribution. To analyze the fiber diameter and the fiber diameter distribution, SEM pictures with a magnification of 500 were used. For each picture 100 random site were chosen to measure transverse to the fiber axis. In addition, each fiber is only measured once. For flat ribbon fibers, sites where the observation was nearly perpendicular to the flat side of the ribbon were chosen. Each site was afterwards measured using the Fiji length measuring tool, calibrated using the scales provided by the SEM.

Figure 13 shows the fiber diameter histograms corresponding to the SEM pictures in Figure 11 and Figure 12. The fiber diameter ranges up to 13.5 µm for flat ribbon fibers. Due to the fact, that each fiber contributes only once to the histogram, the count for smaller fibers is higher, than for larger ones. The histograms shown in Figure 13 confirm the first impression gained from the SEM pictures: there is no significant change in the fiber diameter or the morphology in regard to changes in the electrospinning parameters, at least in the parameter regime chosen for this thesis.

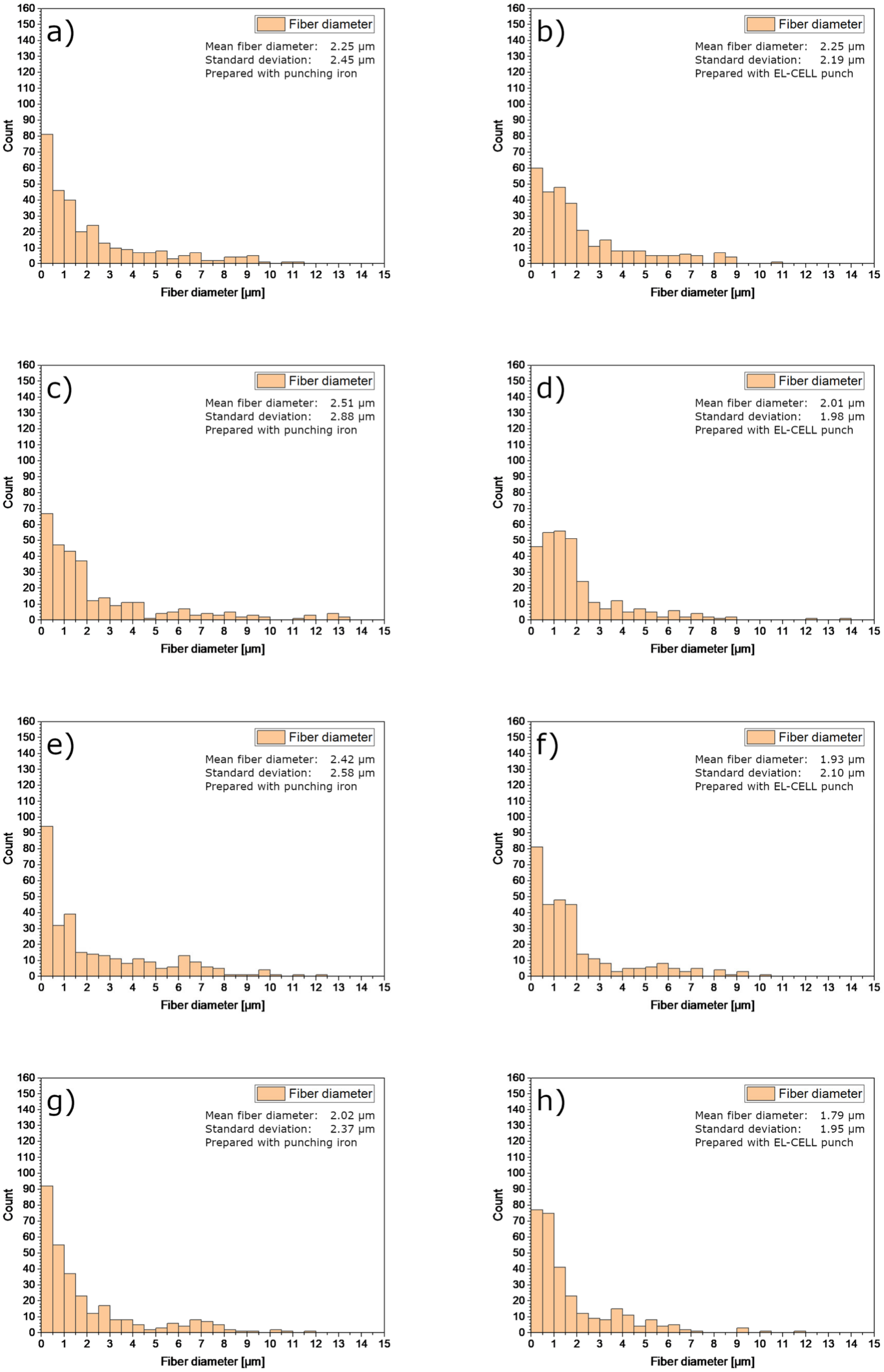

Figure 13 Fiber diameter histograms for all used electrospun electrolytes. a,b) #17, c,d) #18, e,f) #21, g,h) #24, Electrode numbers refer to Table 10

3.3.2 Impedance measurements

In the following chapter impedance data of full cells using electrospun electrolytes and lithium metal anodes will be presented. The used cell set-up is described in subchapter 2.3.4.1, the electrode and electrolyte preparation can be found in subchapters 2.3.3 and 2.3.4 respectively.

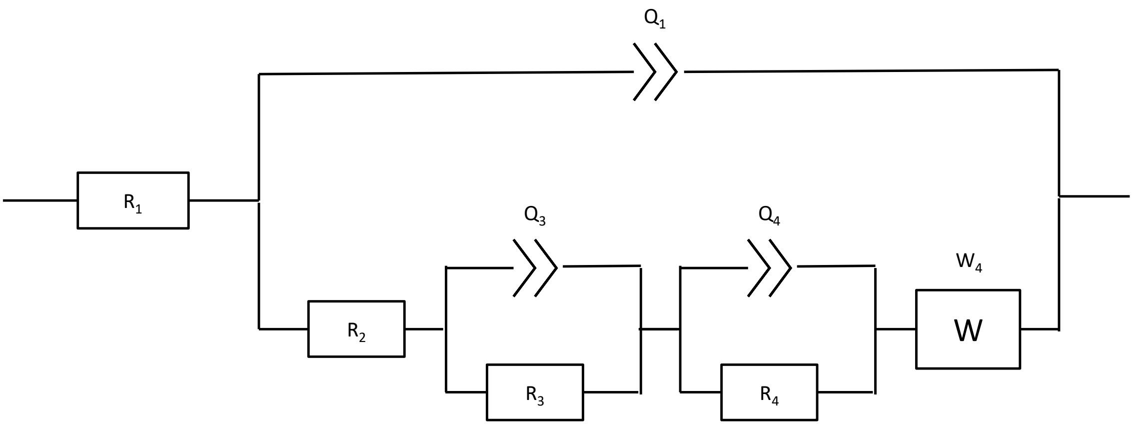

Figure 14 Equivalent circuit diagram used to analyze impedance data

Impedance measurements presented here have been conducted as described in subchapter 2.4.2. Each measurement was conducted after a completed cycling test, which are described in subchapter 2.4.3.

The data in this chapter will be focusing on two electrospun electrodes (#18 and #21) as well as reference cells using a solution casted electrolyte (#26). This step is taken, since said electrodes #18 and #21 have been the only cell series to complete the electrochemical testing program described above and therefore gained the most impedance data. The reference cell system, though it is also far behind said cell series, will be shown as a comparison between solution casting and electrospinning. Impedance data for all other cell series in this thesis is shown in the appendix (see Additional Impedance data).

To analyze the impedance measurements, a data fitting method is used (see subchapter 2.4.2).

The used equivalent circuit diagram is shown in Figure 14. A similar equivalent circuit has been used by Liu et al. to model full cells using a polymeric electrolyte [116]. The different contributions to the model are [116]:

1. R_1: Ohmic resistance of the used experimental set-up
2. Q_1: Geometric capacitance of the cell
3. R_2: Electrolyte bulk resistance
4. $Q_{3,4}$, $R_{3,4}$: Electrode/Electrolyte interfacial capacitance/resistance
5. W_4: Warburg impedance

In this thesis, especially the ionic conductivity and the interfacial resistances as well as their changes with cycling will be of interest. The ionic conductivity is calculated using Eq. 6. The ionic conductivity is thereby defined by the thickness of the electrolyte d, the electrolyte bulk resistance R_2 and the electrode area A. The bulk electrolyte resistance is calculated using the first semi-circle of the impedance spectrum, since this is related to the electrolyte resistance. The area is the geometric area of the smaller electrode, in this case the lithium metal anode. The thickness of the electrolyte was measured before building the cells.

$$\sigma = \frac{d}{R_2 \cdot A} \tag{Eq. 6}$$

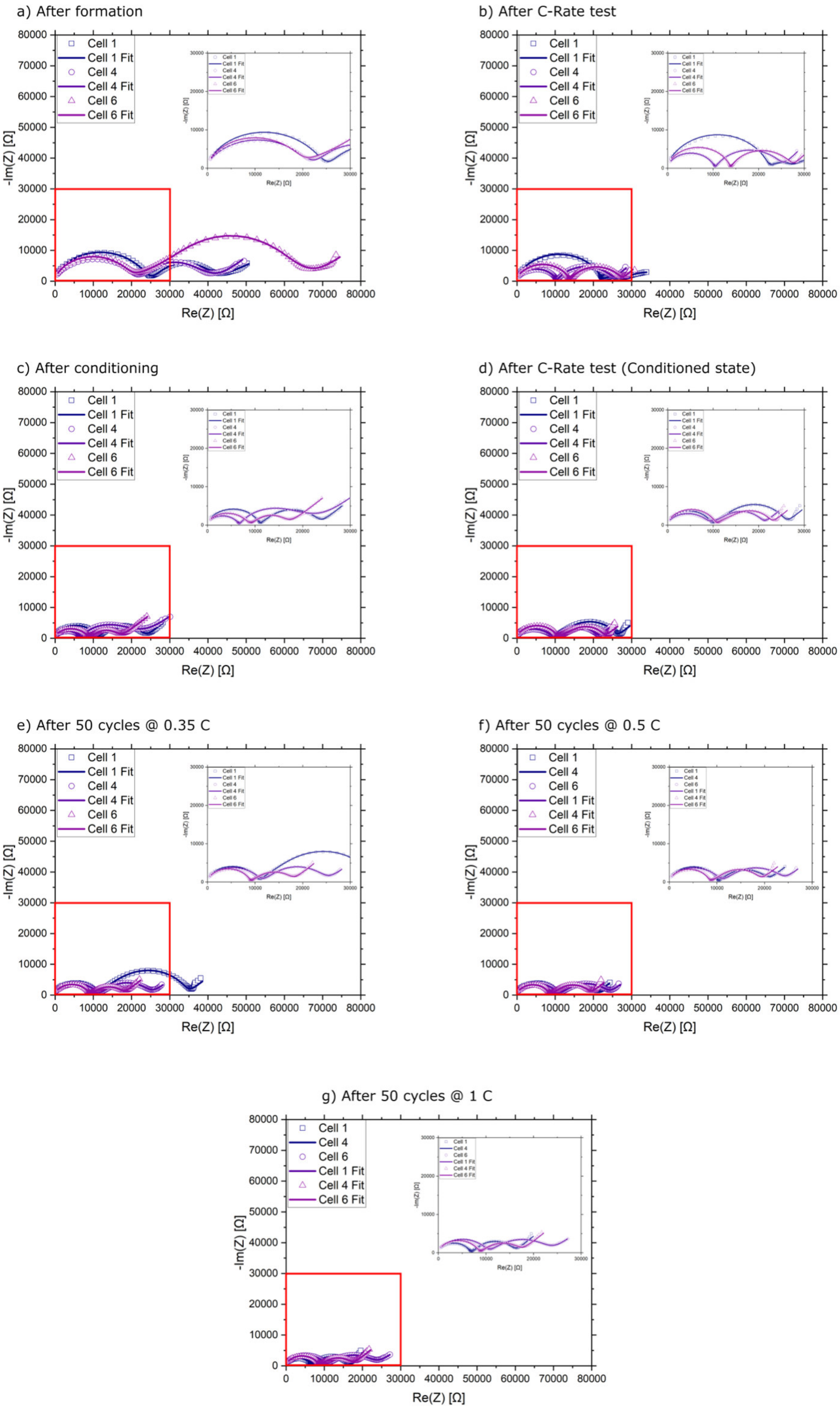
a) After formation

b) After C-Rate test

c) After conditioning

d) After C-Rate test (Conditioned state)

e) After 50 cycles @ 0.35 C

f) After 50 cycles @ 0.5 C

g) After 50 cycles @ 1 C

Figure 15 Impedance spectra for cells using electrospun electrodes #18. Framed areas are shown as insets

Figure 15 shows the fitted impedance spectra for electrode #18. It can be seen that the chosen fitting model suits all shown data in a satisfactory way. The impedance spectra show great differences for each cell as well as between each measurement step.

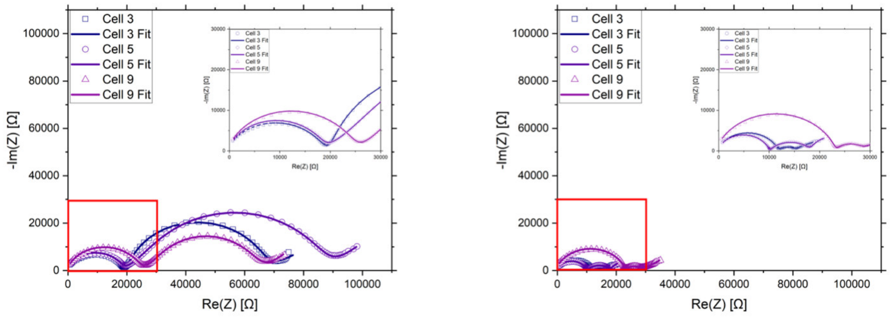

a) After formation

b) After C-Rate test

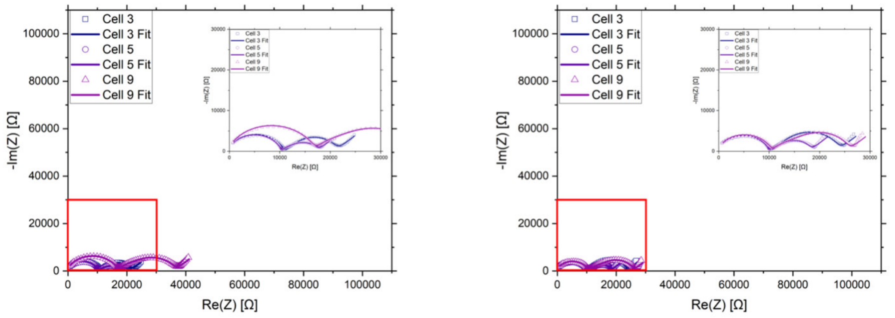

c) After conditioning

d) After C-Rate test (Conditioned state)

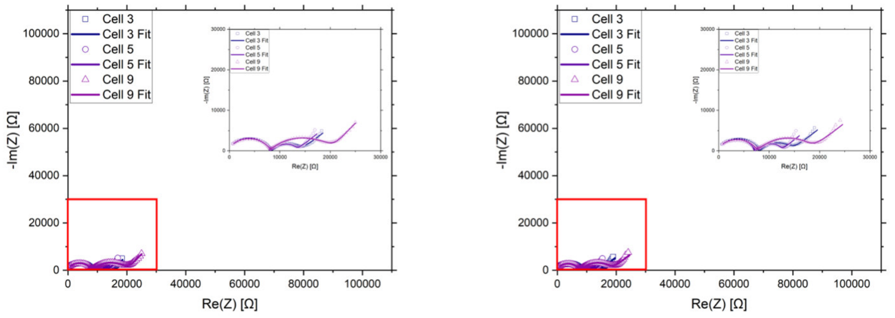

e) After 50 cycles @ 0.35 C

f) After 50 cycles @ 0.5 C

g) After 50 cycles @ 1 C

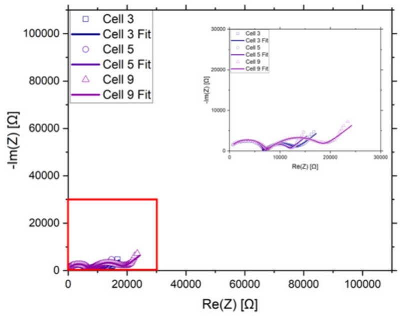

Figure 16 Impedance spectra for cells using electrospun electrodes #21. Framed areas are shown as insets

The first semi-circles (high frequency regime), which are quite similar to each other after the formation seem to develop differently during C-Rate tests. This trend seems to be not fully reversible by conditioning the cells. Interestingly, after C-Rate testing the cells in a conditioned state, the semi-circles, except for the capacitance, are quite similar again. This finding is quite interesting for future aspects of cell production and battery management of such cells. After cycling the cells, the semi-circles start to differentiate slowly.

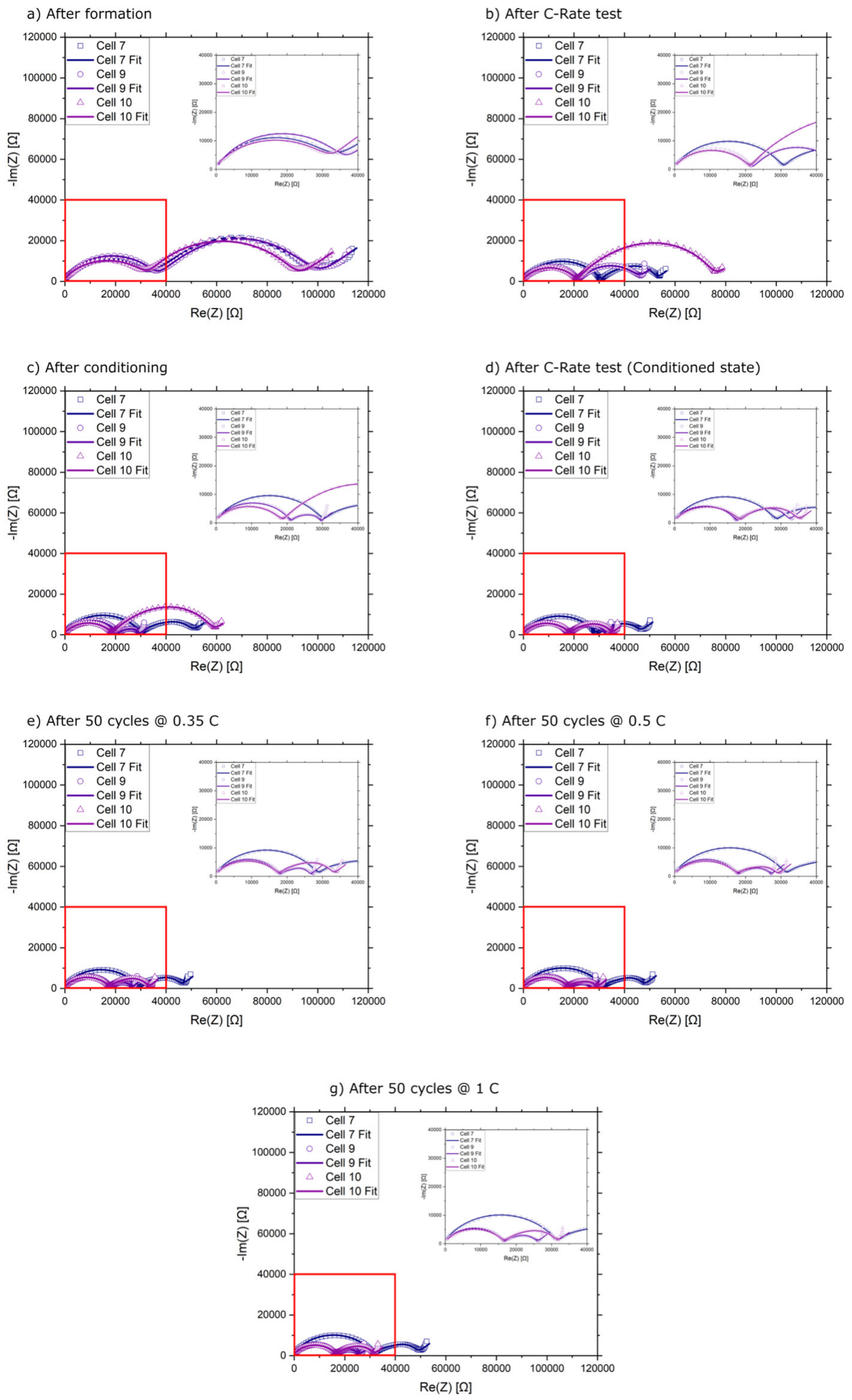

Figure 17 Impedance spectra for cells using electrodes #26 (solution-casted electrolytes); e-g) have been conducted after conditioning. Framed areas are shown as insets

Unfortunately, the second semi-circles (medium frequency regime) show no definite trend over the course of the electrochemical tests.

Figure 16 shows the fitted impedance data for electrode #21. The effects found with electrode #18 seem to apply again.

Figure 17 displays the fitted impedance spectra for cells using electrode #26 and solution-casted electrolytes. Similar effects as in Figure 15 and Figure 16 can be found for the first semi-circle of the spectra; the semi-circles seem to shrink due to the electrochemical cycling. Interestingly, the effect appears not as pronounced as for cells using electrodes #18 and #21.

Ionic conductivity

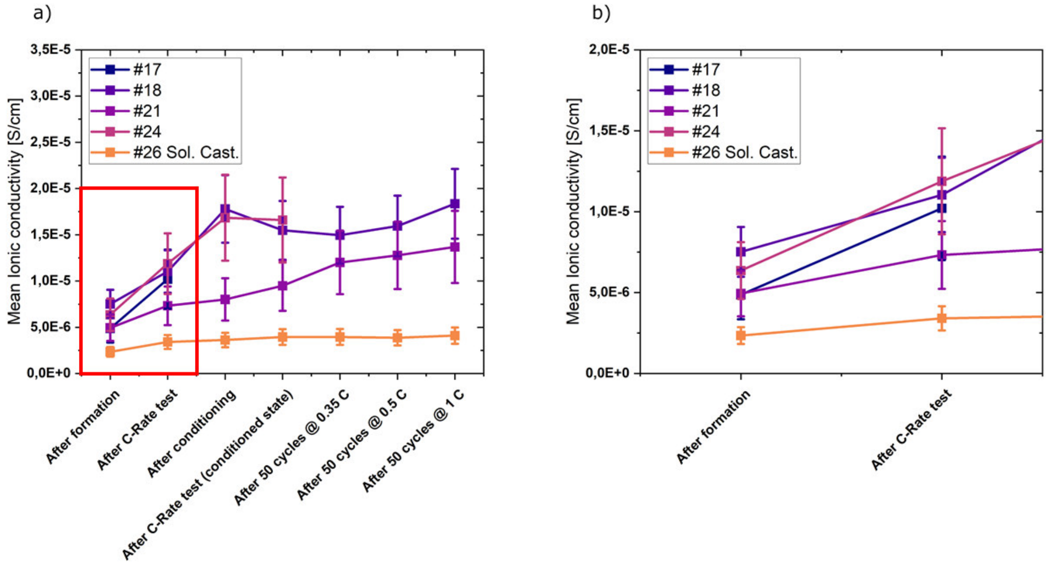

Figure 18 Mean ionic conductivities for all measured cell series

From the impedance data of all measured cells, the ionic conductivity of the electrolytes has been calculated. The results can be found in Figure 18. The trends described previously can be seen more clearly. The ionic conductivity of the cells using electrode #18 as a cathode is found to increase by nearly a factor of 10 until the measurement after the conditioning step. For all the following measurements, the ionic conductivity seems to level of around a value of $\sigma = 1.5 \times 10^{-5}$ S/cm (see also Table 1). Those values are similar to previous values obtained by Freitag et al [18]. For electrode #21 an increase is also seen also up to the measurement after the C-Rate test in the conditioned state, but on a lower level; the increase is much smaller than for electrode #18. Electrodes #17 and #24 show also show an increase in ionic conductivity values. Both have a similar increase until after the C-Rate test.

The lowest ionic conductivities are shown by the solution casted samples.

Figure 18 confirms the trend seen in Figure 15 and Figure 16. The results in ionic conductivity are comparable to values known from literature. A summary of ionic conductivities for electrospun and solution casted PEO-based electrolytes can be found in Table 1. It can be seen that the ionic conductivities are in fact in accordance with values found by previous publications using electrospun electrolytes of comparable compositions. Interestingly, the ionic conductivity of the investigated electrolytes changes with a higher number of cycles. This phenomenon seems to be coupled to the current applied during cycling. For the first three cycling tests, a strong increase in ionic conductivity can be observed for all electrospun electrolytes. After the conditioning, when all cells are set to a capacity of 90 µAh and resulting currents are applied (18 – 450 µA), the ionic conductivity seems to change less. There are some possible explanations for this phenomenon:

1. Expansion of the electrodes and slight compression of the fibers: According to Banitaba et al and Freitag et al, smaller fibers and more contacting points between the fibers lead to an increased ionic conductivity [17, 18].
2. Rupture of bigger fibers into smaller ones: From the SEM pictures in Figure 12 it can be seen that some bigger fibers already have been damaged during the electrospinning process. In case of mechanical stress due to cycling, these fibers could disintegrate into smaller fibers which are favorable for increasing the ionic conductivity [17, 18].
3. Change in the crystallinity: During cycling the crystallinity of the PEO fibers improves by the movement of the ions within or along the fibers. Again, lower currents can improve the crystallinity more than higher currents since the cut-off voltage is not reached as fast.

A compression of the fibers during cycling would lead to the different effects.

During cycling with low currents, the electrode can expand and compress the electrolyte slightly, resulting in an increased contact area between the electrospun fibers and therefore leading to an increased ionic conductivity. For cycling with higher currents, the cathode is not able to expand, since the cut-off voltage is reached to fast due to a high internal resistance and therefore no more compression can occur; the ionic conductivity remains nearly the same with the error bars; This would mean that the ionic conductivity changes are only slightly to none for high current cycling tests. It can be seen from Figure 18 that the mean ionic conductivity rises for all electrospun cell series until after the cell conditioning measurements. The previous cycling experiments (formation, C-Rate-test, and conditioning) use very small charging/discharging currents (see 3.2.3 for reference). Due to the small capacities defined in the formation process, the currents during the first C-Rate test stays small as well; the range varies from 1 µA to 90 µA.

Another factor for the increase in ionic conductivity is caused by the cycle numbers. For both the formation and the first C-Rate test the cycle numbers each cell must absolve is fixed. This is not true for the conditioning. Since the cells gained capacity in a strongly individual manner, it is decided to fixate the capacity to 90 µAh for all cells by conditioning. To achieve this a conditioning step as described in 3.2.3 is used. This leads to a quite different number of cycles for individual cells and therefore more compression cycles for cells with longer conditioning. From the model proposed above (see 1 Expansion of the electrodes) this leads to the conclusion that the increase in ionic conductivity is also linked to the number of absolve cycles within a certain current range. Especially cell series #18 and #21 show interesting differences in these regards. Cells of series #18 took 77 cycles to reach 90 µAh on average, while those of series #21 only took 29 cycles.

A third hint towards the proposed explanations includes data from solution-casted reference cells. Since solution-casted electrolytes are not structured in a similar way compared to electrospun electrolytes, no pores or fibers can create an increased contact surface and thus increase the ionic conductivity. A stagnant ionic conductivity for solution-casted cells (as seen in Figure 18) indicates towards the proposed interpretation.

Another possible explanation for the behavior of the ionic conductivity is mentioned in 2, the rupture of bigger fibers into smaller ones. From SEM pictures shown in 3.3.1 during electrospinning bigger fibers can be damaged by the electrostatic forces; the damage can even lead to a complete decomposition into much smaller fibers. In case the pre-damaged fibers would disintegrate during cycling (e.g., by mechanical stress due to cathode expansion), the contact surface would increase due to the thinner fibers. This would lead to an increase in ionic conductivity. The effects due to smaller currents and due to cycle numbers would be the same as described for a compression of fibers into the pores; actually, both explanations can play a role in interpreting the shown data. More elaborate investigations need to be conducted to directly proof these theories; due to time limitations these measurements are not part of this thesis but will be mentioned below.

Regarding the expansion of the electrodes, in-situ dilatation experiments can pose as a suitable method to investigate. This would require enabling this battery system in a flexible cell housing, e.g. Pouch. Efforts to transfer this battery system into a pouch cell housing on a proof-of-concept level have been conducted. Due to time limitations, a thorough study on pouch cells was not possible. Both solution-casted and electrospun cells must be measured.

To gain insight regarding the decomposition of larger into smaller fibers, different experiments may be proposed. One possible method could use x-ray or neutron radiography or tomography.

Another explanation may be a change in crystallinity due to the cycling. This explanation for the increase of the ionic conductivity is possible, but, based on the data in this study, highly unlikely. Since a lower number of crystalline phases in the PEO improves the ionic conductivity, it could explain an increase over cycling.

A direct proof for this theory is not found in this thesis. A hint towards this theory would be an increase in the ionic conductivity of the solution-casted electrolyte cells. Electrospun cells should be not as effected, since the crystalline phase of electrospun PEO electrolytes is suppressed according to Banitaba et al. [17] . An experiment to test this hypothesis could be realize by an ex-situ XRD study or even an in-situ wide angle x-ray scattering experiment.

Interfacial resistances and capacitances

Besides the ionic conductivity, impedance measurements can also be used to gain knowledge on the interfaces of batteries by analyzing the semi-circle in the medium- to low-frequency regime. This data would be especially interesting since the different preparation methods (e.g., EL-CELL punch for electrospun, cutting for solution-casted electrolytes) and different surface morphologies (fibrous-discrete vs. continuous) might show strong differences. However, the measurement and the analysis of this data is strongly dependent on the state-of-charge (SOC) of the battery. A different SOC can lead to great problems and misinterpretation in analyzing the data; this problem does not occur for the data gained in the high-frequency regime of the PEIS data.

Regarding this thesis, this problem occurs in two different facets:

1. Defining the SOC: Since the capacity changes during the course of the electrochemical tests and the number of cycles (see chapter 3.3.3) the SOC may also change for each cell strongly.
2. Adjusting the SOC: Since all used cells show a quite high internal resistance, adjusting the SOC proofs to be quite challenging. Before the impedance measurements the cells are intended to be charged to a certain voltage, to assure a similar SOC and open circuit voltage, but due to the strong differences in the internal resistance, the charging step usually has no significant effect. Reducing the current would not solve the problem completely, since the resistances compared between the cell series vary much to strongly, so a defined SOC for all cells is not easy to obtain.

Because of these reasons, this thesis foregoes a detailed investigation regarding the interfaces to avoid a severe misinterpretation and a false conclusion. The data gained on this study can be found in the appendix.

Further knowledge on the used coin cells has to be gained and, based on that, refined methods to obtain secure SOCs (e.g. by modified cycling methods) have to be developed.

3.3.3 Analysis of full-cell data

In the following chapter electrochemical cycling data of full cells using electrospun electrolytes and lithium metal anodes will be presented. The measurements presented here are conducted according to the description in subchapter 2.4.3. The error bars are defined by the standard deviation of the cell series.

A special focus is put on the data from cell series #18, #21 and #26, since all these cells have completed the cycling tests. All electrode sheets have been manufactured from the same batch. The area loadings can be found in Table 16 in the Appendix.

3.3.3.1 Capacities and Coulombic efficiencies

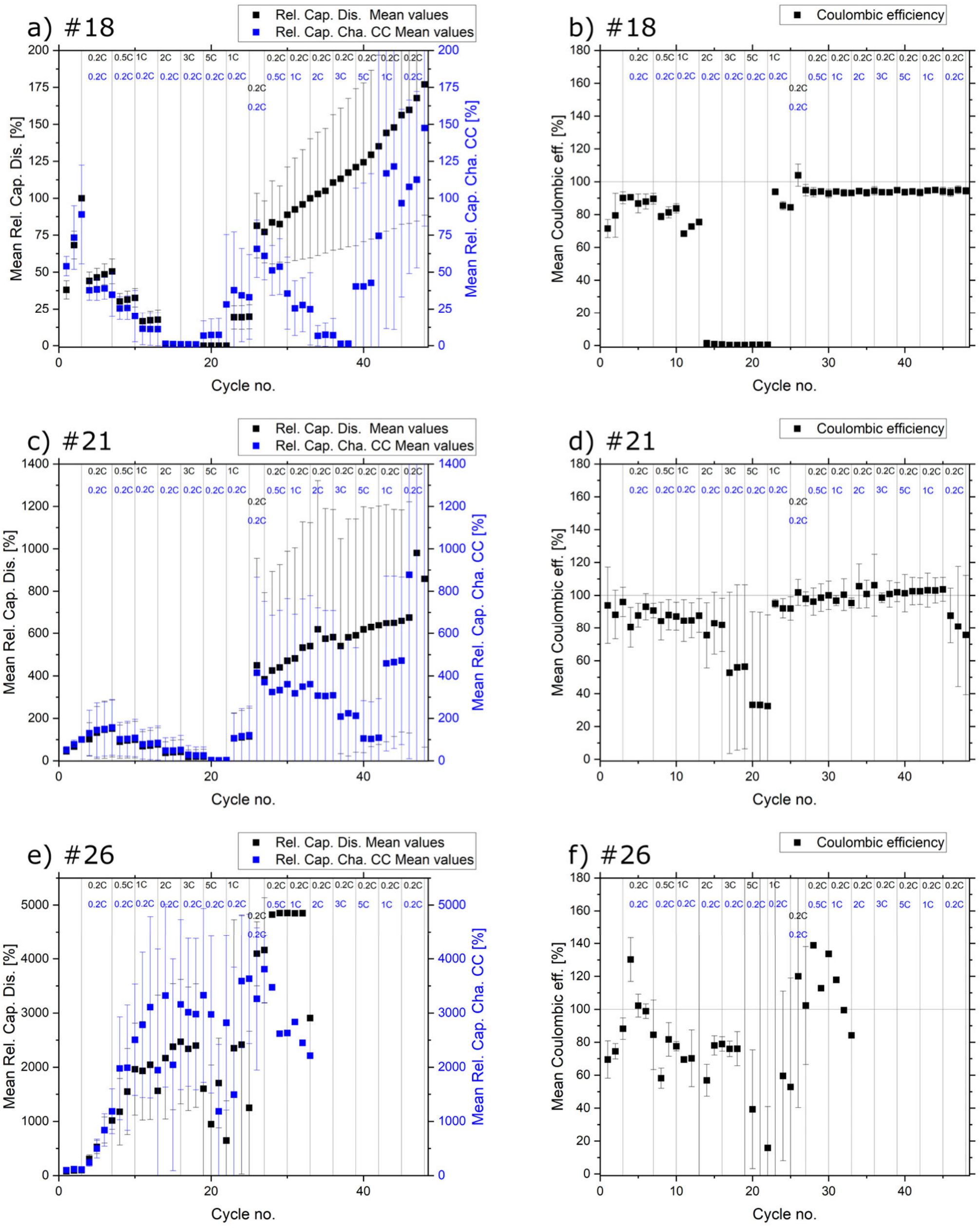

Figure 19 Formation and C-Rate test: CC charge and discharge capacities and coulombic efficiencies for cell series a) ,b) #18, c), d) #21 and e), f) #26. The capacities are relative to the discharge capacity measured for the third formation cycle of each cell

During Formation and C-Rate test

Figure 19 a), c) and e) show the mean CC charge and discharge capacities data gained from the formation and the C-Rate test. It can be seen that during formation, which uses a fixed small current of 1 µA, the capacity increases for all cell series. This phenomenon can also be found in liquid electrolyte cells and is usually associated with the wetting on the electrolyte-anode interface [121]. It is usually coupled to a coulombic efficiency smaller than unity [122]. This is in accordance with the coulombic efficiency found for the formation cycles in Figure 19 b), f) and, within the error range, Figure 19 d).

During the CC-discharge C-Rate test, the capacities for cell series #18 show a strong decrease while the coulombic efficiency values decrease too. From 2C-charge capacities and coulombic efficiency drop to 0. This can be explained by the very high internal resistance of the cells, as can be seen by the quite pronounced discrepancy between CC-charge and discharge capacities. This leads to an increased voltage drop for higher current values. The capacity loaded to the cell cannot be discharged and therefore both charge and discharge capacities decrease drastically. This can also be found for cell series #21. In difference to cell series #18, cell series #21 still works for a discharge current of 3C. This may be an artifact created by the C-Rate test procedure. Since the C-Rate was normed to the discharge capacity from the third formation cycle, strong differences on the currents inflicted on the individual cells arise. The mean discharge capacity for cell series #21 is 9.192 µAh while for cell series #18 it is 13.084 µAh. It is therefore clear, that the charging and discharging currents differ significantly during the C-Rate test. Cell series #26 displays an exceptional behavior. The data gained from the discharge rate test seems to not follow any pattern at all. Again, the explanation can be found in the discharge capacity of the third formation cycle. The mean discharge capacity for cell series #26 is only at 3.240 µAh. This leads to exceptionally small currents. For some C-Rates the currents are smaller than the lower current limit provided by the measuring system. This leads to errors in the measurement, rendering the C-Rate test for cell series #26 not conclusive enough. The above-mentioned findings lead to the decision to condition the cells after the C-Rate test to provide a similar level of all cells before further testing.

During the CC-charge rate test the measured capacities differ for charge and discharge significantly. The reason here is that the slow discharge allows a “deep” discharge and, even when the CC-charge rate is too high to charge the cell it is compensated by the CV-charging phase. Another possible explanation could be lithium stripping. Interestingly, the discharge capacity increases quite strongly for cell series #18 and #21 during the charge rate test. At the end of the test the mean discharge capacity has increased to nearly 175% for cell series #18 and nearly 900% for cell series #21. It also seems from the data that this phenomenon occurs more pronounced for smaller cycling currents. This leads to the conclusion, that the cathode used in all cell series has not reached its full potential after formation and gradually releases its potential capacity, leading to an extremely theoretical formation process. One possible explanation for this phenomenon may be found in the PEO expansion mentioned in subchapter 3.3.2. Since PEO poses as an ionically conductive matrix in the cathode it is possible that this PEO expands during cycling and reduces the pore volume within the electrode.

This leads to short ion migration pathways within the cathode and enables more lithium ions to migrate to or from the electrolyte, leading to an increased capacity.

The C-Rate test for cell series #26 was aborted after the discharge rate test for three reasons: First it was clear from the discharge rate test that no significant data could be gained from continuing the test; second, due to the extremely small currents, the cells would have been conditioned well above the aimed capacity of 90 µAh and comparison of data between the cell series would have become nearly impossible. Third, the completion of the C-Rate test would have taken a very long time and could have induced calendric aging phenomena not present in the other cell series.

During Conditioning

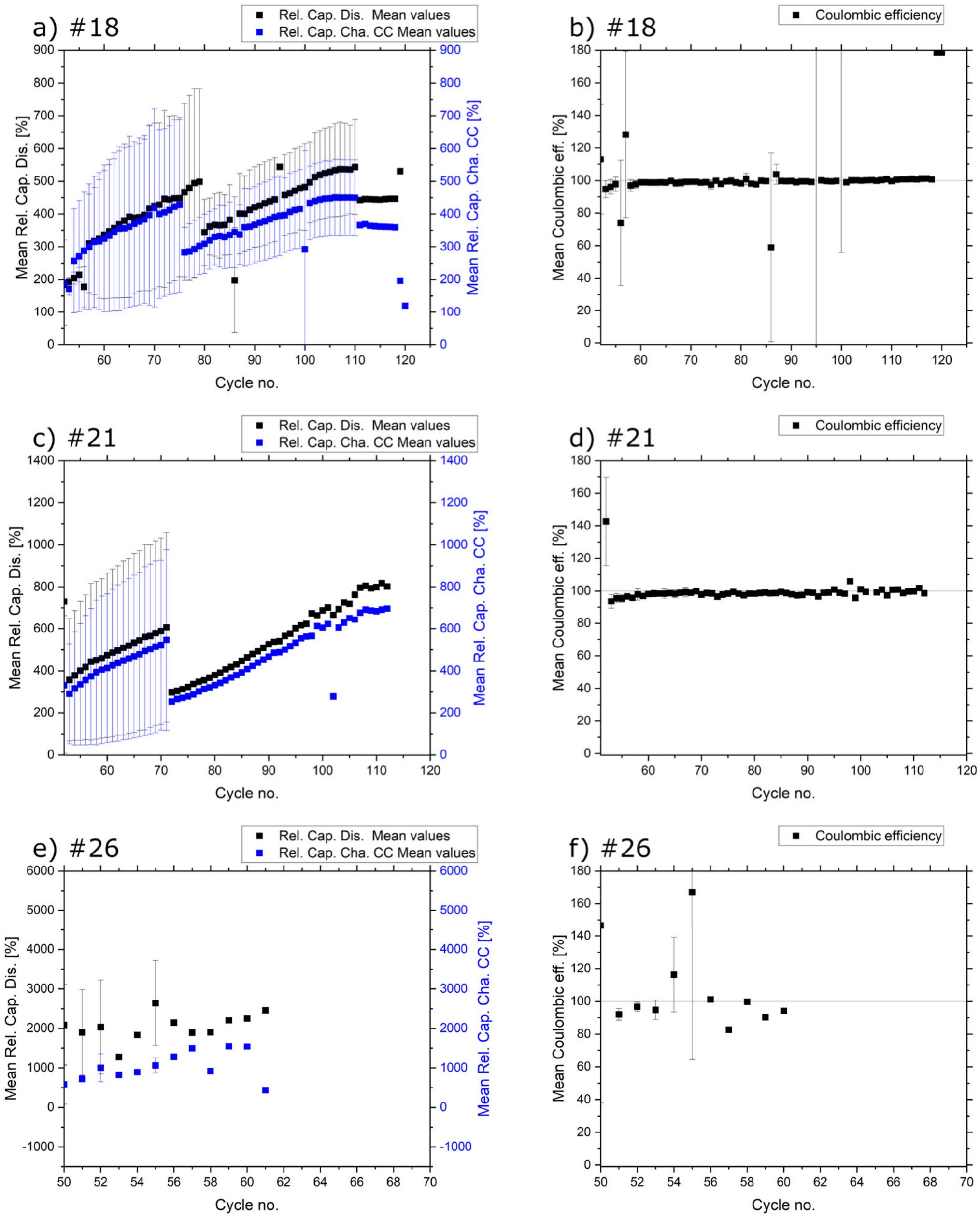

Figure 20 Conditioning of cells: CC charge and discharge capacities and coulombic efficiencies for cell series a) ,b) #18, c), d) #21 and e), f) #26. The capacities are relative to the discharge capacity measured for the third formation cycle of each cell

Figure 20 shows the conditioning of the cell series #18, #21 and #26. As previously mentioned, this step was necessary to provide a more comparable starting point for all cell series. As described in subchapter 3.2.3, the conditioning step was stop when the discharge capacity reached 90 µAh using a small current of 5µA. Such a small current was chosen, since it was unclear whether higher currents, applied for a higher amount of cycles, could actually lead to a decrease in capacity. Depending on the starting condition of each cell, conditioning took a different amount of cycles to be completed. Cell series #26 poses a specialty among the cell series. It can be seen that the conditioning phase for this particular cell series is quite short. This is mainly because the slow discharge C-Rate test in the unconditioned state, which induced conditioning beforehand. It can be seen from Figure 20 e) that conditioning was already in an advanced state. Only few cycles were necessary to reach 90 µAh. The coulombic seems to be quite unsteady during the conditioning cycles. This could already implicate aging processes during the C-Rate test, which may be even reversible. Further investigation on this particular topic has to be undertaken.

Figure 20 a) and c) show the capacity development for cell series #18 and #21, respectively. Both cells series show a significant increase in both CC-charge and discharge capacity with increasing cycle numbers. Interestingly, both cell series show sudden drops in capacities. These drops are indicating a finished cell. For cell series #18, the first conditioned cell occurred after 79 cycles, the second after 110 cycles. For cell series #21, the first cell finished conditioning after the first cycle, the second after the 71st cycle. This shows the strong differences between the individual cells even within one particular cell series.

It is of special interest, why the capacity increases during cycling for these cells. To see, if an electrochemical reaction, similar to the build-up of an SEI, is involved, the coulombic efficiency as well as dQ/dV-plots have been calculated from the data. The dQ/dV-plots will be analyzed thoroughly later in the thesis. The coulombic efficiencies can be found in Figure 20 b), d) and f). For cell series #18 and #21 the coulombic efficiencies are close to unity for nearly all cycles during conditioning. This indicates no additional electrochemical reactions other than the lithium intercalation processes. For the first cycles during conditioning the coulombic efficiency increases slightly first, which could be an equilibrating reaction induced by the C-Rate test before.

The absence of additional electrochemical reactions during conditioning, which has to be analyzed further using dQ/dV-plots, indicates a mechanism for increasing the capacity which is purely relying on physical processes and could pose as an additional indication towards the hypothesis mentioned earlier.

C-Rate test after conditioning

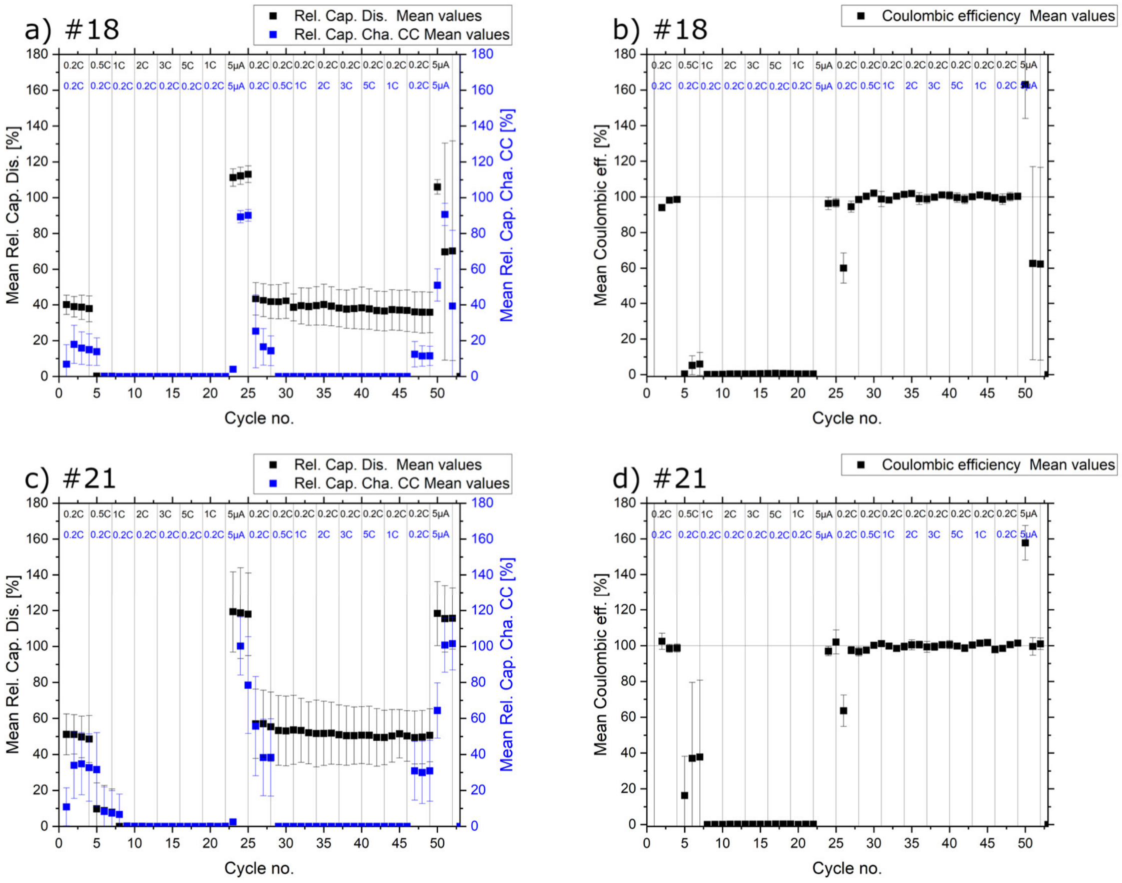

Figure 21 C-Rate test after conditioning: CC charge and discharge capacities and coulombic efficiencies for cell series a) ,b) #18, c), d) #21. The capacities are relative to the conditioned discharge capacity of 90 µAh

Figure 21 shows the C-Rate test conducted after fully conditioning the cells of cell series #18 and #21. Both cell series show relatively similar trends. The discharge rate test shows similar results found in the first C-Rate test before conditioning. Due to the much higher currents, the C-Rate has been normalized to 90 µAh discharge capacity, only 0.2 and 0.5C show charge and discharge capacities of more than 5% relative to 90 µAh. The high internal resistances of the cells lead to a pronounced voltage drop, exceeding the lower cut-off-limit at 2.0 V at an instant for C-Rates higher than 0.5C.

To gain insight whether the cells loss or gain capacity during “cycling” with such high currents or maybe get damaged, three control cycles using 5µA charge/discharge currents have been included to the C-Rate test procedure. From the first 5µA section it can be seen that the cells do not lose capacity. Actually, the cells seem to gain capacity during the discharge rate test. For both cell series the discharge capacity measured during this first 5 µA section manifest around a value of 120% relative to the conditioned 90 µAh.

The coulombic efficiencies start near unity for low C-Rates but continue to drop quickly for higher C-Rates. During the 5 µA section the coulombic efficiencies arise to values near unity again.

The CC-charge rate test again resembles the data shown in Figure 19. The main difference that occurs is that after conditioning no increase in the discharge capacity can be seen. Interestingly, cell series #21 shows higher levels of discharge capacities compare to cell series #18. Unfortunately, the data is not yet sufficient to be able to give a satisfactory explanation for this phenomenon. More research has to be undertaken on this topic, especially on the electrolyte/electrode interface. The coulombic efficiency during CC-charge rate test is for both cell series close to unity.

This changes for the second 5 µA section of the test. While cell series #21 remains on the same level in regards to capacities and coulombic efficiencies as during the first 5 µA section, cell series #18 decreases dramatically. This may be due to a soft short circuit, which seem to be reversible. Even due to this soft short, all cells could continue testing.

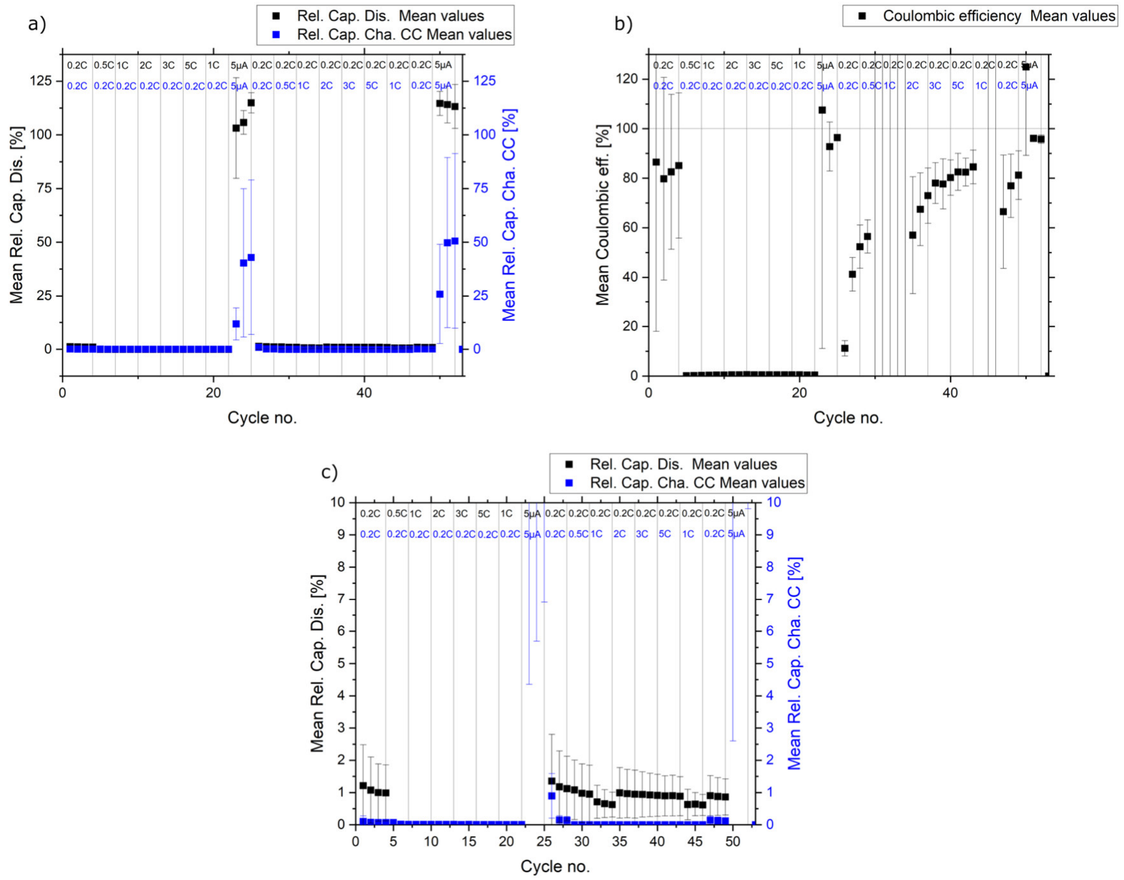

Figure 22 C-Rate-Test after conditioning for cell series using electrode #26 a) mean relative capacities for CC charging and discharging b) mean coulombic efficiency c) Zoom-in into the C-Rate-Test. The capacities are relative to the conditioned discharge capacity of 90 µAh

Figure 22 a) shows the C-Rate test after conditioning cells using a solution-casted electrolyte. For both discharge and CC-charge rate tests, only a very small fraction of the conditioned capacity can be used with these cells. In comparison to cell series #18 and #21, which both use an electrospun electrolyte, the performance difference becomes quite clear. For example, at a charge/discharge rate of 0.2C (equals 18 µA for a conditioned cell with 90 µAh) solution-casted electrolyte cells only reach discharge capacities around 1 µAh. Cells using an electrospun electrolyte easily reach capacity values of 36-54 µAh (see Figure 21). This seems to correlated to the ionic conductivity measured for the cells using different types of electrolytes (see Figure 18). While cell series #26 only reach ionic conductivity values of around 5 µS/cm, cell series #18 shows an enhanced ionic conductivity with nearly a magnitude higher value.

Despite the great difference in capacity values, cell series #26 shows a similar behavior in regard to the capacity development with increasing cycle numbers. For all investigated cell series, the capacities seem to decrease over cycling with relatively high C-Rates (see Figure 21 a), c) and Figure 22 c)). Figure 22 c) shows one oddity though: during CC-charge rate testing, the discharge capacity drops slightly at a charge rate of 1C. Since this section appears for a second time in the charge rate test, the phenomenon can be seen twice. Interestingly, for charge rates greater 1C the discharge capacity recovers.

During cycling with 5 µA the discharge capacities of cells using a solution-casted electrolyte recover to values similar than for cells using electrospun electrolytes. The CC-charge capacity remains at much smaller values for solution-casted compared to electrospun electrolytes. The gap between charge and discharge capacities for cell series #26 hints, that the internal resistance of these cells is much higher than the resistance for cells using electrospun electrolyte.

Figure 22 b) shows the corresponding coulombic efficiencies gained from the C-Rate test. The coulombic efficiencies show a high fluctuation, the mean values are not close to unity, unlike the efficiency values reported for cells using an electrospun electrolyte (see Figure 21 b) and d)). An exception is posed by the values reported during 5 µA cycling. These fluctuate around unity. Again, this can be correlated to the CV-charging or to Lithium stripping from the lithium metal anode during discharge. This leads to the question whether high currents induce additional electrochemical reactions within cells using a solution-casted electrolyte.

During Cycling tests

Figure 23 a) shows the capacity development for cell series #18. As expected from the results of the C-Rate test after conditioning the cells, the discharge capacity drops significantly for the first cycle. Figure 23 b) shows the capacity for 50 cycles at a charge/discharge current of 32 µA. During the first four cycles (cycle number 55-59), the discharge capacity increases. This may be due to an influence by the previous testing procedure. More investigation on this topic is required, a satisfactory explanation con not be found using only the data gathered during this thesis. After the fourth cycle, the capacity decreases rapidly till the 25th cycle (cycle number 80) of this test. After this cycle, the decrease in capacity seems to slow down. For some cycles the capacity stabilizes on a certain level or even increases in a minor way. The coulombic efficiency (see Figure 23 e)) is fluctuating between values of 80 to 90 %, indicating, that there might occur additional

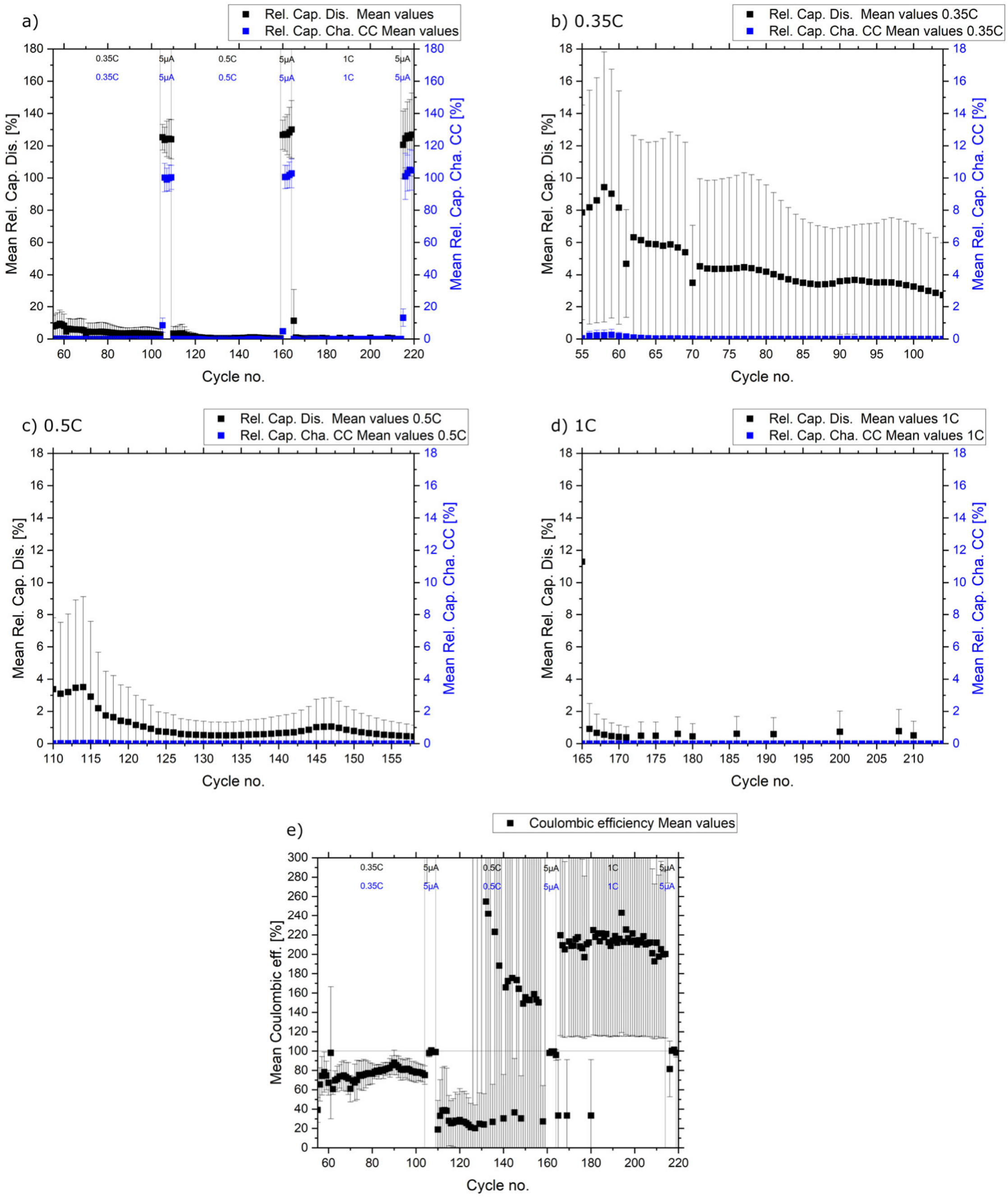

Figure 23 Cycling data for cell series using electrode #18 a) overview on all cycling data b) focus on 0.35C cycling c) focus on 0.5C cycling d) focus on 1C cycling e) coulombic efficiency during cycling

reactions during cycling. The following five cycles with currents of 5 µA show a slight increase in capacity compared to the 5 µA cycling section before cycling at 0.35C. For higher currents the capacity during the 5 µA cycling sections remains at this initial level, indicating that no significant reactions regarding the capacity have occurred.

Cycling at 0.5C gives a similar impression (see Figure 23 c)). During the first cycles the discharge capacity increases slightly with a rather rapid decrease for the following cycles. After cycle number 130 the capacity seems to level at very small values below 0.9 µAh.

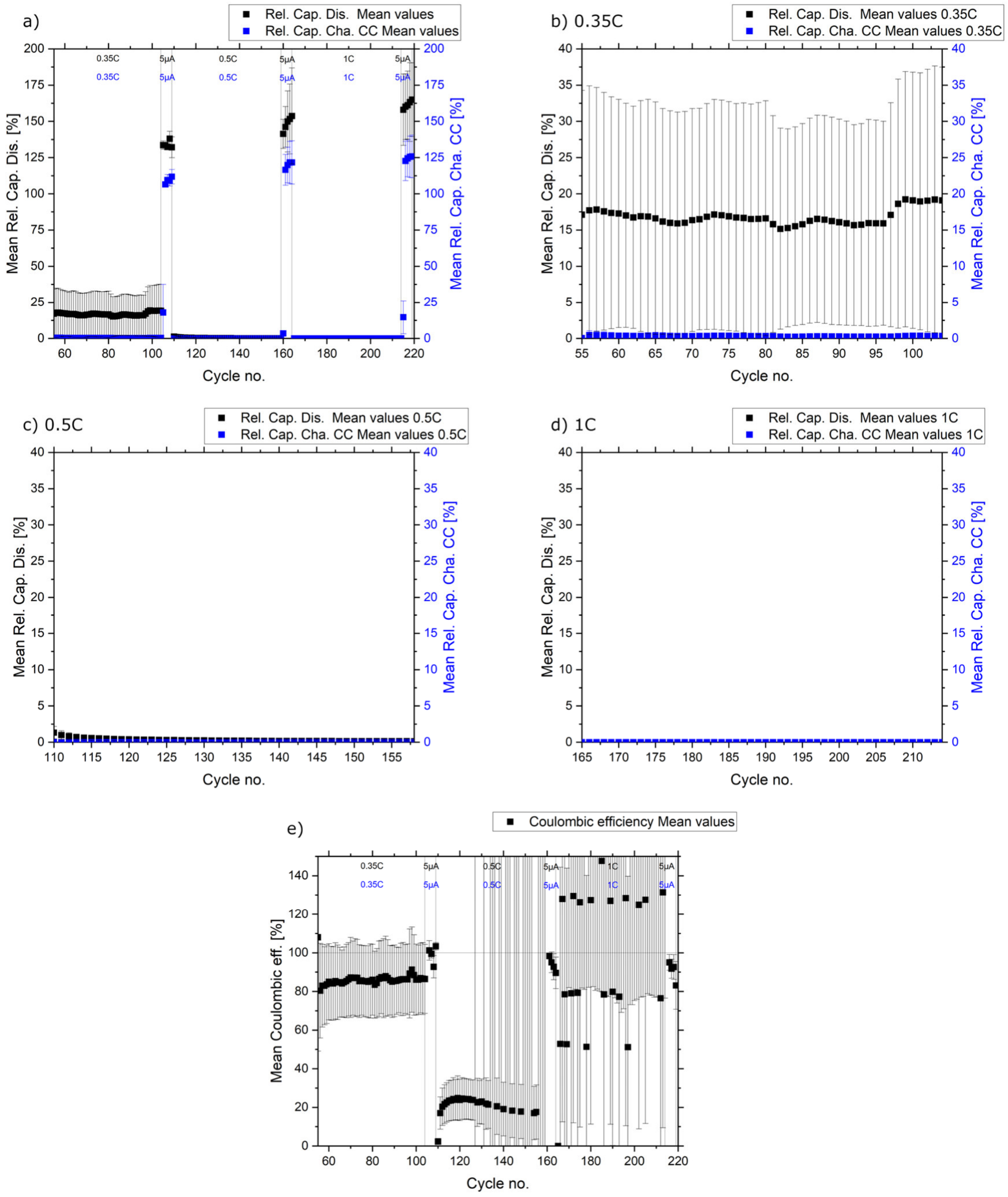

Figure 24 Cycling data for cell series using electrode #21 a) overview on all cycling data b) focus on 0.35C cycling c) focus on 0.5C cycling d) focus on 1C cycling e) coulombic efficiency during cycling

Coulombic efficiencies drop even further for higher C-Rates up to the point, where the charge capacity is not measured properly anymore. This leads to values far beyond unity. The same applies to the coulombic efficiencies calculated for 1C cycling of the cells. During cycling at 1C (Figure 23 d)), nearly no charge is either charged or discharged. Due to the voltage drop induced by the high currents the cut-off voltages are reached almost immediately. It may be of interest to correct the cut-off voltages by this voltage difference to further see the reaction of the cells to high currents in later experiments.

Figure 24 a) shows the cycling data for cell series #21. It depicts quite similar results than cell series #18. The measured capacities during cycling with 0.35C are depicted in Figure 24 b). Compared to the results from cell series #18 (see Figure 23 b)), cell series #21 shows some differences. While series #18 shows a steady decrease over 50 cycles, series #21 fluctuates around a mean relative capacity value of 18% (~16.2 µAh), with a small increase to 20% for the last few cycles.

The general capacity values are constantly higher for cell series #21 compared to #18. It is possible that this arises from a systematical advantage given by variations in the manufacturing process. A hint towards this theory is found in Figure 19 a) and c). The relative mean capacities reported in these two graphs show already a really strong difference in capacity development during the C-Rate test. A similar phenomenon can be found in Figure 20. Although it seems that the conditioning for cell series #21 and #18 proceed in a very similar way, this is only true for one particular cell of cell series #21. The other cells of this series complete the conditioning process much faster than the cells of series #18. This again leads to the conclusion, that the electrode used for cell series #21 had one particular advantage from the beginning to start. A detailed analysis which manufacturing step is crucial for this advantage has to be undertaken in future. Based on the hypothesis that the increase in capacity is due to a reduction in porosity within the electrode, electrode manufacturing steps, such as mixing and coating, or modification steps, such as laminating, may have to be taken into special focus. Especially the lamination modification step may be the key step, since it applies both pressure and heat to the polymeric electrode, therefore being able to change the electrode structure, similar to calendaring electrodes for liquid electrolyte cells [123].

Figure 24 c) and d) show the data gathered for cycling at higher C-Rates of 0.5 and 1C, respectively. For currents of 45 µA (0.5C), the capacity decreases in a rapid way. For 90 µA (1C) the capacity measurement is not reliable.

Figure 24 a) also shows the capacities measured during the 5 µA check-up steps. The capacities gathered here are again higher compared to the capacities measured for cell series #18. This again indicates that the cells of series #21 have an advantage over those of series #18 regarding the cathode.

Another effect may be seen from this. While cell series #18 remain the capacities for cycling at 5 µA after cycling at three different C-Rates, cell series #21 shows an increase not only during the 5 µA cycling, which is basically a continued conditioning for the cells, but also directly after cycling at higher C-Rates. The relative mean discharge capacities of series #18 stay between 120 and 128%, while the capacities of series #21 increase steadily.

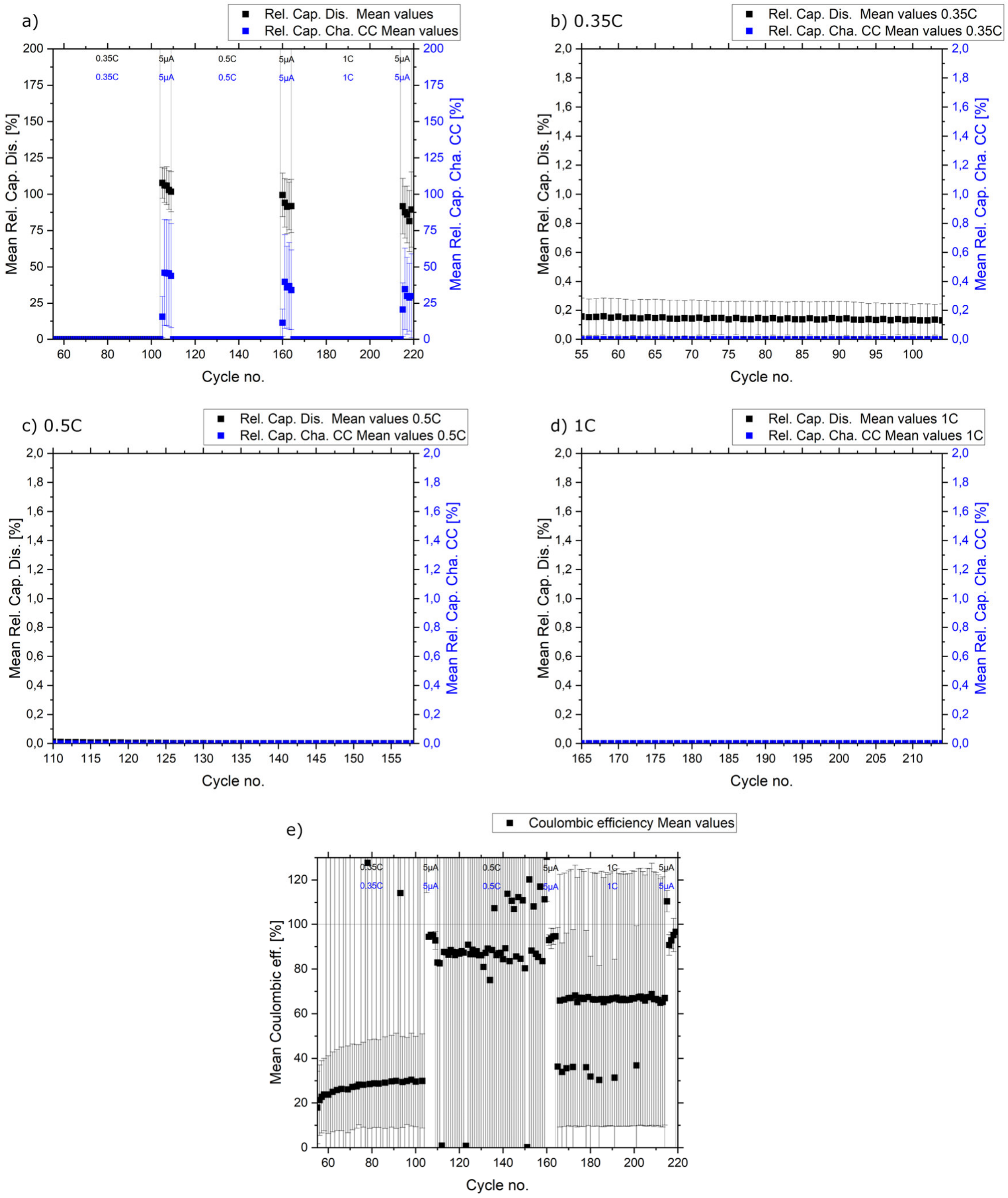

Figure 25 Cycling data for cell series using electrode #26 a) overview on all cycling data b) focus on 0.35C cycling c) focus on 0.5C cycling d) focus on 1C cycling e) coulombic efficiency during cycling

After cycling at 0.35C the mean values start at around 133%, after cycling at 0.5C it increased to around 141%. During this 5 µA cycling period it even increases to 153%. Cycling at 1C, where it would not be expected, has also a conditioning effect on the cells, showing a mean capacity of 158% for the first consecutive 5 µA cycle and 164% for the last, indicating once again an advantageous cathode compared to electrode #18.

The development of the coulombic efficiencies shows the exact same behavior as for cell series #18 (see Figure 23 and Figure 24).

The cycling data for cells using a solution-casted electrolyte is shown in Figure 25 a). It is easily seen that these cells have a much worse performance compared to both sets of cells using an electrospun electrolyte. The capacity development for cycling the cells at 0.35C is depicted in Figure 25 b). At first glance the capacity stays quite stable over the course of 50 cycles. But the capacity values are by far smaller compared to the values measured for all cell series with an electrospun electrolyte. While cells of series #21 reach values around 18 µAh, cell with a solution-casted electrolyte (cell series #26) merely reach values smaller than 0.18 µAh, a result as expected from the data gathered at this point. Cycling these cells at even higher currents does not lead to further results, since the cells immediately reach the set cut-off voltages.

The 5 µA cycling sections reveal an interesting difference between solution-casted and electrospun electrolytes. While the electrospun electrolytes are able to keep their conditioned capacity (see Figure 23, cell series #18) or are even able to further improve their capacity by cycling at high currents (see Figure 24, cell series #21), cells with a solution-casted electrolyte lose capacity. After 50 cycles at 1C the capacity measured during cycling with 5 µA drops even below the initially conditioned 90 µAh. This may have several reasons: First the used electrode may be the issue. As already described in subchapter 2.3.3, the electrodes have been prepared as sheets. It is therefore possible that the preparation steps, e.g. lamination, have had different effect. Second, due to time limitations as well as to prevent over-conditioning of cell series #26, the C-Rate test before conditioning the cells has been stopped before the 2C CC-charge rate test. It is possible, that during this charge rate test important processes take place within the cathode so that it shows worse performance than the cells of the other cells series, which have completed the C-Rate test before conditioning the cells. Nevertheless, a worse performance from cells using solution-casted electrolytes compared to electrospun electrolytes has been expected. This arises from the PEIS data gathered on the cells, which clearly show that the electrospun electrolytes have an advantage regarding the ionic conductivity at room temperature (see Figure 18).

The coulombic efficiencies are shown in Figure 25 e). These show also quite the differences when compared with efficiencies calculated for cell series #18 and #21. During 50 cycles at 0.35C the coulombic efficiency drops to values between 15 and 30 %, while for series #18 and #21 values between 60 to 90 % are reported. This may indicate that additional electrochemical reaction take place. For 0.5C and 1C the efficiencies may not be reliable, since the cut-off voltages are reached too fast. This may lead too much to high errors and misinterpretations.

3.3.3.2 Internal resistances

During C-Rate tests

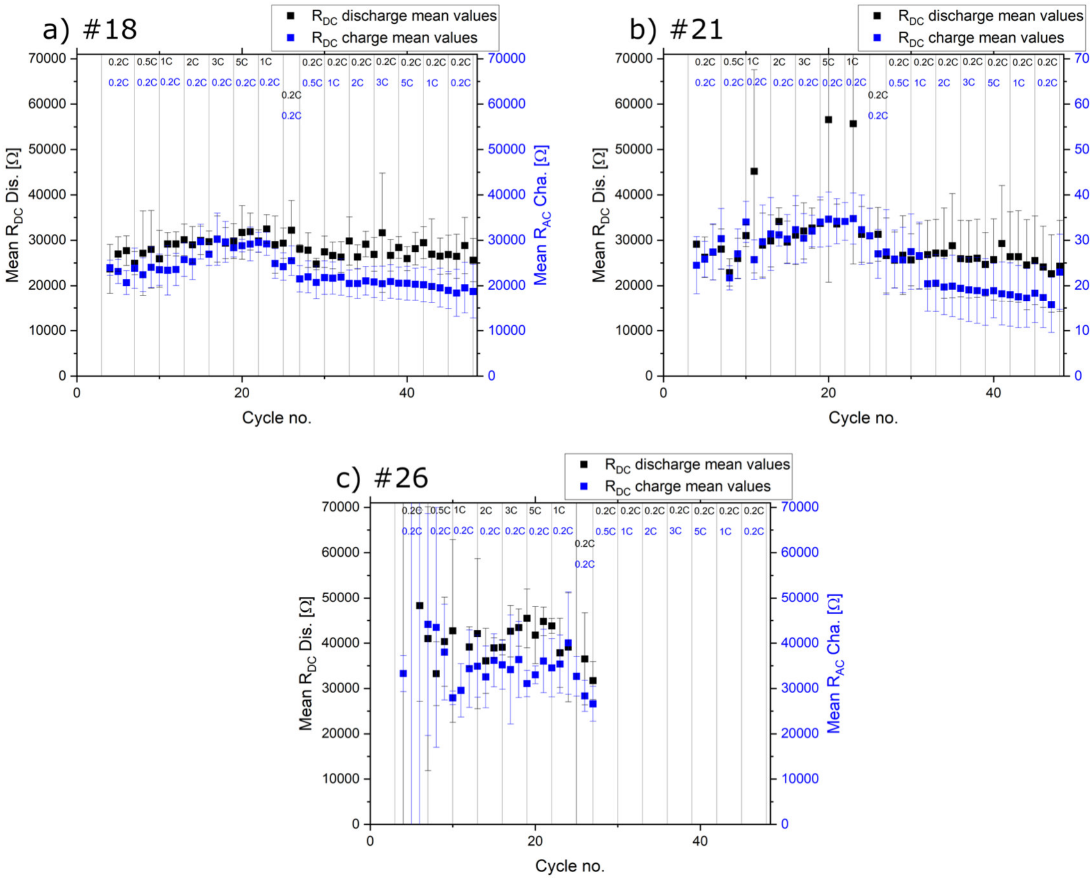

Figure 26 Internal resistances measured during C-Rate test for cell series a) #18, b) #21 and c) #26

Figure 26 shows the internal resistances of the cells for all finished cell series. The internal resistance is measured by the BasyTec measurement set-up automatically, starting from the first C-Rate test and labeled R_{DC}. Figure 26 a) shows the development of the resistance values during the first C-Rate test for cell series #18. The values measured during charging and discharging steps are plotted separately to see if any differences occur. As can be seen, during the discharging rate test the internal resistance for both charging and discharging show no significant difference within the error range. This changes during the charging rate test. While the discharging resistance values seemingly scatter around 28 kΩ, the charging resistance values drop to values below 20 kΩ, starting from a charging rate of 0.5C. Similar findings can be seen for cell series #21 in Figure 26 b). The deviation of charge and discharge internal resistance values seems to correlated with the deviation of the charge and discharge capacities measured for these cells (see Figure 19 a) and c)). Since the Coulombic efficiency during the charge rate test is close to unity for both cell series (see Figure 19 b) and d)), additionally occurring chemical reactions may not be an imperative part to explaining this phenomenon. Additionally, an expansion of the active materials within the cathode might be able to rise an explanation. Assuming the NMC_{111} expands during discharging (insertion of lithium ions into the active materials) and shrinks during charging (depletion of the active materials from lithium ions) of the battery, the porosity of the electrode changes. This not only enables lithium ions to move in a more direct manner but also allows electrons to move more along shortened paths, realizing a decreased internal resistance. This hypothesis is not proven by this data but hinted. A direct experimental proof has to be undertaken to fully understand this phenomenon and to enlighten the mechanisms responsible for the observed behavior of the cells.

Figure 26 c) shows the data generated for cell series #26 during the discharge rate test. No data was gathered during the charge rate test. The reasons for this have been mentioned before. For the discharge rate test, similar observations as found for the other cells series can be seen.

During Conditioning

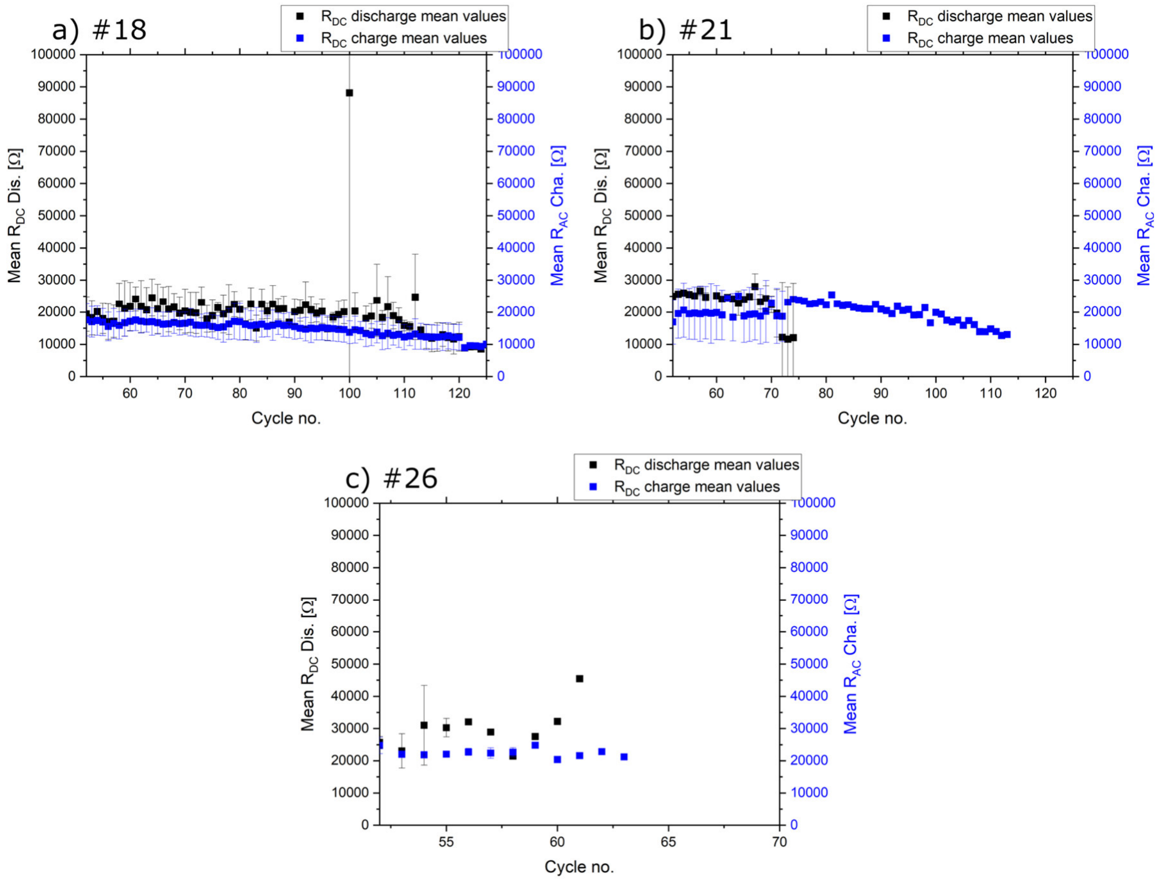

Figure 27 Internal resistances measured during cell conditioning for cell series a) #18, b) #21 and c) #26

Figure 27 a) shows the internal resistance values measured during the conditioning of cell series #18. At the beginning of the conditioning the resistance values are quite similar for both charge and discharge steps. A few cycles into the conditioning, the discharge resistance values scatter around a slightly higher resistance level compared to the charge values. For the last cycles, the values seemingly return to similar values, but this is only true for the longest lasting cell during conditioning. Interestingly, both charge and discharge resistance values steadily decrease along the advancing conditioning. Again, this correlates with the increase found in Figure 20 a).

Figure 27 b) shows the internal resistance development of cell series #21 during conditioning of the cells. For about 25 cycles a deviation between charge and discharge resistance values can be found. Afterwards, two cells have finished the conditioning process and only the last remaining cell is shown. For this cell, the resistance values are nearly the same, a behavior expected for charging and discharging with equal currents. Again, a decrease of the resistance values can be found over the course of the conditioning.

Figure 27 c) shows R_{DC} values for cell series #26. It can easily be seen that the conditioning for these cells only took few cycles, confirming the assumption, that these cells have been more affected by pre-conditioning during the first C-Rate test compared to the electrospun electrolyte cells.

During C-Rate tests after conditioning

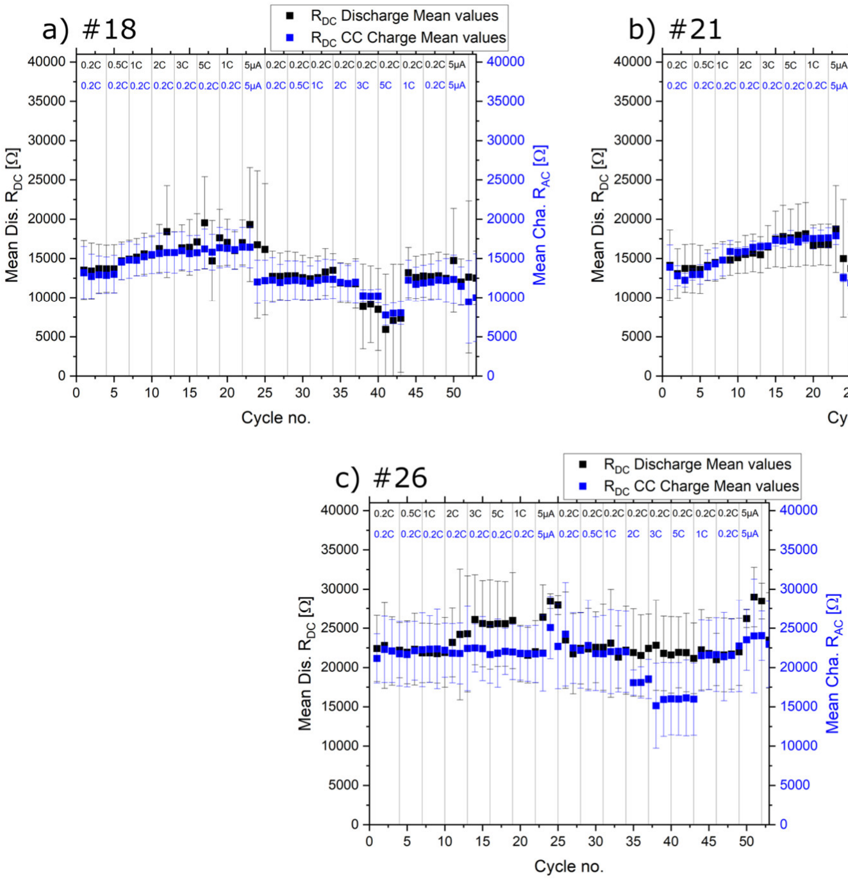

Figure 28 Internal resistances measured during C-Rate test after conditioning for cell series a) #18, b) #21 and c) #26

Figure 28 a) shows the internal resistance development of cell series #18 during the C-Rate test in a conditioned state. In contrast to the R_{DC} values measured for the previous C-Rate test, the internal resistance values show a smaller deviation between charging and discharging steps. During the discharging C-Rate test the resistance values increase slightly, starting from 0.5C discharging current. Interestingly, during the 5 µA cycling step between the discharging and the charging C-Rate test, the resistance values measured for discharging deviate for the second and third cycle. Similar effect can be found for the second 5 µA cycling step at the end of the charge C-Rate test.

Another observation to be seen from the C-Rate test is the development of the resistance during the charge Rate test. It can be seen, that during the charge rate test the resistance values drop compared to the values seen at the end of the discharge rate test. Additionally, the is no steady in- or decrease found during the charge rate test in contrast to the discharge rate test. For 3C and 5C charging rates both the charge and discharge resistance drop significantly. This is interesting, since a change in the charge resistance may be explained by a significant measuring error caused by the rapid rise in voltage due to the high currents of 180 µA and 450 µA, respectively. The values of the discharge resistance are not expected to change, since the current is not changed during the charge C-Rate test. It seems that the development of the resistance is dependent of the cycles previous cycles. Another possible explanation could be that during the short high voltage measured during high C-Rate charging the electrolyte gets polarized.

Figure 28 c) shows the resistance measured for cell series #26 during the second C-Rate test. It shows significant differences compared to the cell series using an electrospun electrolyte. The overall resistance values are significantly higher compared to Figure 28 a) and b) without a steady in- or decrease in the course of the C-Rate test. Interestingly, for higher C-Rates (2C and up), during discharging C-Rate testing the values of the discharge resistance increase, reversibly. The charge resistance stays the same. During charging C-Rate testing, the values of the charge resistance decrease for higher C-Rates, again reversibly. Also, the discharge resistance stays at a stable level. Contrary to the findings in Figure 28 a) and b) both resistances increase during 5 µA cycling.

During Cycling tests

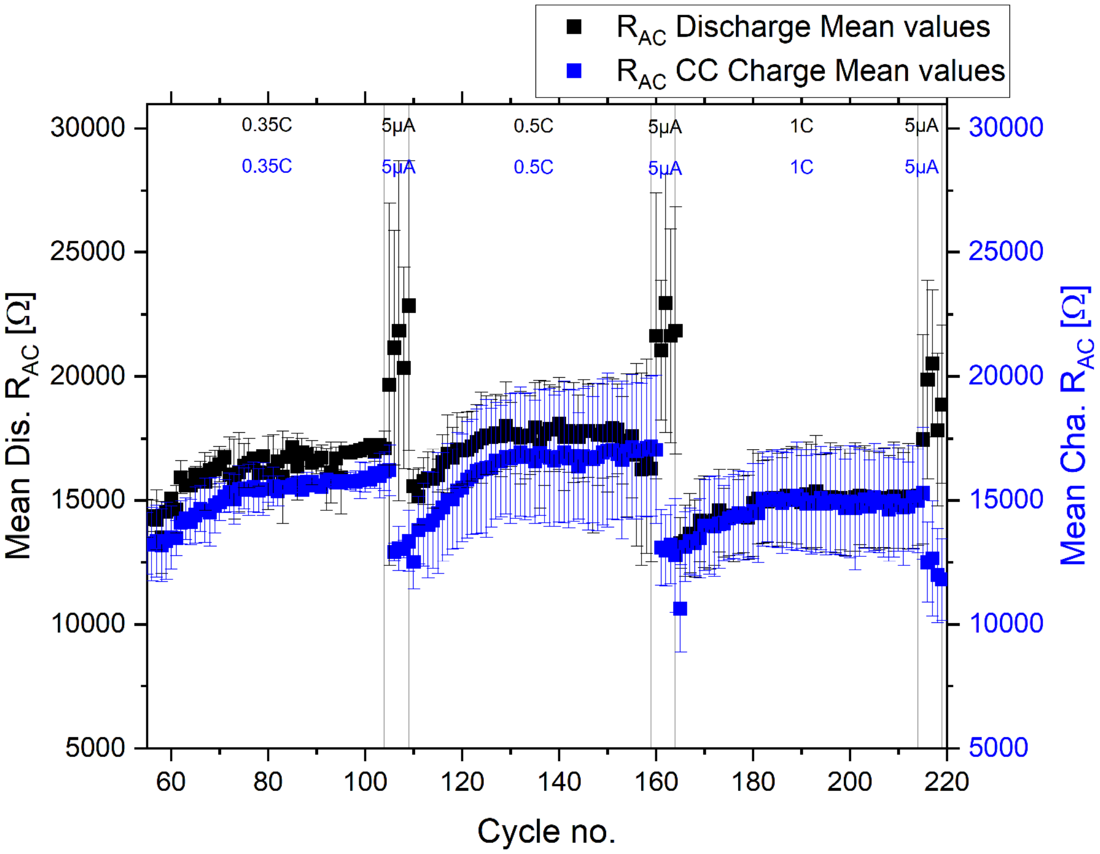

Figure 29 Internal resistance for cell series #18 during all cycling tests

Figure 29 shows the resistance development for cycling cell series #18 at three different C-Rates. From this plot it can be seen that the resistance increases slightly with the number of cycles. It seems for the resistance values to converge against a limit around 15 kΩ for all tested C-Rates. While C-Rates 0.35C and 0.5C show a slight difference in values between charging and discharging, 1C has no such gap. Interestingly, cycling at 1C shows the lowest resistance values among the three tested C-Rates. This data seems to be in accordance with the results seen in the C-Rate test before.

In addition, it again seems that the correlation found with Figure 20 and Figure 27 between the resistance and the capacitance seem to be applying here again. While the capacities during cycling decrease, the resistances increase in a similar manner.

In Figure 29 cycling at 5 µA between the higher C-Rates is also plotted. Different to the behavior during cycling at high currents, a pronounced gap between charging and discharging resistances can be found. While the charge values drop significantly compared to the last cycles at high currents, the discharge value increases rapidly. Gaps between the two resistances have been found also during the second C-Rate test and partially during conditioning, but neither have been the difference between charge and discharge this

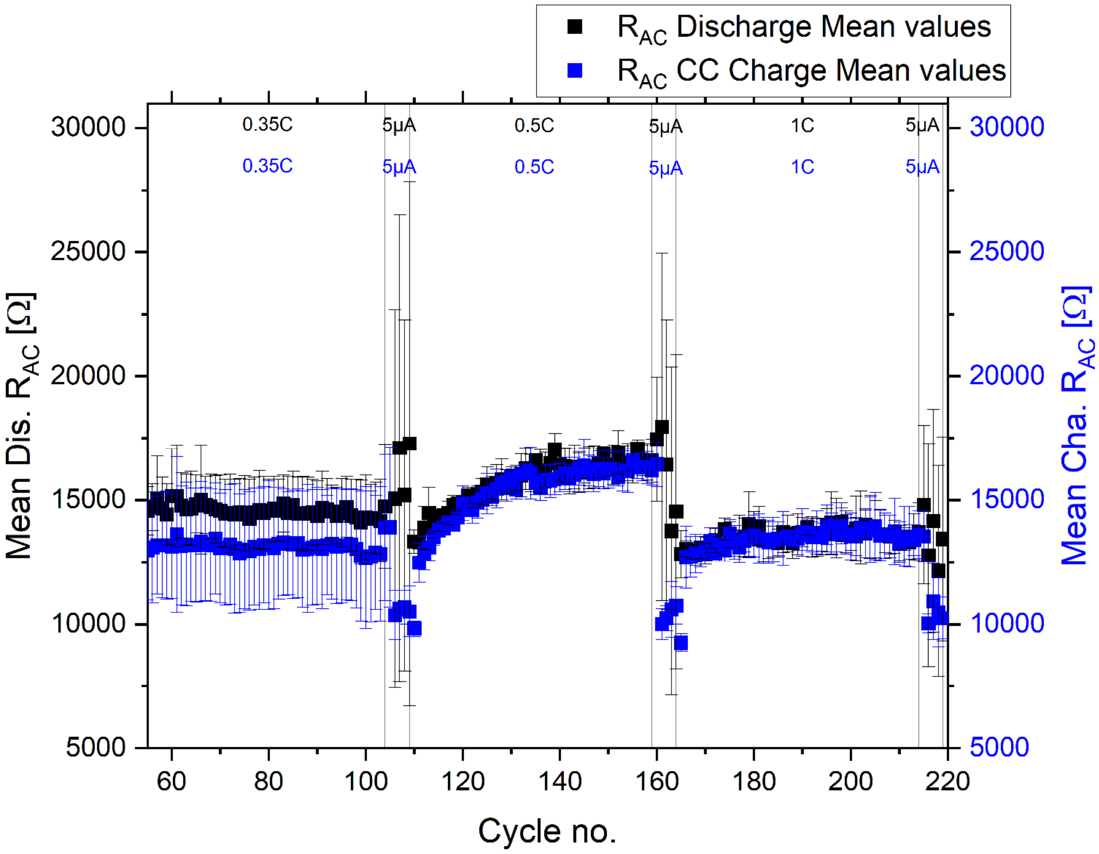

Figure 30 Internal resistance for cell series #21 during all cycling tests

pronounced. It may seem that the resistances are dependent on the cycling beforehand. Figure 30 shows the development of the internal resistance during cycling at different C-Rates. In comparison to Figure 29, a more pronounced difference between the charging and discharging resistance measured at 0.35C. While cell series #18 shows an increase in the resistance during 50 cycles at 0.35C, cell series #21 remains at a stable level. During the 5 µA cycles following the difference between charging and discharging resistances rapidly increases, as seen for cell series #18. Comparing Figure 24 and Figure 30 it can again be found, that the development of the capacity and the development of the corresponding internal resistance are reversed: while for 1C the resistance values increase with increased cycle numbers, seemingly converging to a limit lightly above 15 kΩ, the capacities are decreasing (see Figure 24 c)). In addition, a correlation between the difference between charging and discharging resistance and the difference between the CC charging and discharging capacities can be found from Figure 24 b)-d) and Figure 30. It seems, that the greater the difference between the capacities is, the greater the difference between R_{DC}-values. A possible explanation may be found in the chosen cut-off voltage limits. During cycling with different C-Rates, the cut-off voltage upper limit is often reached nearly instantly, therefore nearly no capacity is measured. For discharging the limit is chosen more suitably, hence a measurable discharge phase can be seen. The R_{DC}-values are calculated by using the voltage difference after a pause and at the start of a charge or discharge step. For most CC-charge phases, the voltage is overshoot to values between 4.5 to more than 6 V, leading to only a short pulse of current on the cell and to resistance values without ionic conduction or interface transition phenomena. For some discharge steps a capacity can be measured, the cut-off voltage is not reached immediately. Therefore, the resistance includes ionic conduction and interface transition phenomena and may be higher. For higher discharging currents, the same effects as mentioned for CC charging may apply and the resistances for charging and discharging approach each other. The increase in resistance values may be caused by polarization phenomena within the PEO. Since high currents are applied over many cycles and a certain asymmetry between charging and discharging is seen, a concentration gradient can arise within the cell, assuming that no lithium ions are stripped from the lithium anode during discharge. A possible explanation is the contact area between the electrolyte and the lithium metal. Since no thermal annealing step has been undertaken to improve the electrode-electrolyte interface it is possible that these interfaces vary strongly between the cells. These discreet contact points may limit lithium diffusion into the electrolyte at high currents and lead therefore to an accumulation of ions at the cathode during charging; this leads therefore to an overall polarization within the cell and an opposing electric field. Since the charging step is essentially not conducted, the accumulation of charges is not reversed and builds up with more cycles. This may be measured as an increase in the R_{DC} discharge value. For too high currents no ion conduction in either way is conducted and therefore no increase in resistance can be measured. As an experiment to test this hypothesis full cells with and without thermal annealing could be measured to see if any differences in the R_{DC} values can linked to discreet contact points on the electrode-electrolyte interfaces, including a carefully conducted impedance study to find out more on the electrochemical character of these interfaces. Additionally, modified test procedures regarding the cut-off voltages can be used to be able to fully study full cells without the limitation of ohmic overpotential. This applies also to cell series #18 and the corresponding C-Rate tests after conditioning of the cells.

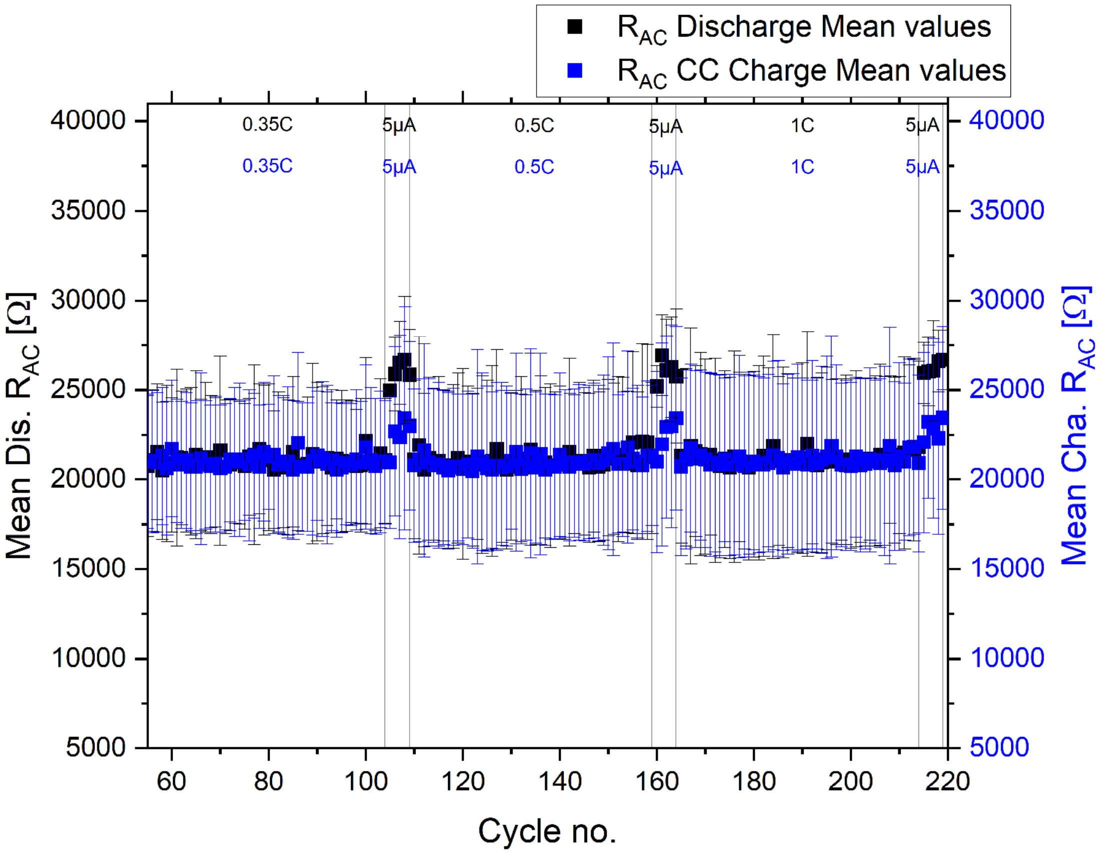

Figure 31 Internal resistance for cell series #26 during all cycling tests

Figure 31 shows the behavior of the internal resistance during cycling at 0.35, 0.5 and 1C. It can be seen easily that the internal resistance, unlike cell series #18 and #21, stays constant for cycling at all C-Rates. Additionally, differences between charging and discharging have vanished completely. As mentioned above, the reason is the ohmic overpotential for these high currents. Due to the even slower ion migration within the solution-casted electrolyte (see Figure 18 and Figure 22) these cells reach the cut-off voltage in an instant, for both charging and discharging. Therefore, as described above, the resistance values approach each other as well as a certain limit value. Since these phenomena effect the cells for all C-Rates, the R_{DC} values stay at around 21 kΩ, significantly higher compared to cell series #18 and #21.

From Figure 31 the resistance values during 5 µA cycling can be seen. Here a gap between charge and discharge resistance can be observed, similar to what has been observed for other 5 µA cycling steps, e.g., during C-Rate test. Interestingly, the values measured for the charging resistance are above the values during high C-Rate cycling. This has only been seen for cell series #26 and can also be found in Figure 28. Additionally, the gap between the resistances is smaller compared to cell series #18 and #21. This again may be caused by the much slower ion migration within cell series #26 in comparison to the other cell series.

3.3.3.3 dQ/dV investigation on possible side reactions

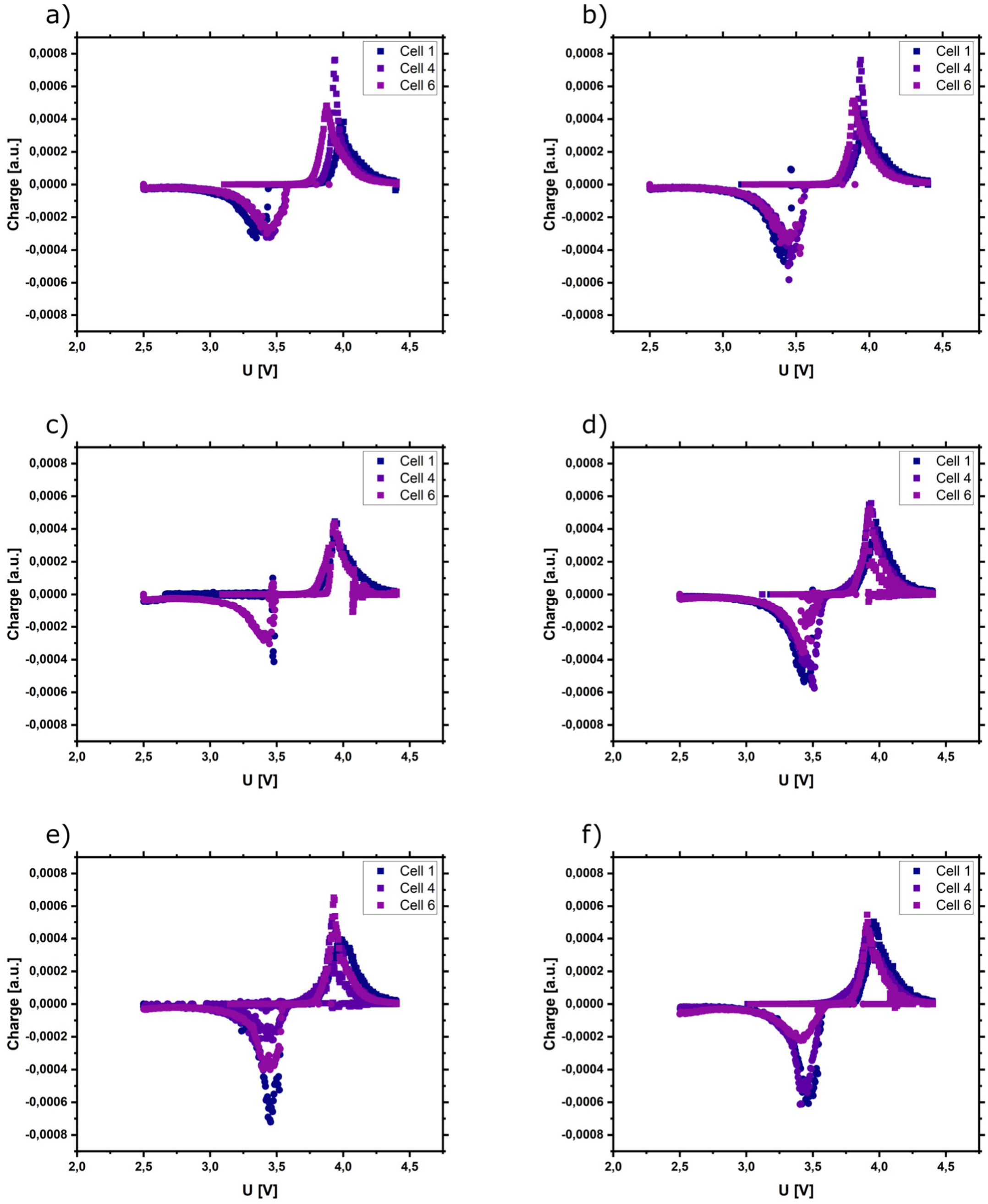

Figure 32 dQ/dV-Plots for cell series #18 during electrochemical cycling with 5 µA currents. a) Final cycle of the conditioning process b) 5µA cycling after discharge C-Rate test c) 5µA cycling after charge C-Rate test d) after 0.35C e) 0.5C and f) 1C cycling

Figure 32 show dQ/dV-plots for all individual cells of cell series #18 derived from cycling with 5 µA currents starting from the final cycle of conditioning to 1C cycling. For all plots only one peak during charging and one peak during discharging is observed.

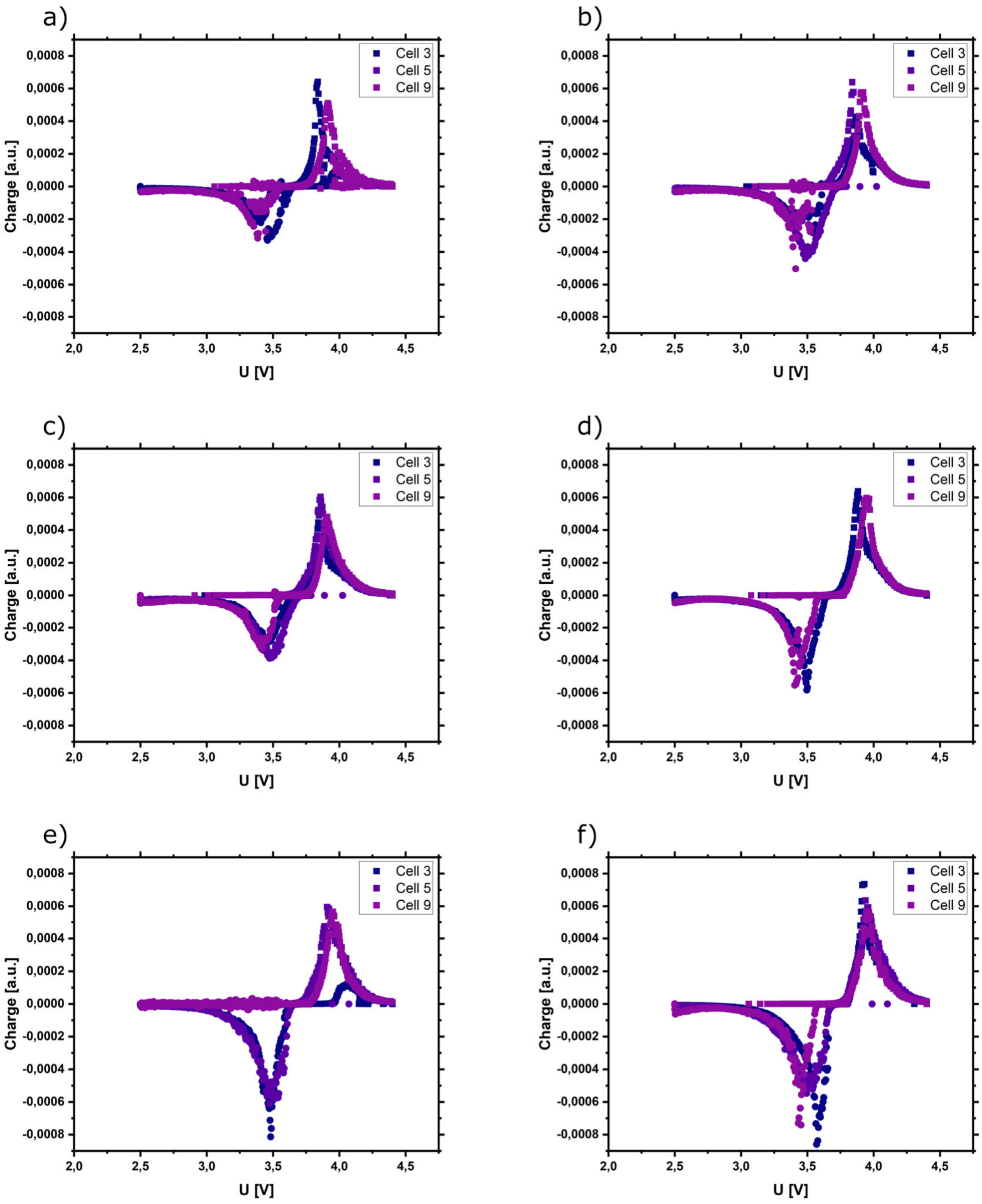

Figure 33 dQ/dV-Plots for cell series #21 during electrochemical cycling with 5 µA currents. a) Final cycle of the conditioning process b) 5µA cycling after discharge C-Rate test c) 5µA cycling after charge C-Rate test d) after 0.35C e) 0.5C and f) 1C cycling

These peaks have been identified as the NMC_{111} intercalation and deintercalation peaks, respectively. For each measurement an increase in charges being intercalated can be derived from the plots. This is in accordance with the findings in Figure 20 to Figure 25, where an increase in capacity can be found for cell series #18 during cycling with 5 µA. The shift between the peaks hints a rather large internal resistance, which is in accordance with the values reported in Figure 26 to Figure 31. Additionally, no supplementary peaks outside

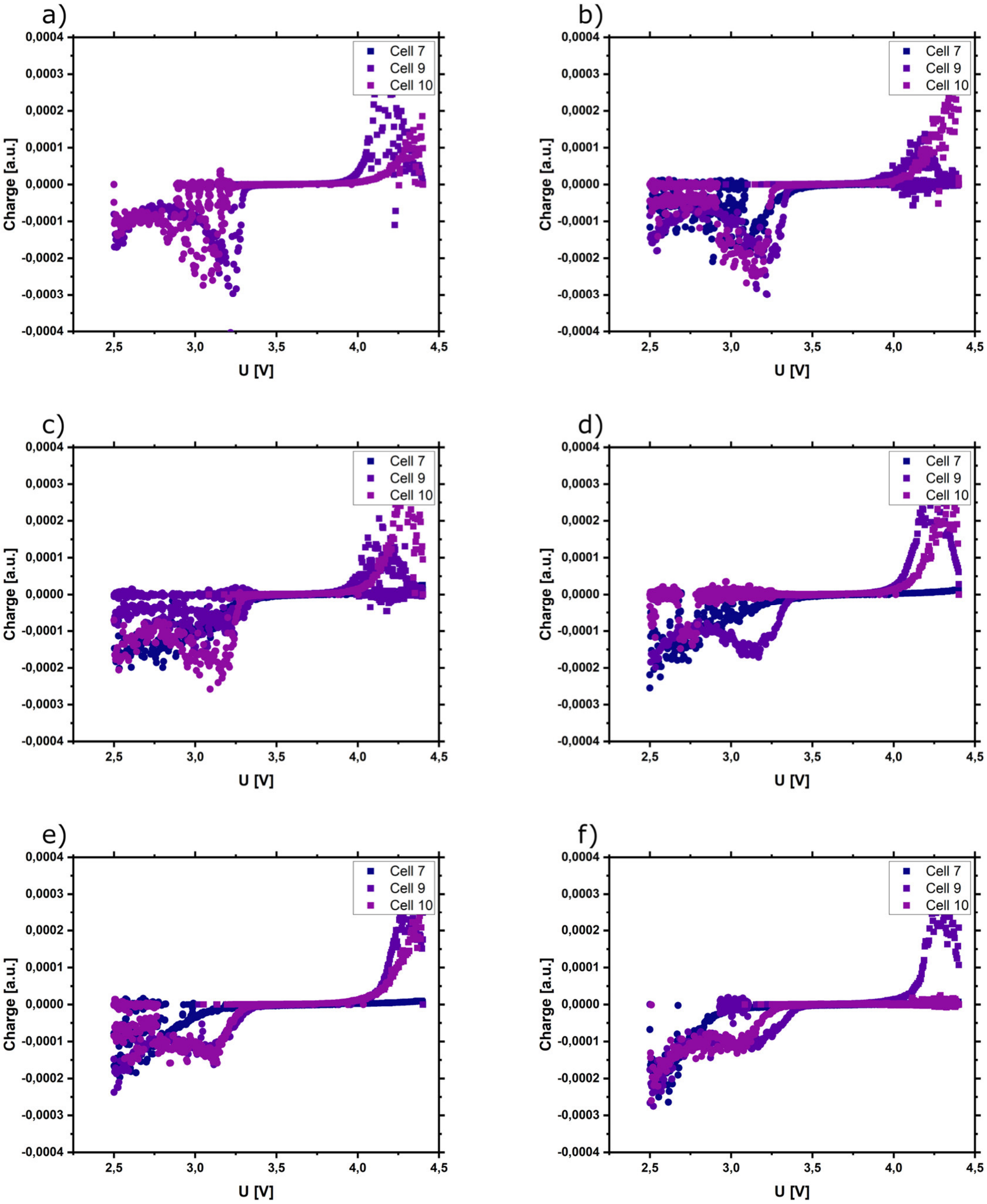

Figure 34 dQ/dV-Plots for cell series #26 during electrochemical cycling with 5 µA currents. a) Final cycle of the conditioning process b) 5µA cycling after discharge C-Rate test c) 5µA cycling after charge C-Rate test d) after 0.35C e) 0.5C and f) 1C cycling

the intercalation peaks have been found, which supports the conclusion, that no additional electrochemical reactions take place during cycling of the cells. This also applies to cell series #21 (see Figure 33).

Figure 34 shows the dQ/dV-data derived for cell series #26. In comparison to data gathered for cell series #18 and #21 the higher internal resistance with these cells can be seen. This is in accordance with the previous results. Additional peaks may be found within this data, but unfortunately the raw data gathered for this cell series showed fluctuations of voltage during charging and discharging after conditioning. While these fluctuations did not occur for cell series #18 and #21 and had no significant effect on the determination of the capacities and internal resistance values, they generate additional signal noise within the dQ/dV-plots. It is therefore not possible to make statements on additional electrochemical reactions taking place based on this data. Additionally, no countermeasures regarding an internal resistance correction have been undertaken, since the data was calculated from cycling data. This leads to the strong displacements between the intercalation peaks during charging and discharging.

To gain more information on this topic additional CV experiments after or during the cycling experiments must be conducted. Due to time limitations, these experiments were not undertaken in the course of this thesis.

3.3.4 XRD data analysis

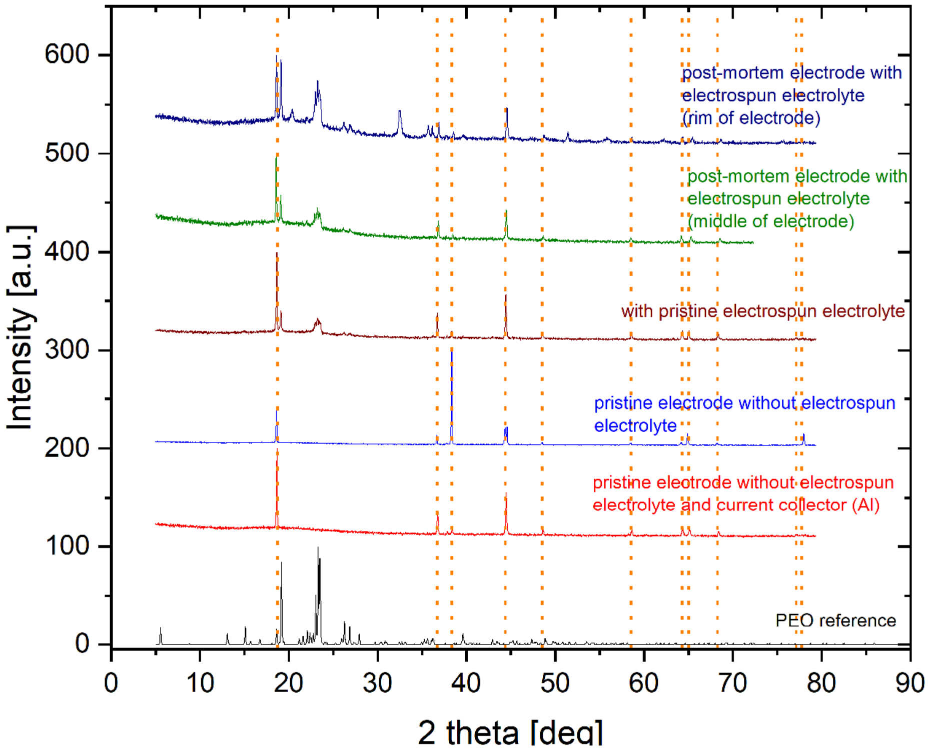

Figure 35 XRD spectra of pristine and post-mortem electrodes, both with and without electrospun PEO-based electrolytes

One observation from chapter 3.3.3 is an increase in capacity seen in all measured cells. This increase was in fact different for each individual cell, leading to the conclusion, that the increase must have been to changes within the electrode. Since the electrode binder material used in this thesis is PEO (see chapter 2.3.3), a change in the crystallinity due to the forced ion movement could be plausible. To test this hypotheses XRD measurements have been conducted on pristine and post-mortem electrodes, both with and without the electrospun PEO electrolyte. The results of these experiments can be found in . The samples have been prepared under an argon atmosphere. The sample of a pristine electrode without the electrolyte and the current collector was additionally prepared by scraping off the electrode coating from the current collector and using only the electrode powder for analysis. The powder or the electrodes, respectively, were fixed between two stripes of adhesive tape, which itself did not cause noteworthy background scattering during the XRD measurement. The reference spectrum for PEO was simulated and not measured directly.

Figure 35 shows XRD spectra of pristine and post-mortem electrodes. The dotted orange lines represent the positions of XRD reflexes for NMC_{111} which also poses as a major species within the electrode. As a reference for the peak positions the work of Yabuuichi et al. is used [124].

It can easily be seen, that for all samples intensive peaks associated with NMC_{111} are present. This poses no surprise since the electrode consists of mostly this material. Especially samples without an electrospun PEO electrolyte show no peaks other than those associated to NMC. Possible peaks coming from the PEO within the electrode coating are too weak to be seen in these samples. Therefore, no statement on the crystallinity of the PEO within the electrode coating can be made.

Samples with an electrospun PEO electrolyte do show PEO crystallinity peaks. The pristine state does not show drastic changes in the XRD spectrum compared to the post-mortem state (middle of the electrode). Both spectra measured for the post-mortem state show a slight shoulder between about 13 to 30 degrees. This might be a change due to the cycling of the cell and may be an additional explanation for the increase in ionic conductivity seen for these cells, but further investigations must be conducted for a definite statement.

The most pronounced changes can be seen for the post-mortem state at the rim of the electrode. This spectrum shows the most peaks with increased intensities for peaks associated with PEO. A possible explanation can be the pressure exerted during the punching process. Since the used punch exerts more pressure on the rim of the electrode than the middle, the fibers lose their morphology and return to a state similar to a solution-casted electrolyte with a higher degree of PEO crystallinity. Similar behavior was described by Freitag et al [18], who measured the ionic conductivity for PEO membranes under different pressures and found a decreasing ionic conductivity for increasing pressures, leading to the conclusion that the fibers lose their form and return to an solution-casted state.

3.4 Conclusions

Solid-state lithium-ion batteries were studied using PEIS and cycling experiments. From the electrochemical data gained, e.g., cycling tests, it can be seen that the cathode was not fully activated over the course of the experiments, leading to an increase of discharge capacity. The impedance measurements after each cycling experiment reveal an increase in the ionic conductivity for cycling experiments using small currents. Additionally, conditioning the cells using a constant small current for all cells leads to strong differences in both ionic conductivity after the conditioning and the cycling numbers needed to fulfill the conditioning criterium. This leads to the conclusion, that the increase in ionic conductivity is mainly dependent on the cycling currents and the cycling numbers. This effect is only observed for cells using an electrospun electrolyte; solution-casted reference cells do not show these effects. These effects may be due to an expansion of the electrodes within the system, pressing the fibers of the electrospun electrolytes into the pores, thus increasing the effective area and the ionic conductivity.

Investigations on the electrolyte/electrode interface have been intended by PEIS, but due to difficulties in defining and adjusting the SOC in the used coin cells, the data gathered may not be accurate enough to come to a safe conclusion.

Another intriguing effect is found in the cycling data. For small currents an increase in the capacity can be seen for all used cells. No additional reactions other than an increasing NMC-peak can be found in corresponding dQ/dV-plots, rendering an additional reaction (e.g., decomposition) unlikely. XRD data of post-mortem opened cells show no significant reduction of PEO crystallites within the electrode. This may lead to the conclusion, that the active materials used within the electrode may expand and therefore reduce the porosity and tortuosity, leading to shorter migration ways and more active NMC-particles.

For conducted battery tests (PEIS, cycling and C-Rate tests), the electrospun electrolytes display a superior performance compared to the solution-casted cells; especially the internal resistances are much lower for electrospun electrolytes.

More research is needed to fully understand the effects described in this thesis, especially direct measurement methods for these phenomena must be implemented.

4. Electrospun PFSA/PEO solid electrolyte for ASSBs

4.1 Introduction

In the following chapter a PFSA-based solid electrolyte and its spinning characteristics are in the focus. Different combinations of PFSA, PEO, Lithium salt and solvents are under investigation in regard to finding an optimized solution. From pre-tests it is known that PEO is needed to form fibers. A matrix of possible formulations is defined and judged based on criteria like the ability to form fibers during electrospinning, the ionic conductivity of the materials combinations (see chapter 4.2.1). The spinning results are analyzed using optical microcopy and SEM. The ionic conductivity is characterized using impedance spectroscopy of solution casted samples. To gain further insight into the materials, DSC measurements are conducted. The most suitable electrospun electrolyte is tested using electrochemical cycling within a full cell set-up.

4.2 Process development of a suitable electrolyte solution

4.2.1 Requirements to the solution

Since it is not possible to check all possible combinations of compositions, concentrations and solvents in the context of this thesis for their performance in all-solid-state lithium-ion batteries, one has to find ways to filter for promising candidates, therefore, to define requirements to the solutions or dispersions.

For this thesis, solutions or dispersions must fulfill three requirements to be as a candidate for an electrospun electrolyte:

1. The solution or dispersion must be stable for the entire electrospinning process. Otherwise, precipitating polymers can change the composition of the corresponding fibers as well as interrupt the spinning process by clogging the feed.
   To check this requirement, different possible compositions and concentrations are mixed in different solvents and are qualitatively checked for precipitating ingredients over a long period of time.

2. Furthermore, it has to be of the right concentration to be able to produce fibers under spinning conditions (e.g., relative humidity) and parameters (e.g. voltage, emitter-collector distance) realizable with the used set-up.

   In this thesis solutions or dispersions which match with the first requirement will be tried in the electrospinning process for a shorter period of time and for different spinning parameters. Possible fibers produced in this process are investigated using suitable techniques (e.g., Optical (OM) or Scanning Electron Microscopy (SEM)). In addition, solutions which show the ability to form fibers are tested in long-time electrospinning tests, to form thicker fiber mats.

3. On the other hand, the composition of the solution or dispersion has to be engineered such that the fiber material shows the desired functionality. It is not reasonable to design a solution or dispersion using a high amount of a materials, possibly as an auxiliary to tune or enable spinning, that the resulting fibers do not meet the required functionality anymore.

   This requirement will be implemented by measurement. In case there are several solutions or dispersions matching with the above-mentioned requirements, the functionality of the resulting material will be of most interest. Since the ionic conductivity defines the usefulness of a solid electrolyte, it is also our most prioritized material characteristic. It can be easily determined using Electrochemical Impedance Spectroscopy (EIS).

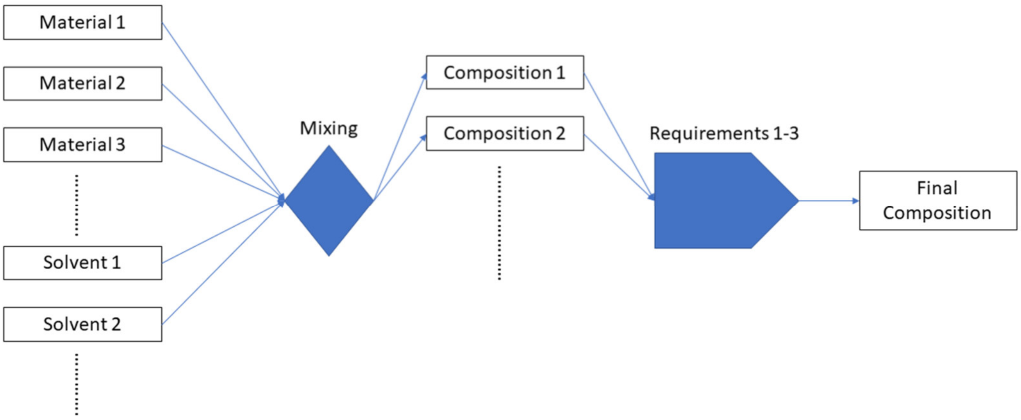

Figure 36 Schematic used for narrowing down possible compositions used in this thesis

4.2.2 Experimental

Table 12 shows all the used PFSA solution formulations used in this thesis. To calculate the necessary lithium salt, ratios between lithium and ethylene oxide units (Li/EO) and sulfonic acid units (Li/SA) have been set to 1/1 Li/EO and 1.2/1 Li/SA.

The main reason for this high lithium contents is a possible ion exchange between the sulfonic acid and the lithium. The contents have been chosen in a way to ensure an excess of lithium ions even in case that all sulfonic acid units and all ethylene oxide units have been fully coordinated with lithium. The solution concentration mentioned in Table 12 refers to the total solids content in relation to the solvent.

PFSA solution parameters			
Solution concentration	Solvent	Weight percentage PFSA/PEO	Solution Code
5 wt%	Deionized water	9/1	1.1.1
10 wt%	Deionized water	9/1	1.1.2
15 wt%	Deionized water	9/1	1.1.3
5 wt%	Deionized water/Ethanol	9/1	1.2.1
10 wt%	Deionized water/Ethanol	9/1	1.2.2
15 wt%	Deionized water/Ethanol	9/1	1.2.3
5 wt%	Ethanol	9/1	1.3.1
10 wt%	Ethanol	9/1	1.3.2
15 wt%	Ethanol	9/1	1.3.3
5 wt%	Deionized water	19/1	2.1.1
10 wt%	Deionized water	19/1	2.1.2
15 wt%	Deionized water	19/1	2.1.3
5 wt%	Deionized water/Ethanol	19/1	2.2.1
10 wt%	Deionized water/Ethanol	19/1	2.2.2
15 wt%	Deionized water/Ethanol	19/1	2.2.3
5 wt%	Ethanol	19/1	2.3.1
10 wt%	Ethanol	19/1	2.3.2
15 wt%	Ethanol	19/1	2.3.3
5 wt%	Deionized water	99/1	3.1.1
10 wt%	Deionized water	99/1	3.1.2
15 wt%	Deionized water	99/1	3.1.3
5 wt%	Deionized water/Ethanol	99/1	3.2.1
10 wt%	Deionized water/Ethanol	99/1	3.2.2
15 wt%	Deionized water/Ethanol	99/1	3.2.3
5 wt%	Ethanol	99/1	3.3.1
10 wt%	Ethanol	99/1	3.3.2
15 wt%	Ethanol	99/1	3.3.3

Table 12 PFSA solutions investigated in this thesis; the Li/ethylene oxide ratio is fixed at 1/1 and the Li/sulfuric acid is fixed at 1.2/1 for all solutions

4.2.2.1 Scanning electron microscopy

For scanning electron microscopy, a Zeiss Merlin VP compact (Carl Zeiss Jena GmbH, Jena, Germany) with a secondary electron detector was used. The acceleration voltage for the electrons was chosen to be in the range of 1 to 1.5 kV in order to avoid electrostatic charging on the polymers. The chosen aperture size was 30 µm for all experiments. All experiments have been conducted under high vacuum. The same set-up and parameters are used to analyze the PEO fibers, as described in chapter 3.2.1.

The samples for both optical and scanning electron microscopy have been prepared under normal atmosphere, but storage as well as transport have been conducted under argon atmosphere. SEM samples have been punched using a punching iron of 10 mm diameter to fit the sample holders used in the SEM.

For analyzing microscopy data freeware software Fiji and ImageJ have been used.

4.2.2.2 Impedance spectroscopy

Impedance measurements have been conducted using an Autolab PGSTAT204 (Metrohm AG, Herisau, Switzerland) potentiostat. The frequency range for all PEIS experiments was set to be 100 kHz to 10 mHz. The cells were connected to the potentiostat by using a coin cell holder as shown in Figure 9.

Impedance measurements included the following steps:

1. Open circuit voltage (OCV) measurement
2. Relaxation period for two hours; accompanied with an OCV measurement
3. Impedance measurement

The data analysis and fitting were conducted with EC-Lab V10.44 software (Biologic, Seyssinet-Pariset, France) using its Z-Fit function.

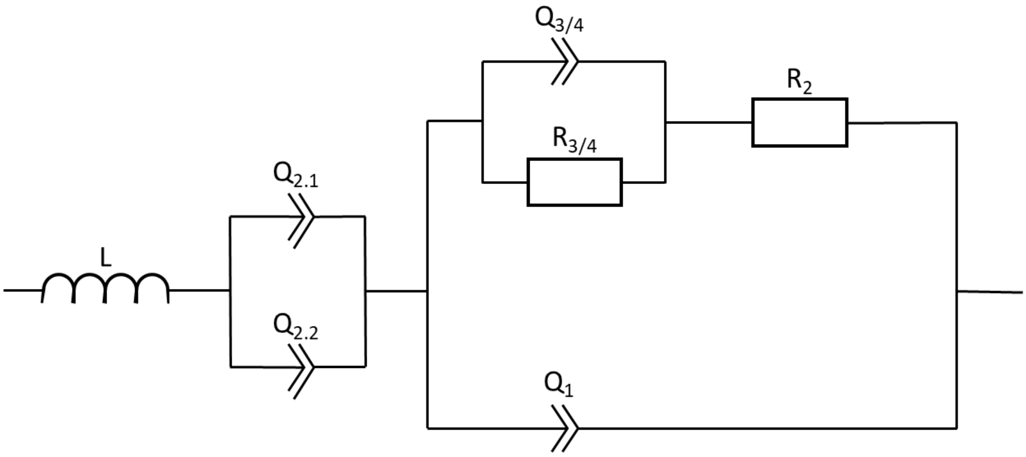

Figure 37 Equivalent circuit model used for fitting impedance spectra of solution-casted PFSA-based electrolytes

Due to a differing cell structure compared to the cells presented in chapter 3, a differing impedance model is used (see Figure 37). The nomenclature of this model has been adapted to show the similarities as well as the differences to Figure 14. The main contributions are:

- Two capacitances $Q_{2.1}$ and $Q_{2.2}$, which account for polarization of the electrolyte, behaving differently at the two electrodes; this may be due to the manufacturing process, where solution is drop-casted onto one electrode and the second one is added after drying
- Inductance L: Accounts for the inductance of the experimental set-up
- Capacitance Q_1: Geometric capacitance of the cell
- Capacitance $Q_{3/4}$: Electrode-electrolyte interface capacitance
- Resistance $R_{3/4}$: Electrode-electrolyte interface resistance
- Resistance R_2: Bulk electrolyte resistance

4.2.2.3 Determination of transference numbers

Transference numbers are determined using an Autolab PGSTAT204 (Metrohm AG, Herisau, Switzerland) potentiostat. The determination Transference number measurements included the following steps:

1. Open circuit voltage (OCV) measurement
2. Application of voltage to counter previous polarization
3. Open circuit voltage (OCV) measurement
4. First impedance measurement
5. Open circuit voltage (OCV) measurement
6. Application of 0.1 V voltage step and recording of the current response over a time period of 2 hours
7. Open circuit voltage (OCV) measurement
8. Second impedance measurement

The transference number is then calculated using the Bruce-Vincent method [94]:

$$t^{+} = \frac{I_{SSC}(\Delta V - I_0 R_0)}{I_0(\Delta V - I_{SSC} R_{SSC})} \qquad \textit{Eq. 7}$$

ΔV is a small voltage used to polarize the sample. This voltage induces a current response, which is measured until the current reaches a steady state. I_0 refers to the current measured immediately after the sample polarization, while I_{SSC} describes the current of the sample in a steady state after polarization. R_0 is the resistance of the electrolyte determined by fitting the impedance spectrum obtained during the first impedance measurement; analogous, R_{SSC} is determined from the second impedance measurement. All impedance data was fitted using the model described in Figure 37.

4.2.3 Results and Discussion

4.2.3.1 Long-term stability of the solutions

PFSA solution parameters

Solution concentration	Solvent	Weight percentage PFSA/PEO	Solution Code
5 wt%	Deionized water	9/1	🟥 1.1.1
10 wt%	Deionized water	9/1	🟩 1.1.2
15 wt%	Deionized water	9/1	🟩 1.1.3
5 wt%	Deionized water/Ethanol	9/1	🟩 1.2.1
10 wt%	Deionized water/Ethanol	9/1	🟩 1.2.2
15 wt%	Deionized water/Ethanol	9/1	🟩 1.2.3
5 wt%	Ethanol	9/1	🟩 1.3.1
10 wt%	Ethanol	9/1	🟩 1.3.2
15 wt%	Ethanol	9/1	🟥 1.3.3
5 wt%	Deionized water	19/1	🟥 2.1.1
10 wt%	Deionized water	19/1	🟥 2.1.2
15 wt%	Deionized water	19/1	🟥 2.1.3
5 wt%	Deionized water/Ethanol	19/1	🟩 2.2.1
10 wt%	Deionized water/Ethanol	19/1	🟩 2.2.2
15 wt%	Deionized water/Ethanol	19/1	🟩 2.2.3
5 wt%	Ethanol	19/1	🟩 2.3.1
10 wt%	Ethanol	19/1	🟩 2.3.2
15 wt%	Ethanol	19/1	🟩 2.3.3
5 wt%	Deionized water	99/1	🟥 3.1.1
10 wt%	Deionized water	99/1	🟥 3.1.2
15 wt%	Deionized water	99/1	🟥 3.1.3
5 wt%	Deionized water/Ethanol	99/1	🟩 3.2.1
10 wt%	Deionized water/Ethanol	99/1	🟩 3.2.2
15 wt%	Deionized water/Ethanol	99/1	🟩 3.2.3
5 wt%	Ethanol	99/1	🟩 3.3.1
10 wt%	Ethanol	99/1	🟩 3.3.2
15 wt%	Ethanol	99/1	🟩 3.3.3

Table 13 Solutions meeting the stability criterium (green); failed solutions (red)

Since the electrospinning process can take up to 12 h to produce a fiber mat of suitable thickness to be used as a solid-state electrolyte, the solutions have to be stable for at least 12 h under room temperature (see requirement 1, chapter 4.2.1). To test the stability, a small amount, usually around 5 ml of the solution in question, is prepared in a glass vile. The vile is then placed inside the fume cupboard overnight. To be able to determine the time, when an unstable solution starts to fail, a camera is set up to take a picture every ten seconds. The first and the last picture for each solution can be found in the appendix (see Solution stability).

All solutions meeting the stability criterium can be found in Table 13.

4.2.3.2 Impedance spectroscopy of solution-casted mixtures

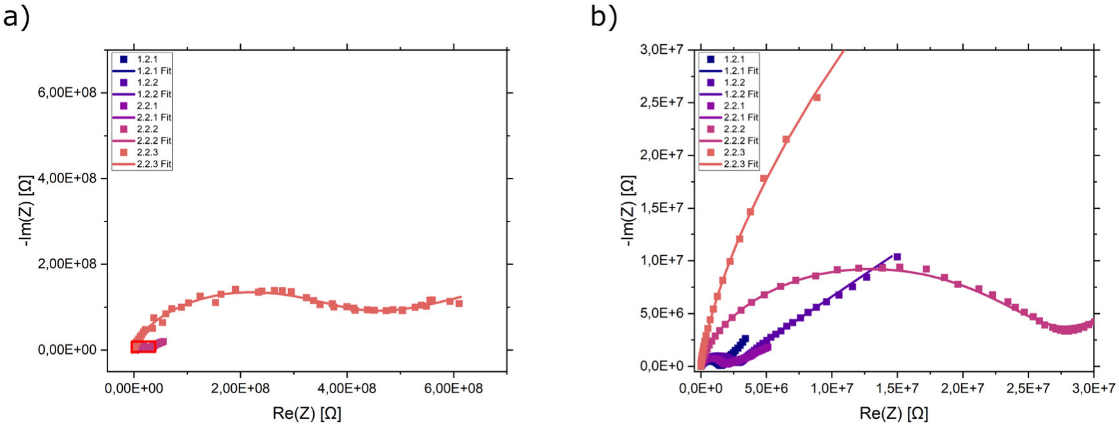

Figure 38 a) Impedance spectra for PFSA-based solution-casted electrolytes b) Zoom-in of impedance spectra marked by the red box in a)

Figure 38 shows the impedance spectra measured for spinnable solution-casted impedance samples from spinnable mixtures (see Table 15). These spectra are gained during the transference number measurement after the polarization step (see 4.2.2.3). The measured cells are structured in a different way compared to chapter 3; while in chapter 3 full cells have been constructed, here symmetric cells comprising from two stainless steel electrodes and the drop-casted electrolyte are built. Therefore, no cycling experiments nor any kind of conditioning have been conducted with these cells.

Compared to the electrospun PEO membranes investigated in chapter 3.2.2, these samples show a highly increased resistance. Especially the sample for mixture 2.2.3 shows a very large semi-circle as well as a very high scattering of data points for high impedance. A possible explanation can be that the currents measured by the potentiostat reached its resolution limit. The data measured for all other samples does not show such pronounced scattering and were fitted nicely by the equivalent circuit model proposed in Figure 37.

Solution	Ionic conductivity [S/cm]	Transference number
1.2.1	$4.66 \times 10^{-10} \pm 1.16 \times 10^{-10}$	$1.80 \times 10^{-10} \pm 2.69 \times 10^{-6}$
1.2.2	$9.90 \times 10^{-8} \pm 2.15 \times 10^{-10}$	$8.15 \times 10^{-10} \pm 1.49 \times 10^{-5}$
2.2.1	$1.12 \times 10^{-7} \pm 2.38 \times 10^{-8}$	$1.33 \times 10^{-9} \pm 3.73 \times 10^{-4}$
2.2.2	$7.80 \times 10^{-9} \pm 5.43 \times 10^{-9}$	$1.99 \times 10^{-10} \pm 4.18 \times 10^{-5}$
2.2.3	$1.07 \times 10^{-9} \pm 4.39 \times 10^{-10}$	$6.23 \times 10^{-13} \pm 4.88 \times 10^{-6}$

Table 14 Ionic conductivities and transference numbers for PFSA-based electrolytes

The ionic conductivities as well as the transference numbers are shown in Table 14. The ionic conductivities prove to be quite low for all measured samples. The highest ionic conductivity is found for solution 2.2.1, being in the magnitude of a solution-casted PEO electrolyte at room temperature. A possible explanation could be a strong coordination of the lithium ions to the sulfonic acid groups from the PFSA polymer. In a dry state, like in this thesis, the chain mobility of the PFSA may also be reduced drastically. This may result in an overall low ionic conductivity.

The measured transference number is far below the transference number of 0.2 to 0.6 [94] for PEO. Again, a possible explanation might be a strong coordination of lithium ions to the sulfonic acid groups as well as a hindered chain mobility. To gain further insight, NMR experiments on this system are proposed to measure the activation energy for lithium-ion transport.

The transference numbers calculated for this system generally seem to be problematic. The calculated errors for the transference numbers are several orders of magnitude higher than the actual transference number. This can be explained by the measurement system itself. The main contribution to the error calculation comes from the small variation in the polarization voltage from the measurement system. The exact error calculation can be found in the appendix (see Error calculation for transference numbers).

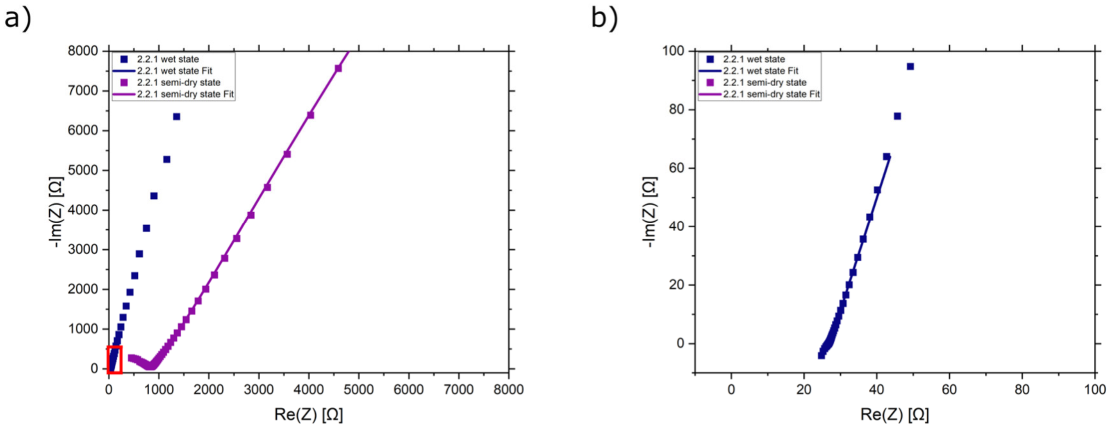

Figure 39 Impedance spectra for PFSA solution 2.2.1 in a) semi-dry and b) wet state

Impedance measurements conducted with insufficiently dried solution-casted samples of solution 2.2.1 showed a much better performance (see Figure 39). Unfortunately, due to the soft nature of these electrolytes, no sufficient thickness measurement was possible and thus the ionic conductivity was not determined reliably. Therefore, PFSA-based electrolytes may be a candidate for new functionalized gel polymer electrolytes.

4.3 Analysis of electrospun. PFSA/PEO electrolyte

4.3.1 Fiber morphology

PFSA solution parameters

Solution concentration	Solvent	Weight percentage PFSA/PEO	Solution Code
10 wt%	Deionized water	9/1	🟥 1.1.2
15 wt%	Deionized water	9/1	🟥 1.1.3
5 wt%	Deionized water/Ethanol	9/1	🟩 1.2.1
10 wt%	Deionized water/Ethanol	9/1	🟩 1.2.2
15 wt%	Deionized water/Ethanol	9/1	🟥 1.2.3
5 wt%	Ethanol	9/1	🟥 1.3.1
10 wt%	Ethanol	9/1	🟥 1.3.2
5 wt%	Deionized water/Ethanol	19/1	🟩 2.2.1
10 wt%	Deionized water/Ethanol	19/1	🟩 2.2.2
15 wt%	Deionized water/Ethanol	19/1	🟩 2.2.3
5 wt%	Ethanol	19/1	🟥 2.3.1
10 wt%	Ethanol	19/1	🟥 2.3.2
15 wt%	Ethanol	19/1	🟥 2.3.3
5 wt%	Deionized water/Ethanol	99/1	🟥 3.2.1
10 wt%	Deionized water/Ethanol	99/1	🟥 3.2.2
15 wt%	Deionized water/Ethanol	99/1	🟥 3.2.3
5 wt%	Ethanol	99/1	🟥 3.3.1
10 wt%	Ethanol	99/1	🟥 3.3.2
15 wt%	Ethanol	99/1	🟥 3.3.3

Table 15 Solutions forming fibers (green); failed solutions (red)

In the following chapter, electrospinning experiments using PFSA-based solutions are conducted, following requirement 2 from chapter 4.2.1. Starting from the solutions identified in chapter 4.2.3.1, different spinning parameter combinations (see Table 11) are tested for a short amount of spinning time (around three minutes). Immediately afterwards the fiber samples are subjected to optical microscopy to determine whether fibers have been electrospun or not. In case of fibers, SEM samples are prepared as described in chapter 4.2.2.1 for further characterization.

These experiments further reduced the number of solutions of interest for this study, since fibers are not found for some of them. All material combinations, which form fibers are listed in Table 15.

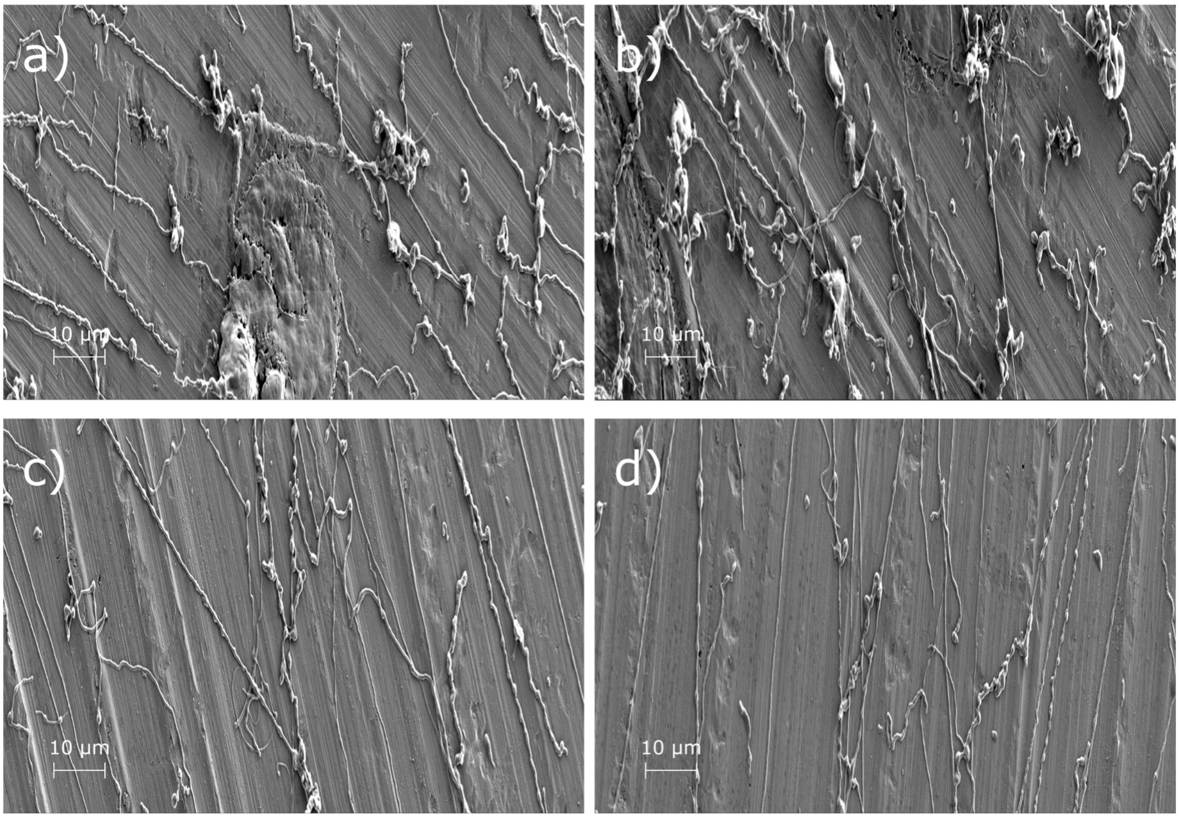

Figure 40 SEM pictures for spinning solution 1.2.1 a) 20 kV, 100 mm, b) 30 kV, 100 mm, c) 30 kV, 150 mm, d) 30 kV, 200 mm

Figure 40, Figure 42, Figure 44, Figure 46 and

Figure 48 show SEM pictures of different spinning solutions under various spinning parameter conditions. All samples have been spun for a time period of 10 min. Longer spinning experiments have been conducted and are described below. These experiments aim to confirm successful fiber creation under the respective solution/parameter combination. All shown SEM pictures were taken at a magnification of 1000. Additional SEM pictures can be found in the appendix.

Figure 41, Figure 43, Figure 45, Figure 47 and Figure 49 show the histograms of the measured fiber diameters. The diameters were measured using Fiji software, using the measurement tool. For each solution/parameter combination, SEM pictures have been taken on three different sites of the punched SEM sample. All three SEM pictures have been considered for randomly choosing the fibers to be measured.

Solution 1.2.1

Figure 40 shows that solution 1.2.1 is able to form fibers for electric field strength between 2-3 kV/cm. For emitter-collector distances below 150 mm, droplets can be found on the substrate. The fibers themselves seem to be quite inhomogeneous for all tested parameters. Especially for Figure 40 d) a tendency to form aligned, beaded fibers can be

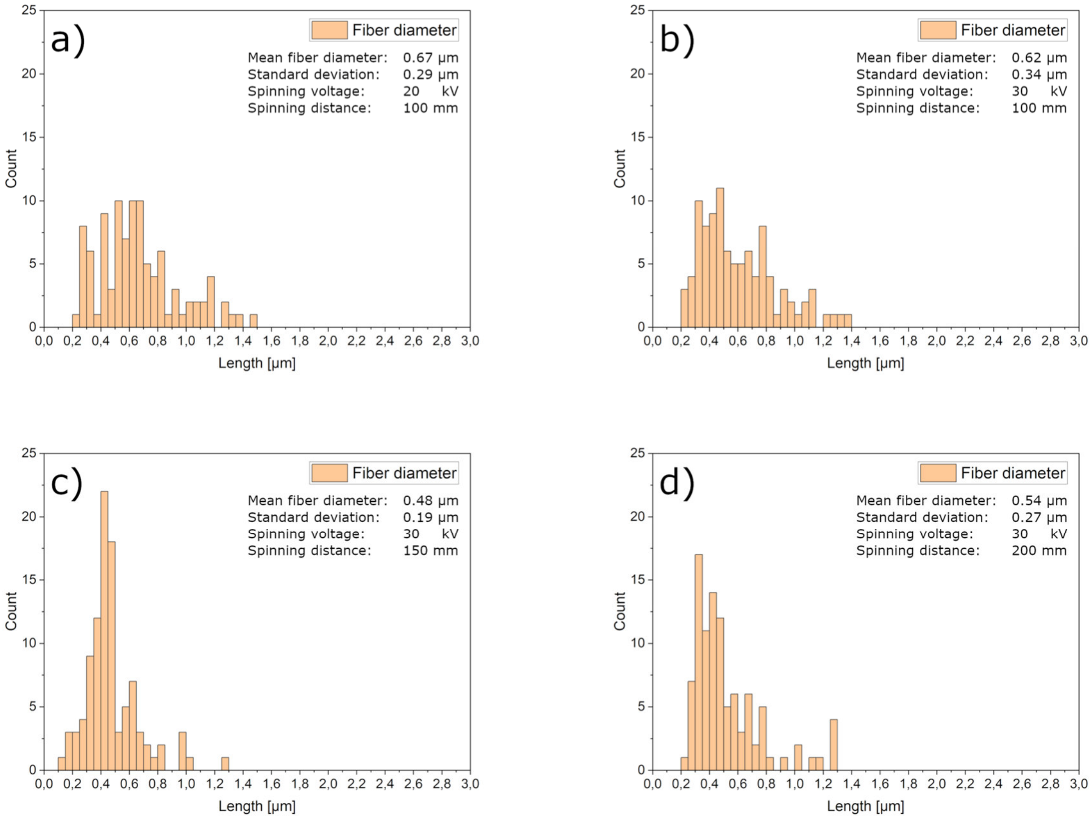

Figure 41 Histograms of measured fiber diameters for spinning solution 1.2.1

seen. In addition, all fibers seem to be wet at the collector, resulting in a suitable adhesion to the aluminum. Note that the degree of coverage is quite poor for all tested parameters. The fibers also seem to have quite small diameters. This impression is supported by the fiber diameter measurements. Figure 41 shows the histograms corresponding to the pictures shown in Figure 40. It can be seen, that the fiber diameters do not exceed 1.6 µm. The majority of the fibers even show diameters far below 1 µm. It seems that the fiber diameters are in this case governed by the emitter-collector distance. Figure 41 a) and b) show similar mean diameters and similar fiber morphologies (see Figure 40 a) and b)), despite a difference of 1 kV/cm in electric field strength. The smallest mean fiber diameter can be found for 30 kV at a spinning distance of 150 mm. These parameters also produce the most homogeneous fiber diameters with a mean of 0.48 µm. Fibers with a diameter of more than 0.8 µm usually result from the agglomeration of smaller fibers before laying down onto the collector. This may be seen from SEM pictures within the appendix.

Overall, the fiber morphology and the fiber diameters for solution 1.2.1 does not show tremendous variations within the tested parameters. Parameter combinations mentioned in Table 11 but are not mentioned in this chapter have been tested but did not produce a fiber jet and have therefore been deemed a failure combination.

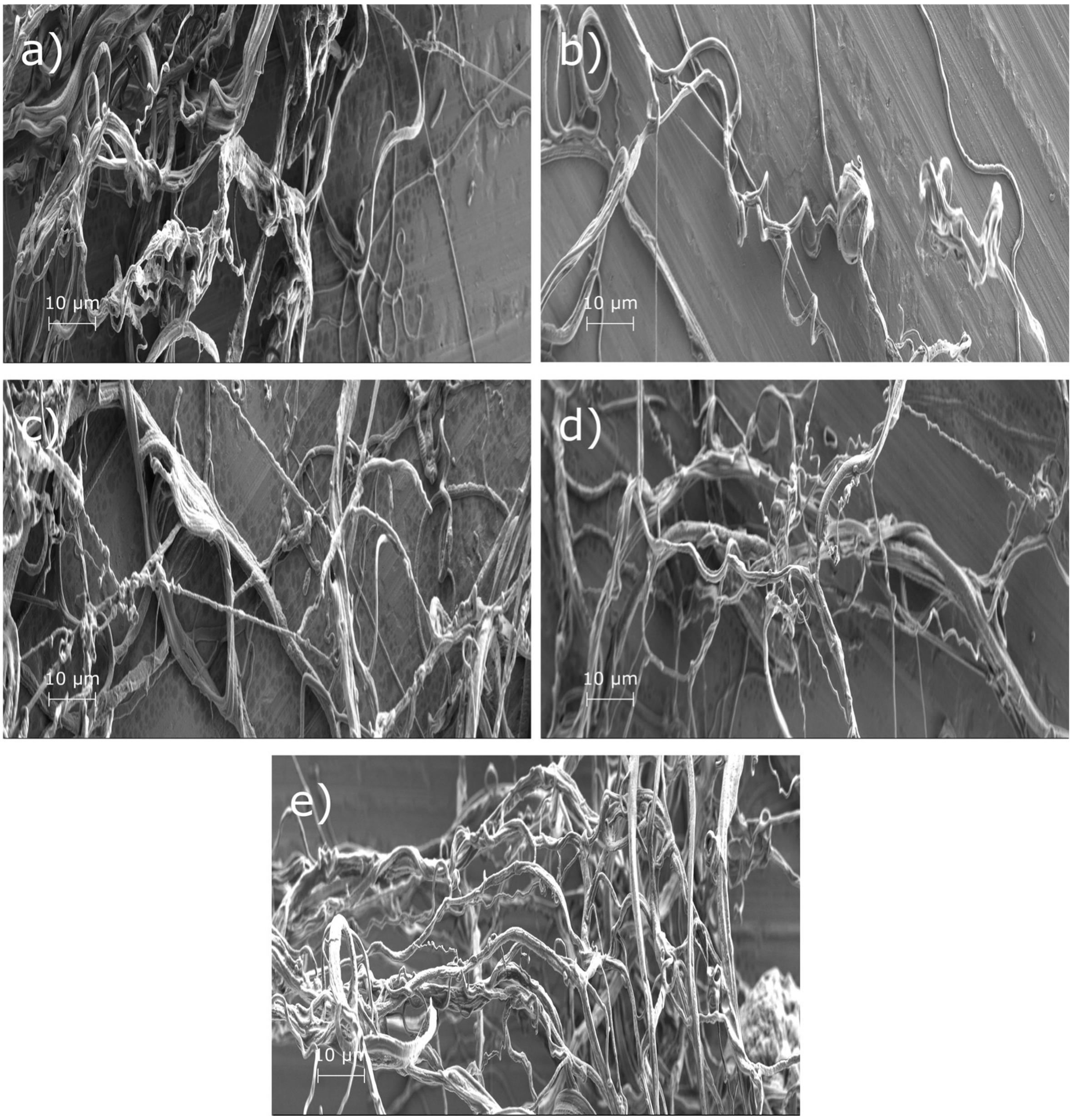

Figure 42 SEM pictures for spinning solution 1.2.2 a) 20 kV, 100 mm, b) 20 kV, 150 mm, c) 30 kV, 100 mm, d) 30 kV, 150 mm, e) 30 kV, 200 mm

Solution 1.2.2

Figure 42 shows the fibers formed by solution 1.2.2 using electric field strengths from 1.33 up to 3 kV/cm. Compared to the fibers depicted in Figure 40, an extensive change in the fiber morphology is seen. While the fibers for solution 1.2.1 seem to still be wet when reaching the collector, solution 1.2.2 creates dry fibers. Throughout all tested parameters, the fibers even seem to form three-dimensional structures or webs. From additional pictures at different magnifications (see appendix Additional SEM data of PFSA-based electrospun samples), it can be deducted, that these fibers tend to agglomerate, since the fibers are not

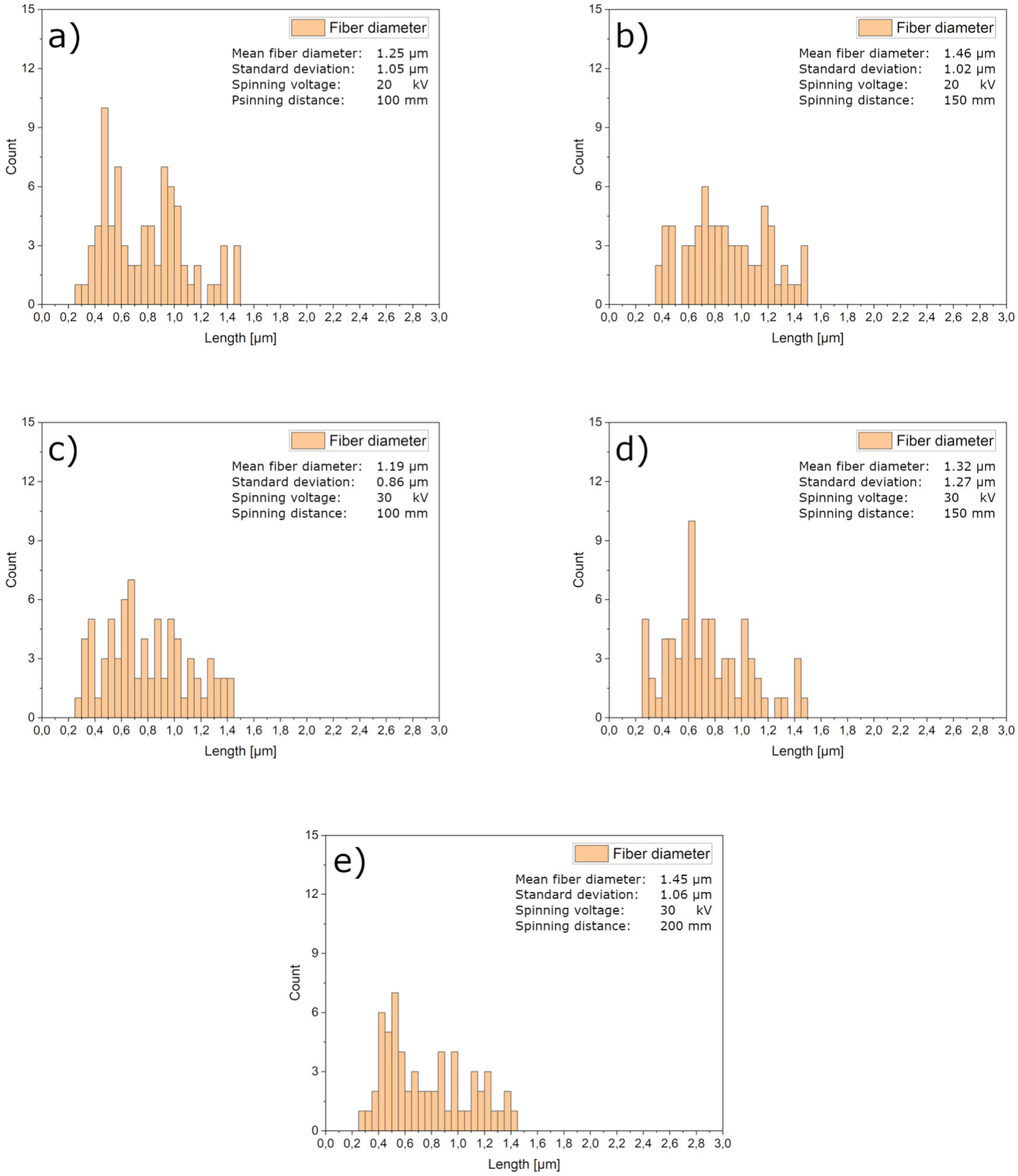

Figure 43 Histograms for measured fiber diameters for spinning solution 1.2.2

evenly distributed on the collector. A possible explanation could be a residual electrostatic charge of the fibers on the collector, which would influence follow-up fibers towards areas with lower electrostatic charges. The fibers themselves show a quite inhomogeneous morphology. Some fibers show a flat-ribbon like structure, with a very uneven surface. This can lead to the conclusion, that these fibers are in fact smaller fibers fused together during the early stages of the electrospinning process. The build-up of agglomerates as depicted in Figure 42 indicate residual electrostatic charges within the fibers, posing as a possible explanation for the high distances between single fibers and the loose-packed structure of the fiber agglomerates.

Due to the tendency to fuse fibers, the measured fiber diameter distributions (see Figure 43) are expected to be quite broad. Even if the maximum fiber diameters measured are in the same interval as for solution 1.2.1, between 0.2 and 1.4 µm, distributions of the fiber diameters are much broader (standard deviation close to the values of the mean diameter). This shows again the tendency for fiber fusion.

Solution 2.2.1

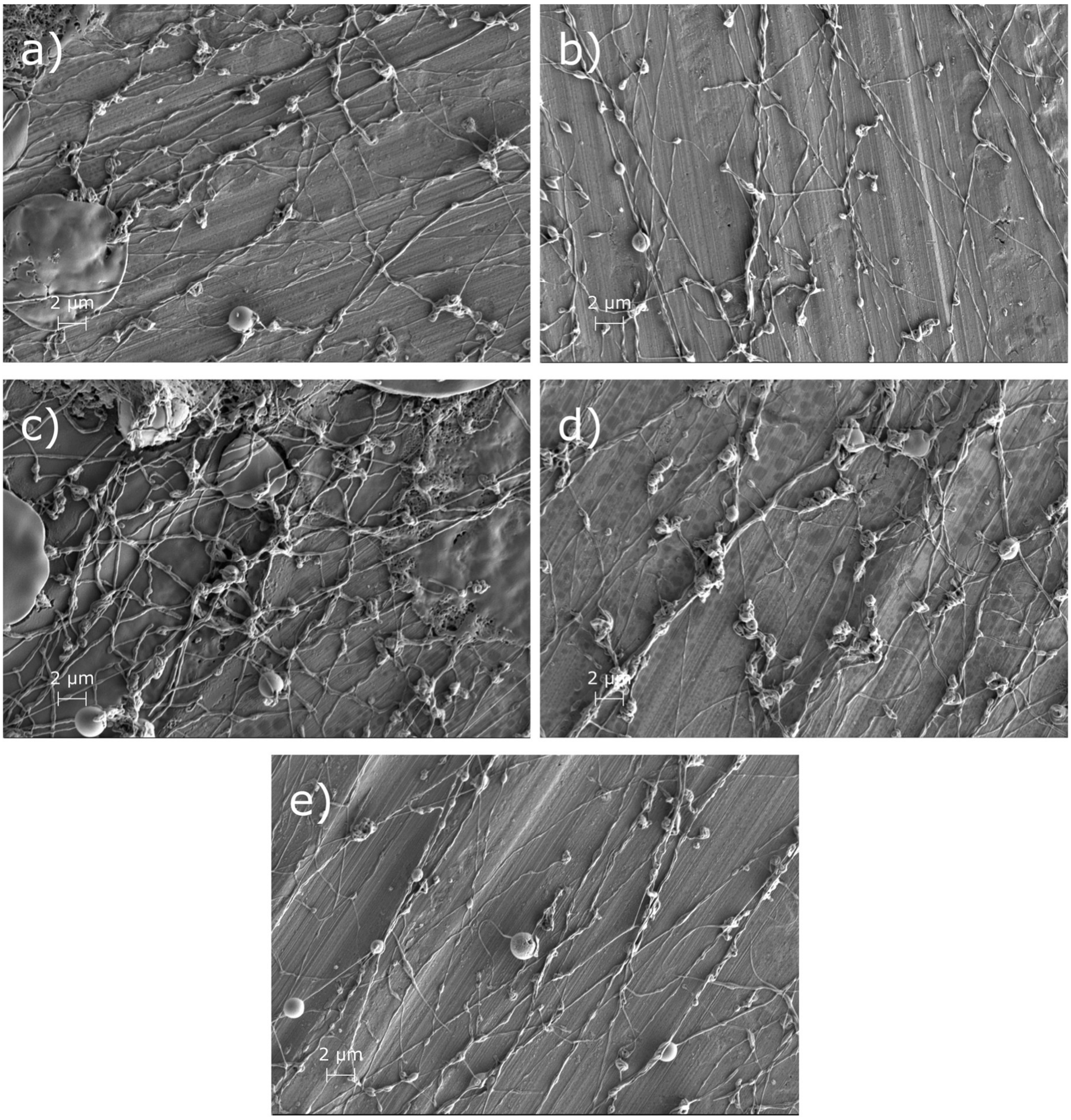

Figure 44 SEM pictures for spinning solution 2.2.1 a) 20 kV, 100 mm, b) 20 kV, 150 mm, c) 30 kV, 100 mm, d) 30 kV, 150 mm, e) 30 kV, 200 mm

Figure 44 shows SEM pictures of fibers from solution 2.2.1. Note that these pictures are at a magnification of 3000, compared to the SEM pictures beforehand. These fibers partly resemble fibers from solution 1.2.1, which is due to the overall polymer concentration (5 wt% for solutions 1.2.1 and 2.2.1), which may be on the lower limit for electrospinning. Especially solution 2.2.1 tends to the formation of quite big droplet on the collector, as well as the formation of beaded fibers (e.g., as in Figure 44 b)), both indicators for a too low polymer concentration. The fiber created with this solution are very inhomogeneous and stick to the

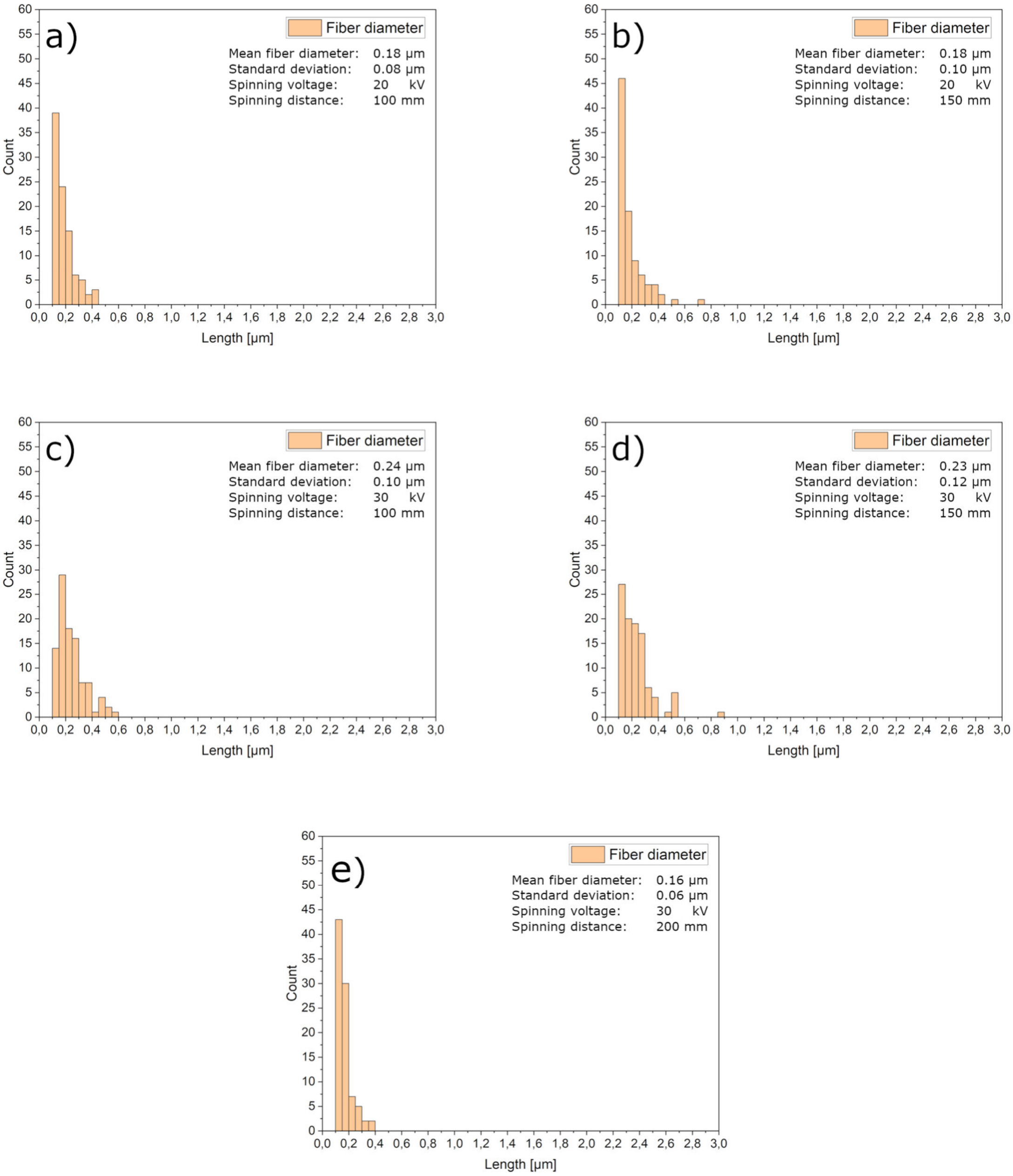

Figure 45 Histograms for measured fiber diameters for spinning solution 2.2.1

aluminum foil on the current collector. In comparison to solution 1.2.1, the fiber beads are more pronounced here. A possible explanation is, that the proportion of PEO in solution 2.2.1 lower. Since PFSA usually requires a carrier polymer for electrospinning [35], PEO content is to a paramount importance for the fiber morphology. Decreasing the PEO content, while fixing the overall polymer concentration, will lead to a reduced concentration of the fiber-building polymer, thus increase the chance to form beaded fibers and droplets.

The fiber diameters are much smaller compared to fibers formed from solutions 1.2.1 and 1.2.2 (see Figure 45). Within the tested parameters, the fiber diameters vary from a mean0.16 and 0.24 µm. Fibers of diameters greater 1 µm have not been found.

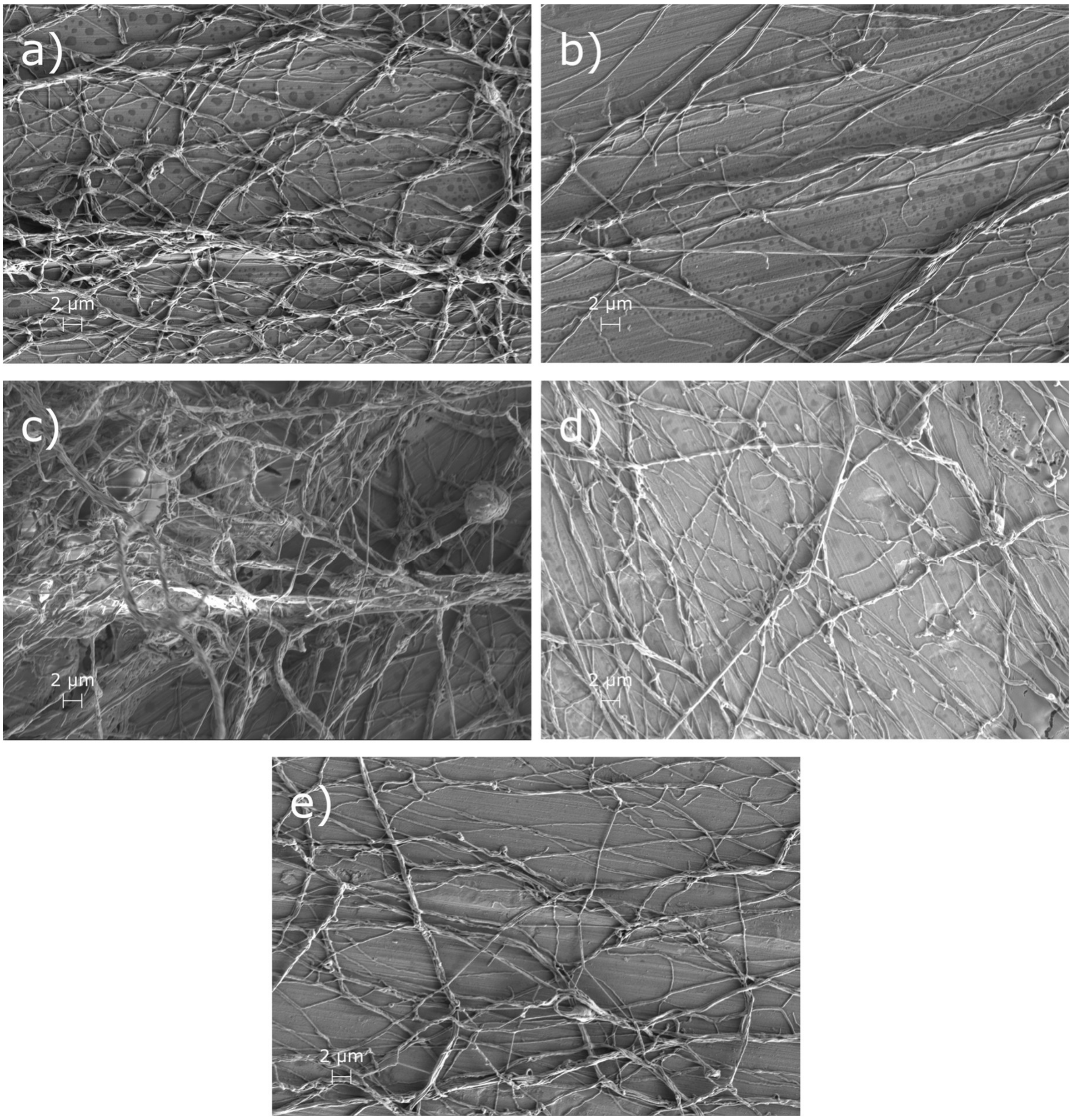

Figure 46 SEM pictures for spinning solution 2.2.2 a) 20 kV, 100 mm, b) 20 kV, 150 mm, c) 30 kV, 100 mm, d) 30 kV, 150 mm, e) 30 kV, 200 mm

Solution 2.2.2

Figure 46 shows SEM pictures of spinning fibers gained from solution 2.2.2. The shown pictures were taken at a magnification of 2000. These fibers resemble the fibers gained from solution 1.2.2, but they are much smaller in diameter (Mean fiber diameter for solution 1.2.2: 1.19 to 1.45 µm). In addition, fibers created from solution 2.2.2 appear to be more homogeneous. From additional pictures at various magnifications (see appendix) it can be seen that these fibers tend to have less and smaller agglomerates of fibers compared to

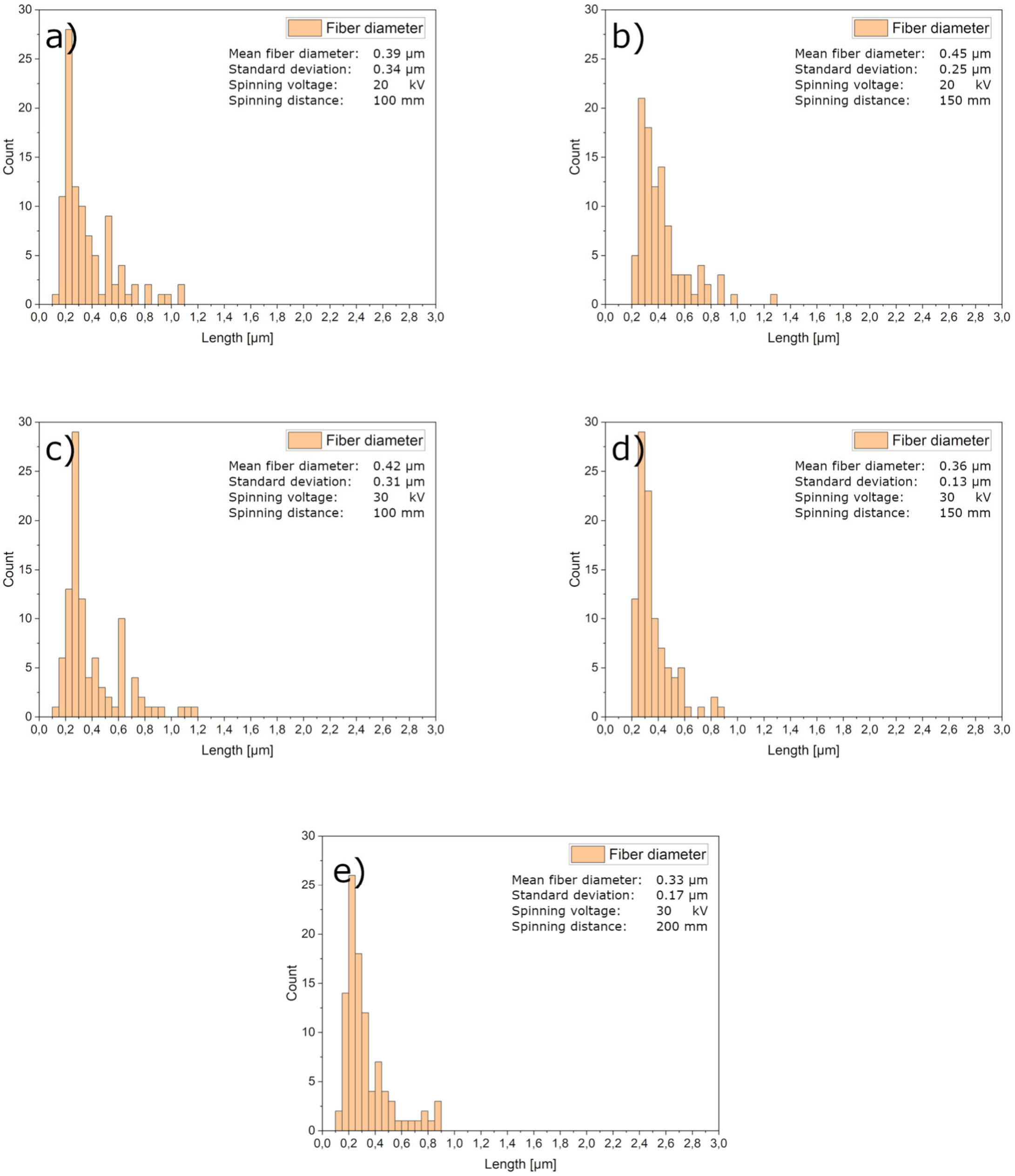

Figure 47 Histograms for measured fiber diameters for spinning solution 2.2.2

solution 1.2.2. The spinning result appears to be much more homogeneous over the entire SEM sample. It is also notable, that the fibers from solution 2.2.2 tend to less loose-packed structures as solution 1.2.2. An exception to this is spinning at 30 kV with a distance of 100 mm. With these parameters, loose-packed structures become possible again. This leads to the conclusions, that 100 mm distance is not sufficient to get rid of the majority of the electrostatic and that a higher PFSA content in relation to the PEO content is beneficial to the spinning fiber formation.

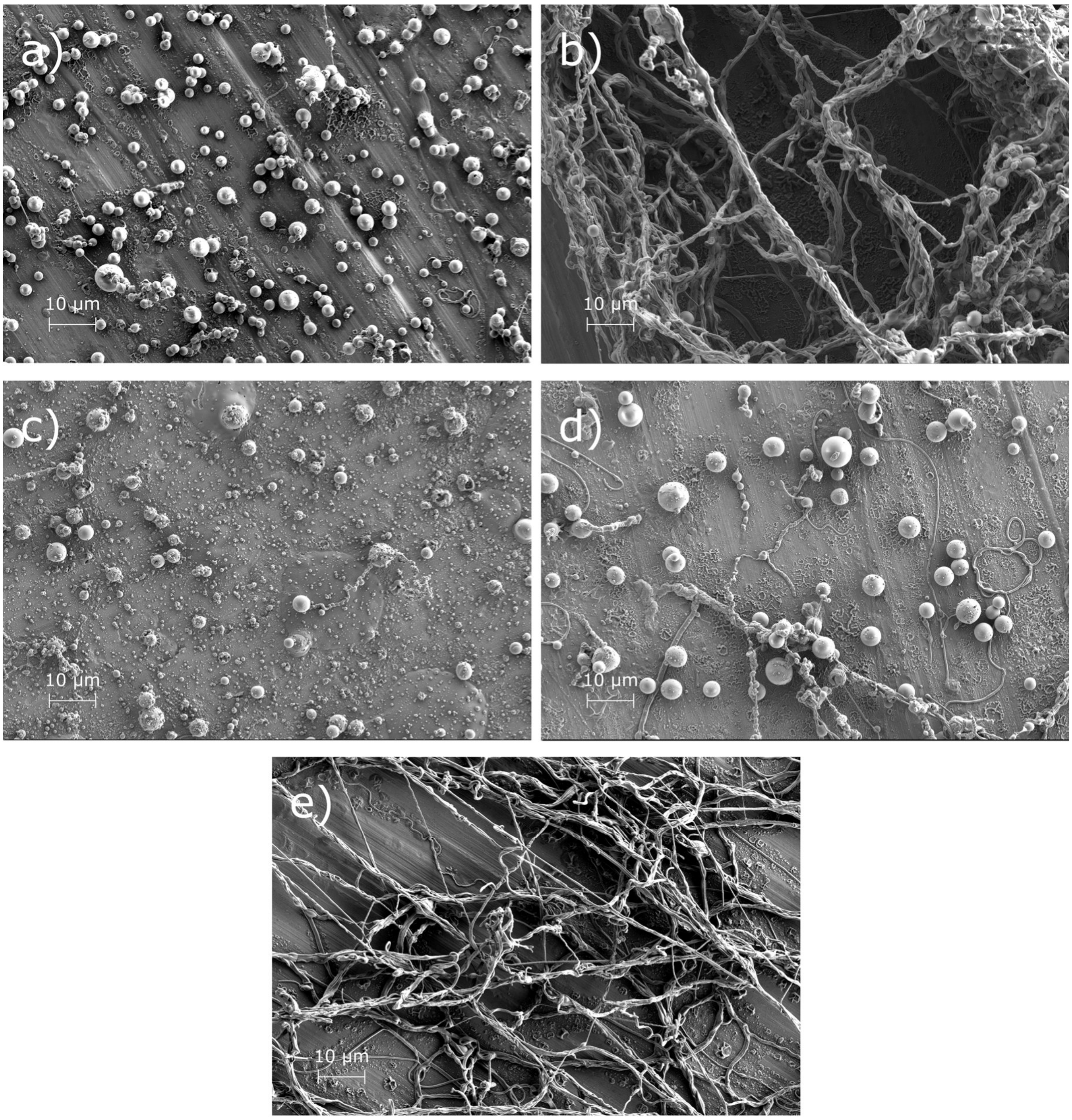

Figure 48 SEM pictures for spinning solution 2.2.3 a) 20 kV, 100 mm, b) 20 kV, 150 mm, c) 30 kV, 100 mm, d) 30 kV, 150 mm, e) 30 kV, 200 mm

Figure 47 shows the fiber diameter histograms for solution 2.2.2. already mentioned above, the fibers are much smaller, within a range of 0.33 to 0.45 µm, compared to the fibers gained from solution 1.2.2. This may be due to the greatly reduced ratio of PEO to PFSA in comparison to 1.2.2. Some thicker fibers can be found, but similar to 1.2.2, these are assumed to be fused smaller fibers. The fiber homogeneity can also be seen from the histograms, since the standard deviation of the distributions are small compared with the mean fiber diameter. An exception is posed by Figure 47 c) mainly due to an increased tendency to form more and larger fused fibers.

Solution 2.2.3

Figure 48 depicts the spinning experiment results for spinning solution 2.2.3. Despite showing a Taylor cone as well as a spinning jet, fibers only are generated for small electrostatic field strengths (1.33 to 1.5 kV/cm). For field strengths higher, the fibers may be disintegrated into droplets, leading to electrospraying or something similar.

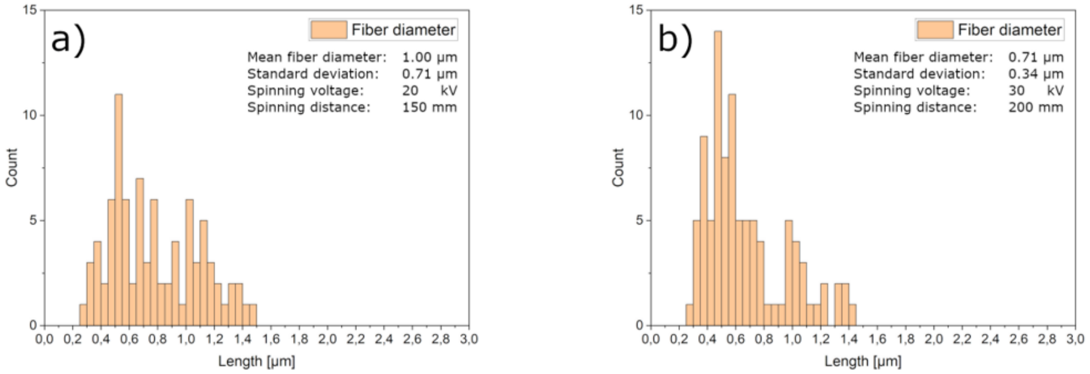

Figure 49 Histograms for measured fiber diameters for spinning solution 2.2.3

For field strengths around 2 kV/cm some remaining fibers can be found (see Figure 48 d)). The fibers generated from this solution show a strong tendency to form large agglomerates as well as fused fibers. At first glance it may seem that many of these fibers are beaded, but on closer examination it can be seen, that the fibers actually embed or twine around smaller droplets (also see appendix).

Figure 49 shows the histograms for the fiber generating parameter sets of solution 2.2.3. As already mentioned only parameters with an electric field strength between 1.33 and 1.5 kV/cm are able to form fibers in a continuous way. Fibers generated at an electric field strength of 1.33 kV/cm (see Figure 48 b) and Figure 49 a)) show an increased tendency to form fused fibers, resulting in a much broader diameter distribution and a higher mean fiber diameter. At higher electric field strengths (1.5 kV/cm) fibers tend to form less fused fibers and generally shift to smaller fiber diameters.

4.3.2 Long-term spinning experiments

Long term electrospinning reveals a tremendous problem for the application of these compositions as electrospun electrolytes. After some time, usually between 5 and 10 minutes, the fibers are not deposited onto the drum collector anymore. Reducing the rotational speed of the collector or stopping the rotation completely does not change the situation. The same effect is also seen for using a flat plate collector. A possible explanation for this phenomenon is an electrostatic repulsion of the already accumulated fibers on the collector. Measures to improve the grounding of the collector and its suspension showed no positive effect on the issue. Banitaba et al. have also experienced this effect for PEO fibers containing high amounts of lithium salts [17]. This leads to the conclusion, that the compositions described in Table 15 are not suitable for application as electrospun electrolytes. Additional experiments varying the salt concentration must be conducted. First proof-of-concept experiments using formulations without any lithium salts have formed very thick and agglomerating fibers. These fibers showed a tendency to stick to the emitter rather than lay down on the collector. Long spinning times were not possible, since the fibers grew to be an electrically low conductive bridge between the emitter and the collector, resulting in relatively high currents (out of the measuring scale of the set-up). Additionally, these fibers showed burn marks resulting from these relatively high currents and posed a fire hazard.

In the frame of this thesis no search or adjustments regarding the isoelectric point of any of the solutions was conducted. This may be a base for further experiments regarding PFSA-based spinning solutions.

4.4 Conclusions

PFSA-based electrolyte candidates have been investigated in regards of processability using electrospinning, ionic conductivities, and transference numbers. Solution-casted electrolyte membranes showed ionic conductivities in the range from 4.66×10^{-10} to 1.12×10^{-7} S/cm at room temperature. The transference number calculated for these samples ranges from 6.23×10^{-13} to 1.33×10^{-9}, far below values known for PEO at room temperature. Impedance measurements of samples undergoing an insufficient drying procedure indicate a much better electrochemical performance. This leads to the conclusion, that PFSA-based electrolytes may be a candidate for new functionalized gel polymer electrolytes.

In regard to the electrospinning processability, the tested solutions proved to form fibers for different spinning parameter sets. The fibers showed different morphologies, e.g., beaded and agglomerated fibers. Fiber thicknesses varied from 0.2 up to 1.4 µm. Fiber thickness depends thereby mainly on the weight concentration of the polymers, the voltage, and the spinning distance. Thinner fibers are formed for more diluted solutions at high voltages and great spinning distances. Fibers are also only formed for solutions in a water/ethanol mixed solvent.

An electrochemical investigation of electrospun PFSA-based electrolyte membranes was not possible since the fibers retained a large amount of charge due to the high lithium salt concentration during the electrospinning process. This led to fibers being repelled and unable to form a membrane of sufficient thickness for impedance measurement and full-cell characterization. Additional work in refining the electrolyte solution candidates in regard to lithium salt concentration and eventually the use of plasticizers has to be undertaken.

5. Summary and Conclusions

The use of electrospinning to manufacture improved polymeric electrolytes and their application in full cells was within the scope of this thesis. Two electrolyte systems have been investigated: Polyethylene oxide and Polyfluoride sulfonic acid.

Impedance measurements for PEO-based cells show an increase in ionic conductivities after cycling experiments with small currents. Cell conditioning leads to significant differences regarding the ionic conductivity as well as the cycle numbers needed to fulfill the conditioning criteria. It is concluded that the increase in ionic conductivity is dependent on the cycle numbers run at small currents. This is only observed for cells using an electrospun electrolyte.

An increasing capacity is found during cycling tests conducted at small cycling currents for all measured cells, including solution-casted electrolyte cells. No additional peaks besides the NMC-intercalation peak can be found in dQ/dV-data. The coulombic efficiency is also close to unity for all these cycling tests, therefore additional electrochemical reactions are unlikely to be the source of this phenomenon.

XRD data of post-mortem cells show no significant change regarding the crystallinity of the cathode. A possible explanation for this increase in conductivity may be an expansion of the electrodes, changing the porosity of the cathode, thereby reducing migration pathway lengths, rendering more parts of the electrode accessible.

More research is needed to fully understand the effects described in this thesis, especially direct measurement methods for these phenomena must be implemented.

PFSA-based electrolytes have been tested in regard to ionic conductivities as well as the ability to for fibers. Intensive work was directed to the development of a suitable formulation. For dry PFSA-solution-casted electrolytes, the highest reported ionic conductivity was in the range of 10^{-7} S/cm at room temperature, far below the highest ionic conductivity of PEO-electrolytes used in this study; for non-sufficient dried PFSA-electrolytes much higher ionic conductivities have been found; these can be used as a potential gel-electrolyte candidate. The ability to form fibers was also tested. While several proposed formulations were able to form fibers, all of them were unable to form fiber mats of sufficient thickness. The reason on this phenomenon was the high lithium salt concentration, used in all PFSA-based solutions, which led to an electrostatic charge at the collector, causing a counter electric field repelling additional fibers from the collector surface.

6. Suggestions for future work on electrospinning

In the following a short outlook on future research aspects based on the methods and results gained during this thesis will be presented. This also includes pre-tests conducted during this thesis which were later not part of it since the focus was more on all-solid-state systems.

6.1 Lamination of separators and electrodes using electrospinning

Lamination of separators and electrodes has some interesting advantages for the production of liquid-electrolyte based lithium ion batteries [125–128], e.g. an improvement in production due as well as an improvement of the electrochemical performance due to better electrode-separator interfaces [125, 126]. Unfortunately, many commercially available separators are not able to be laminated. Therefore, it is intriguing to modify separator surfaces to enable lamination, e.g., by electrospinning. First pre-tests have been conducted by the author using PVDF and a commercially available ceramic separator [42]. This topic was later deferred in favor of focusing on all-solid-state batteries using an electrospun polymer electrolyte. Nevertheless, this path still poses opportunities for research and improvements:

- The parameters used in lamination are crucial to the performance of the later battery. For example, if the lamination temperature is too high, damage can be done to the separator resulting in bad performance or even a complete shut-down of the cell. This leads to a requirement profile for the used polymer, including the melting temperature, the electrochemical stability, the solubility and swelling behavior in the desired electrolyte.
- One crucial question is the number of fibers on the separator. It is easily understood that a certain number of fibers is needed to ensure lamination. But in regard of electrochemical performance the question whether as little area as possible should be covered by fibers or a higher number of fibers for a nearly completely covered separator surface has to be investigated carefully.

6.2 Future research aspects regarding ASSBs

In this thesis ASSBs with lithium metal anode and electrospun electrolytes have been in the focus. Based on the methods and results of this thesis, several ideas for future research will be presented here.

6.2.1 Electrodes: Cathode

The cathode used in this thesis was described already in 3. Nevertheless, the electrodes pose a great potential for improvement and research.

The formulation used for this cathode can be further tuned. An example is the combination of binder polymers in the cathode. The proportion of PEO and PVDF can be further optimized in regard to the ionic conduction and the adhesion to the current collector. Another possible idea is the use of special crafted or modified polymers.

Another aspect on the cathode is the structure of the electrode, especially the contact and the contacting of the ion conducting polymer species with the active material is of interest. In addition, the impact of porosity on the electrode performance is of interest. In this regard, processing of the electrodes after or during the casting of the electrode on the current collector can be investigated, especially to gain knowledge on the relationship between the processing, structure, and electrochemical performance of the electrodes. In addition, new approaches in manufacturing electrodes, e.g., dry-coating of electrodes, should be considered for research and production of cathodes for ASSBs.

6.2.2 Electrodes: Anodes

The anode used in this thesis was simply metallic lithium. For later production of ASSBs with metallic lithium anodes, further research must be conducted, especially to ease the handling and safety problems of lithium. Fundamental research and interface engineering are needed and have been conducted recently [10, 65, 66, 68, 83, 129, 130].

Another very interesting approach are ASSBs are cell designs without an anode [131]. Problems during production connected to the use of lithium metal as an anode are eliminated in this approach intrinsically.

6.2.3 Interfaces between electrodes and electrolyte

Interfaces between the electrodes and the electrolytes play a crucial role. The present thesis focuses on the characterization of electrospun electrolytes in lithium-metal batteries. Therefore, a cathode has been manufactured and used in the experiments throughout, but deep insights into the interfaces have not been conducted. Based on the system used in in this thesis several interfaces must be considered:

- Interfaces within the composite cathode: The interfaces in the used cathode are especially of interest. The cathode formulation was meant to have sufficient PEO/LiTFSI to sheath the NMC_{111} particles fully and have as less porosity as possible. From the electrochemical data gained, e.g., cycling tests, it can be seen that the cathode was not fully activated over the course of the experiments, leading to an increase of discharge capacity. Possible explanations can be the actual porosity of the cathode, the interface between the PEO and the NMC_{111} and the crystallinity of the PEO. The porosity of the cathode can lead to an increase of diffusion pathways within the electrode and therefore render it less active. Cycling the cell may lead to a volume change of the NMC_{111} and thus lead to a small decrease of the electrode porosity. The behavior of the interface between the NMC_{111} and the PEO must also be considered and investigate, e.g., in regard of “the wetting” of the NMC_{111} by the PEO. An insufficient wetting leads to a more problematic ion diffusion into or from the NMC_{111}. In addition, the formation of a solid electrolyte interphase has to be considered and investigated.
- Interface between the cathode and the electrolyte: The interface between the cathode and the electrolyte is quite an interesting field since here the lithium ions change from discrete conduction paths (fibers) to a continuum (electrode). To avoid problems with possible dendrite formation due to the discrete conduction of the fibers, an interlayer has been introduced. The necessity and the characteristics of this interlayer may be of research interest in future works.
- Interface between the anode and the electrolyte: At this interface mainly two aspects are of interest. First, the formation of a SEI should be investigated for classical solution casting and electrospinning since the effective area of the electrospun electrolyte is smaller. Second, the formation of dendrites when cycling at high current densities. It is known from literature that in liquid electrolyte based systems non-woven or foam-like structures can deflect and homogenize the growth of dendrites [132–134]. It cannot be ruled out, that a similar effect can be seen using electrospun electrolytes.

6.2.4 Electrolyte

During this thesis a platform for further research on all-solid-state electrolytes was developed and tested using two different polymer electrolytes. Further research can be done on many more different electrolytes.

6.2.5 Charging procedure

A crucial challenge due to the incomplete active electrode was to find a suitable charging procedure. The charging procedure was mainly based on the experiences made with liquid electrolyte cells. This must not mean it is the best procedure for all-solid-state lithium-ion batteries. One experience from the electrochemical testing during this thesis was an increase in the discharge capacity during the C-rate test. In this case a discharge C-rate test was performed followed by a charge C-rate test. One observation made was a strong increase in the discharge capacity at 0.2 C after the discharge C-rate. This leads to the idea that relatively strong currents or combinations of different discharge and charge currents can speed-up the process of electrode activation. The underlying mechanism is not understood and requires in depth investigation.

6.2.6 Cell housing

The cells build during this thesis have been successfully demonstrated using T- and Coin-type cell housing. For production at scales higher than laboratory use, different cell housings must be tested for this kind of cells.

Enabling the use of pouch cells is a step towards industrial production; On one hand, Pouch cells are already used for many different applications (e.g., mobile phones, smart devices) on the other hand, mastering the use of Pouch cells can pave the way towards more complicated and diverse cell housings, e.g., cylindrical cell types.

First attempts for a proof of concept using electrospun electrolytes in Pouches have been conducted during this thesis. The cell system used in this thesis has been proven feasible for the use in Pouch cell, although some optimization must be conducted. This refers especially to the used current collector, in this case copper expanded metal.

The anode in these cells was metallic lithium, rolled in the expanded metal. This ensures that the lithium metal does not segregate from the current collector during cycling of the cell. Unfortunately, expanded metal can form sharp edges when punched in form of an anode, which poses a safety issue either by piercing through the Pouch or by short-circuiting the cell. Therefore, different current collectors must be tested and possibly optimized for the use in Pouch cells.

There are still some difficulties to be solved for the use of electrospun electrolytes in pouch cells:

- Cell pressure: The pressure on the cell must be chosen carefully. Freitag et al. stated that too much pressure on the electrolyte can lead to a reduction of performance [18]. In addition, the use of expanded metal can lead to short circuits when too much pressure is applied. On the other side a certain pressure is needed to ensure the functionality of the cells.
- The sealing temperature of the cell housing has also to be optimized. First experiments using electrospun electrolytes in pouch cells showed molten fibers in the vicinity of the sealing.
- Expanded metal can lead to another problem: in first experiments the anode was chosen to be geometrically smaller than the cathode, in agreement with the cell design used in coin cells. Unfortunately, this leads to a small portion of the expanded metal current collector to overlap with the electrospun electrolyte and the cathode, posing a possible short-circuiting risk within the cell. A lab scale solution can be the use of electrochemically inert adhesive tape, which, obviously, is not solution for larger production.

List of Figures

List of Abbreviations

A

ASSB	All-solid-state Battery, All-solid-state Battery

C

C	Capacitance
CC	Constant current
CF_4	*Carbon tetrafluoride*
CH_4	Methane
Co	Cobalt
CO_2	Carbon dioxide
CPE	Constant phase element
CV	Constant voltage

E

EIS	Electrochemical impedance spectroscopy
EV	Electric vehicle

I

IPCC	Intergovernmental Panel on Climate Change

L

L	Inductance
LCO	Lithium cobalt oxide, Lithium cobalt oxide
Li_3N	Lithium nitride
LIB	Lithium-Ion Battery
$LiCoO_2$	Lithium cobalt oxide
LiFeO	Lithium iron oxide
$LiFePO_4$	Lithium iron phosphate
$LiNiO_2$	Lithium nickel oxide
$LiNi_xCo_yAl_{1-x-y}O_2$	Lithium nickel cobalt aluminium oxide
$LiNi_xMn_yCo_{1-x-y}O_2$	Lithium nickel manganese cobalt oxide
LiPON	Lithium phosphorus oxynitride
LNO	Lithium nickel oxide

M

Mn	Manganese

N

NCA	Lithium nickel cobalt aluminium oxide
Ni	Nickel
NMC	Lithium-nickel-manganese-cobalt oxide
NMP	N-methyl-pyrrolidone

O

OCV	Open circuit voltage, Open circuit voltage
OM	Optical microscopy

P

PEO	Polyethylene oxide
PFSA	Perfluorosulfonic acid, Perfluorosulfonic acid
PHEV	Plug-in hybrid electric vehicle
PVDF	Polyvinylidene fluoride

R

R	Ohmic resistance

S

SEI	Solid electrolyte interface
SEM	Scanning electron microscopy
Si	Silicium
SOC	State-of-charge

References

[1] R. K. Pachauri *et al.,* “Climate Change 2014: Synthesis Report,” Contribution of Working Groups I, II and III to the Fifth Assessment Report of the Intergovernmental Panel on Climate Change, Geneva, 2014.

[2] Bundesministerium für Wirtschaft und Energie, *Abkommen von Paris.* [Online]. Available: https://www.bmwi.de/Redaktion/DE/Artikel/Industrie/klimaschutz-abkommen-von-paris.html (accessed: Aug. 9 2021).

[3] P. Sterchele *et al.,* “Wege zu einem klimaneutralen Energiesystem: Die deutsche Energiewende im Kontext gesellschaftlicher Verhaltensweisen,” Fraunhofer-Institut für Solare Energiesysteme ISE, Freiburg, Feb. 2020.

[4] BMU, *Klimaschutzprogramm 2030 der Bundesregierung zur Umsetzung des Klimaschutzplans 2050.* [Online]. Available: https://www.bundesregierung.de/resource/blob/975226/1679914/e01d6bd855f09bf05cf7498e06d0a3ff/2019-10-09-klima-massnahmen-data.pdf?download=1 (accessed: Nov. 7 2020).

[5] P. Hertzke, N. Müller, P. Schaufuss, S. Schenk, and T. Wu, “Expanding electric-vehicle adoption despite early growing pains,” *McKinsey & Company*, 26 Aug., 2019. https://www.mckinsey.com/industries/automotive-and-assembly/our-insights/expanding-electric-vehicle-adoption-despite-early-growing-pains (accessed: Aug. 9 2021).

[6] A. Jossen and W. Weydanz, *Moderne Akkumulatoren richtig einsetzen,* 2nd ed., 2019.

[7] G. Homann, L. Stolz, J. Nair, I. C. Laskovic, M. Winter, and J. Kasnatscheew, “Poly(Ethylene Oxide)-based Electrolyte for Solid-State-Lithium-Batteries with High Voltage Positive Electrodes: Evaluating the Role of Electrolyte Oxidation in Rapid Cell Failure,” *Scientific reports*, vol. 10, no. 1, p. 4390, 2020, doi: 10.1038/s41598-020-61373-9.

[8] M. Weiss *et al.,* “From Liquid- to Solid-State Batteries: Ion Transfer Kinetics of Heteroionic Interfaces,” *Electrochem. Energ. Rev.*, vol. 3, no. 2, pp. 221–238, 2020, doi: 10.1007/s41918-020-00062-7.

[9] T. Zhang *et al.,* “Designing composite solid-state electrolytes for high performance lithium ion or lithium metal batteries,” *Chem. Sci.*, vol. 11, no. 33, pp. 8686–8707, 2020, doi: 10.1039/D0SC03121F.

[10] T. Krauskopf, F. H. Richter, W. G. Zeier, and J. Janek, “Physicochemical Concepts of the Lithium Metal Anode in Solid-State Batteries,” *Chemical reviews*, vol. 120, no. 15, pp. 7745–7794, 2020, doi: 10.1021/acs.chemrev.0c00431.

[11] C. Yada and C. Brasse, “Bessere Batterien mit festem statt flüssigem Elektrolyt,” *ATZelektronik*, 2014, pp. 20–25, 2014. https://www.springerprofessional.de/bessere-batterien-mit-festem-statt-fluessigem-elektrolyt/6417058 (accessed: Nov. 7 2020).

[12] X. Ji *et al.,* “Solid-State Electrolyte Design for Lithium Dendrite Suppression,” *Advanced materials (Deerfield Beach, Fla.)*, e2002741, 2020, doi: 10.1002/adma.202002741.

[13] B. V. Lotsch and J. Maier, “Relevance of solid electrolytes for lithium-based batteries: A realistic view,” *J Electroceram*, vol. 38, 2-4, pp. 128–141, 2017, doi: 10.1007/s10832-017-0091-0.

[14] S. Xia, X. Wu, Z. Zhang, Y. Cui, and W. Liu, “Practical Challenges and Future Perspectives of All-Solid-State Lithium-Metal Batteries,” *Chem*, vol. 5, no. 4, pp. 753–785, 2019, doi: 10.1016/j.chempr.2018.11.013.

[15] S. N. Banitaba, D. Semnani, B. Rezaei, and A. A. Ensafi, “Evaluating the electrochemical properties of PEO-based nanofibrous electrolytes incorporated with TiO 2 nanofiller applicable in lithium-ion batteries,” *Polym Adv Technol*, vol. 30, no. 5, pp. 1234–1242, 2019, doi: 10.1002/pat.4556.

[16] S. N. Banitaba, D. Semnani, E. Heydari-Soureshjani, B. Rezaei, and A. A. Ensafi, “Nanofibrous poly(ethylene oxide)-based structures incorporated with multi-walled carbon nanotube and graphene oxide as all-solid-state electrolytes for lithium ion batteries,” *Polym. Int.*, vol. 68, no. 10, pp. 1787–1794, 2019, doi: 10.1002/pi.5889.

[17] S. N. Banitaba *et al.,* “Electrospun PEO nanofibrous membrane enable by LiCl, LiClO4, and LiTFSI salts: a versatile solvent-free electrolyte for lithium-ion battery application,” *Ionics*, vol. 26, no. 7, pp. 3249–3260, 2020, doi: 10.1007/s11581-019-03414-6.

[18] K. M. Freitag, H. Kirchhain, L. van Wüllen, and T. Nilges, “Enhancement of Li Ion Conductivity by Electrospun Polymer Fibers and Direct Fabrication of Solvent-Free Separator Membranes for Li Ion Batteries,” *Inorganic chemistry*, vol. 56, no. 4, pp. 2100–2107, 2017, doi: 10.1021/acs.inorgchem.6b02781.

[19] K. Takada, “Solid electrolytes and solid-state batteries,” in Freiberg, Germany, 2016, p. 20008.

[20] Q. Zhao, S. Stalin, C.-Z. Zhao, and L. A. Archer, “Designing solid-state electrolytes for safe, energy-dense batteries,” *Nature Reviews Materials*, vol. 5, no. 3, pp. 229–252, 2020, doi: 10.1038/s41578-019-0165-5.

[21] W. Liu *et al.,* “Ionic conductivity enhancement of polymer electrolytes with ceramic nanowire fillers,” *Nano Letters*, vol. 15, no. 4, pp. 2740–2745, 2015, doi: 10.1021/acs.nanolett.5b00600.

[22] D.-Z. Zhang, Y.-y. Ren, Y. Hu, L. Li, and F. Yan, “Ionic Liquid/Poly(ionic liquid)-based Semi-solid State Electrolytes for Lithium-ion Batteries,” *Chin J Polym Sci*, vol. 38, no. 5, pp. 506–513, 2020, doi: 10.1007/s10118-020-2390-1.

[23] M. Forsyth, L. Porcarelli, X. Wang, N. Goujon, and D. Mecerreyes, “Innovative Electrolytes Based on Ionic Liquids and Polymers for Next-Generation Solid-State Batteries,” *Accounts of chemical research*, vol. 52, no. 3, pp. 686–694, 2019, doi: 10.1021/acs.accounts.8b00566.

[24] K. M. Freitag, P. Walke, T. Nilges, H. Kirchhain, R. J. Spranger, and L. van Wüllen, “Electrospun-sodiumtetrafluoroborate-polyethylene oxide membranes for solvent-free sodium ion transport in solid state sodium ion batteries,” *Journal of Power Sources*, vol. 378, pp. 610–617, 2018, doi: 10.1016/j.jpowsour.2017.12.083.

[25] P. Walke, K. M. Freitag, H. Kirchhain, M. Kaiser, L. van Wüllen, and T. Nilges, “Electrospun Li(TFSI)@Polyethylene Oxide Membranes as Solid Electrolytes,” *Z. Anorg. Allg. Chem.*, vol. 644, no. 24, pp. 1863–1874, 2018, doi: 10.1002/zaac.201800370.

[26] K. Kerman, A. Luntz, V. Viswanathan, Y.-M. Chiang, and Z. Chen, “Review—Practical Challenges Hindering the Development of Solid State Li Ion Batteries,” *J. Electrochem. Soc.*, vol. 164, no. 7, A1731-A1744, 2017, doi: 10.1149/2.1571707jes.

[27] A. Greiner, J. Wendorff, and M. Burgard, *Electrospinning: A Practical Guide to Nanofibers.* [Online]. Available: http://gbv.eblib.com/patron/FullRecord.aspx?p=4459584

[28] N. Tucker, J. J. Stanger, M. P. Staiger, H. Razzaq, and K. Hofman, “The History of the Science and Technology of Electrospinning from 1600 to 1995,” *Journal of Engineered Fibers and Fabrics*, vol. 7, 2_suppl, 155892501200702, 2012, doi: 10.1177/155892501200702S10.

[29] J.-W. Jung, C.-L. Lee, S. Yu, and I.-D. Kim, “Electrospun nanofibers as a platform for advanced secondary batteries: a comprehensive review,” *J. Mater. Chem. A*, vol. 4, no. 3, pp. 703–750, 2016, doi: 10.1039/c5ta06844d.

[30] T. Ludwig, C. Bohr, A. Queraltó, R. Frohnhoven, T. Fischer, and S. Mathur, “Chapter One - Inorganic Nanofibers by Electrospinning Techniques and Their Application in Energy Conversion and Storage Systems,” in *Semiconductors and Semimetals : Nanowires for Energy Applications*, S. Mokkapati and C. Jagadish, Eds.: Elsevier, 2018, pp. 1–70. [Online]. Available: https://www.sciencedirect.com/science/article/pii/S0080878418300085

[31] M. Baghali, W. A. D. M. Jayathilaka, and S. Ramakrishna, “The Role of Electrospun Nanomaterials in the Future of Energy and Environment,” *Materials (Basel,*

Switzerland), vol. 14, no. 3, 2021, doi: 10.3390/ma14030558.

[32] G. Massaglia and M. Quaglio, “Semiconducting Electrospun Nanofibers for Energy Conversion,” in *Semiconductors - Growth and Characterization*, R. Inguanta and C. Sunseri, Eds.: InTech, 2018.

[33] Z. Dong, S. J. Kennedy, and Y. Wu, “Electrospinning materials for energy-related applications and devices,” *Journal of Power Sources*, vol. 196, no. 11, pp. 4886–4904, 2011, doi: 10.1016/j.jpowsour.2011.01.090.

[34] Q. Liu, J. Zhu, L. Zhang, and Y. Qiu, “Recent advances in energy materials by electrospinning,” *Renewable and Sustainable Energy Reviews*, vol. 81, pp. 1825–1858, 2018, doi: 10.1016/j.rser.2017.05.281.

[35] D. J. Powers, *Electrospun Nanofiber Composite Membranes for Hydrogen/Air Fuel Cells*, 2019. [Online]. Available: https://ir.vanderbilt.edu/handle/1803/12023

[36] C. Kim, Y.-O. Choi, W.-J. Lee, and K.-S. Yang, “Supercapacitor performances of activated carbon fiber webs prepared by electrospinning of PMDA-ODA poly(amic acid) solutions,” *Electrochimica Acta*, vol. 50, 2-3, pp. 883–887, 2004, doi: 10.1016/j.electacta.2004.02.072.

[37] V. Aravindan, J. Sundaramurthy, P. Suresh Kumar, Y.-S. Lee, S. Ramakrishna, and S. Madhavi, “Electrospun nanofibers: a prospective electro-active material for constructing high performance Li-ion batteries,” *Chemical Communications*, vol. 51, no. 12, pp. 2225–2234, 2015, doi: 10.1039/c4cc07824a.

[38] H.-l. Chen and X.-n. Jiao, “Preparation and characterization of Polyvinylidene fluoride/Octaphenyl-Polyhedral oligomeric silsesquioxane hybrid Lithium-ion battery separators by electrospinning,” *Solid State Ionics*, vol. 310, pp. 134–142, 2017, doi: 10.1016/j.ssi.2017.08.017.

[39] C. Kim *et al.,* “Fabrication of Electrospinning-Derived Carbon Nanofiber Webs for the Anode Material of Lithium-Ion Secondary Batteries,” *Advanced Functional Materials*, vol. 16, no. 18, pp. 2393–2397, 2006, doi: 10.1002/adfm.200500911.

[40] Y. Li, Q. Li, and Z. Tan, “A review of electrospun nanofiber-based separators for rechargeable lithium-ion batteries,” *Journal of Power Sources*, vol. 443, p. 227262, 2019, doi: 10.1016/j.jpowsour.2019.227262.

[41] Z. Liu *et al.,* “A Core@sheath Nanofibrous Separator for Lithium Ion Batteries Obtained by Coaxial Electrospinning,” *Macromol. Mater. Eng.*, vol. 298, no. 7, pp. 806–813, 2013, doi: 10.1002/mame.201200158.

[42] B. C. Springer, M. Frankenberger, and K.-H. Pettinger, “Lamination of Separators to Electrodes using Electrospinning,” *PloS one*, vol. 15, no. 1, e0227903, 2020, doi: 10.1371/journal.pone.0227903.

[43] X. Zhang, L. Ji, O. Toprakci, Y. Liang, and M. Alcoutlabi, “Electrospun Nanofiber-Based Anodes, Cathodes, and Separators for Advanced Lithium-Ion Batteries,” *Polymer Reviews*, vol. 51, no. 3, pp. 239–264, 2011, doi: 10.1080/15583724.2011.593390.

[44] S. N. Banitaba, D. Semnani, E. Heydari-Soureshjani, B. Rezaei, and A. A. Ensafi, “Electrospun core-shell nanofibers based on polyethylene oxide reinforced by multiwalled carbon nanotube and silicon dioxide nanofillers: A novel and effective solvent-free electrolyte for lithium ion batteries,” *Int J Energy Res*, vol. 44, no. 8, pp. 7000–7014, 2020, doi: 10.1002/er.5475.

[45] E. Kostakova, L. Meszaros, and J. Gregr, “Composite nanofibers produced by modified needleless electrospinning,” *Materials Letters*, vol. 63, no. 28, pp. 2419–2422, 2009, doi: 10.1016/j.matlet.2009.08.014.

[46] B. Lu *et al.,* “Superhigh-throughput needleless electrospinning using a rotary cone as spinneret,” *Small*, vol. 6, no. 15, pp. 1612–1616, 2010, doi: 10.1002/smll.201000454.

[47] H. Niu, T. Lin, and X. Wang, “Needleless electrospinning. I. A comparison of cylinder and disk nozzles,” *Journal of Applied Polymer Science*, vol. 114, no. 6, pp. 3524–3530, 2009, doi: 10.1002/app.30891.

[48] T. Rosenthal, J. M. Weller, and C. K. Chan, “Needleless Electrospinning for High Throughput Production of Li 7 La 3 Zr 2 O 12 Solid Electrolyte Nanofibers,” *Ind. Eng. Chem. Res.*, vol. 58, no. 37, pp. 17399–17405, 2019, doi: 10.1021/acs.iecr.9b03376.

[49] N. M. Thoppey, J. R. Bochinski, L. I. Clarke, and R. E. Gorga, “Unconfined fluid electrospun into high quality nanofibers from a plate edge,” *Polymer*, vol. 51, no. 21, pp. 4928–4936, 2010, doi: 10.1016/j.polymer.2010.07.046.

[50] N. M. Thoppey, J. R. Bochinski, L. I. Clarke, and R. E. Gorga, “Edge electrospinning for high throughput production of quality nanofibers,” *Nanotechnology*, vol. 22, no. 34, p. 345301, 2011, doi: 10.1088/0957-4484/22/34/345301.

[51] G. Prahasti, A. Zulfi, and M. M. Munir, “Needleless electrospinning system with wire spinneret: an alternative way to control morphology, size, and productivity of nanofibers,” *Nano Ex.*, vol. 1, no. 1, p. 10046, 2020, doi: 10.1088/2632-959X/ab976a.

[52] T. Li, X.-Z. Yuan, L. Zhang, D. Song, K. Shi, and C. Bock, “Degradation Mechanisms and Mitigation Strategies of Nickel-Rich NMC-Based Lithium-Ion Batteries,” *Electrochem. Energ. Rev.*, vol. 3, no. 1, pp. 43–80, 2020, doi: 10.1007/s41918-019-00053-3.

[53] C. Julien, A. Mauger, K. Zaghib, and H. Groult, “Comparative Issues of Cathode Materials for Li-Ion Batteries,” *Inorganics*, vol. 2, no. 1, pp. 132–154, 2014, doi: 10.3390/inorganics2010132.

[54] N. Tsurukawa, S. Prakash, and A. Manhart, “Social impacts of artisanal cobalt mining in Katanga, Democratic Republic of Congo,” Öko-Institute e.V. Institute for Applied Ecology, Freiburg, Nov. 2011.

[55] R. Amin and Y.-M. Chiang, “Characterization of Electronic and Ionic Transport in Li 1-x Ni 0.33 Mn 0.33 Co 0.33 O 2 (NMC 333) and Li 1-x Ni 0.50 Mn 0.20 Co 0.30 O 2 (NMC 523) as a Function of Li Content,” *J. Electrochem. Soc.*, vol. 163, no. 8, A1512-A1517, 2016, doi: 10.1149/2.0131608jes.

[56] R. Amin, D. B. Ravnsbæk, and Y.-M. Chiang, “Characterization of Electronic and Ionic Transport in Li 1-x Ni 0.8 Co 0.15 Al 0.05 O 2 (NCA),” *J. Electrochem. Soc.*, vol. 162, no. 7, A1163-A1169, 2015, doi: 10.1149/2.0171507jes.

[57] C. Wang and J. Hong, “Ionic/Electronic Conducting Characteristics of LiFePO[sub 4] Cathode Materials,” *Electrochem. Solid-State Lett.*, vol. 10, no. 3, A65, 2007, doi: 10.1149/1.2409768.

[58] B. W. Byles, N. K. R. Palapati, A. Subramanian, and E. Pomerantseva, “The role of electronic and ionic conductivities in the rate performance of tunnel structured manganese oxides in Li-ion batteries,” *APL Materials*, vol. 4, no. 4, p. 46108, 2016, doi: 10.1063/1.4948272.

[59] M. Mao *et al.,* “Electronic Conductive Inorganic Cathodes Promising High-Energy Organic Batteries,” *Advanced materials (Deerfield Beach, Fla.)*, vol. 33, no. 8, e2005781, 2021, doi: 10.1002/adma.202005781.

[60] C. M. Julien, A. Mauger, and K. Zaghib, “Surface effects on electrochemical properties of nano-sized LiFePO4,” *J. Mater. Chem.*, vol. 21, no. 27, p. 9955, 2011, doi: 10.1039/C0JM04190D.

[61] T.V.S.L. Satyavani, B. Ramya Kiran, V. Rajesh Kumar, A. Srinivas Kumar, and S. V. Naidu, “Effect of particle size on dc conductivity, activation energy and diffusion coefficient of lithium iron phosphate in Li-ion cells,” *Engineering Science and Technology, an International Journal*, vol. 19, no. 1, pp. 40–44, 2016, doi: 10.1016/j.jestch.2015.05.011.

[62] A. Yamada, Y. Kudo, and K.-Y. Liu, “Phase Diagram of Li[sub x](Mn[sub y]Fe[sub 1−y])PO[sub 4] (0≤x, y≤1),” *J. Electrochem. Soc.*, vol. 148, no. 10, A1153, 2001, doi: 10.1149/1.1401083.

[63] E. Vilchevskaya and I. Sevostianov, “Effect of pore shapes on the overall electrical conductivity of cathode material in Li-ion batteries,” *International Journal of Engineering Science*, vol. 146, p. 103187, 2020, doi: 10.1016/j.ijengsci.2019.103187.

[64] M. E. Spahr, D. Goers, A. Leone, S. Stallone, and E. Grivei, “Development of carbon conductive additives for advanced lithium ion batteries,” *Journal of Power Sources*,

vol. 196, no. 7, pp. 3404–3413, 2011, doi: 10.1016/j.jpowsour.2010.07.002.

[65] X.-B. Cheng, R. Zhang, C.-Z. Zhao, and Q. Zhang, “Toward Safe Lithium Metal Anode in Rechargeable Batteries: A Review,” *Chem. Rev.*, vol. 117, no. 15, pp. 10403–10473, 2017, doi: 10.1021/acs.chemrev.7b00115.

[66] F. Aguesse *et al.,* “Investigating the Dendritic Growth during Full Cell Cycling of Garnet Electrolyte in Direct Contact with Li Metal,” *ACS Applied Materials & Interfaces*, vol. 9, no. 4, pp. 3808–3816, 2017, doi: 10.1021/acsami.6b13925.

[67] Z. Ahmad and V. Viswanathan, “Stability of Electrodeposition at Solid-Solid Interfaces and Implications for Metal Anodes,” *Physical Review Letters*, vol. 119, no. 5, p. 56003, 2017, doi: 10.1103/PhysRevLett.119.056003.

[68] T. Bartsch *et al.,* “Gas Evolution in All-Solid-State Battery Cells,” *ACS Energy Letters*, vol. 3, no. 10, pp. 2539–2543, 2018, doi: 10.1021/acsenergylett.8b01457.

[69] T. Krauskopf, H. Hartmann, W. G. Zeier, and J. Janek, “Toward a Fundamental Understanding of the Lithium Metal Anode in Solid-State Batteries-An Electrochemo-Mechanical Study on the Garnet-Type Solid Electrolyte Li6.25Al0.25La3Zr2O12,” *ACS Applied Materials & Interfaces*, vol. 11, no. 15, pp. 14463–14477, 2019, doi: 10.1021/acsami.9b02537.

[70] C. Ma *et al.,* “Interfacial Stability of Li Metal-Solid Electrolyte Elucidated via in Situ Electron Microscopy,” *Nano Letters*, vol. 16, no. 11, pp. 7030–7036, 2016, doi: 10.1021/acs.nanolett.6b03223.

[71] M. Arakawa, S.-i. Tobishima, Y. Nemoto, M. Ichimura, and J.-i. Yamaki, “Lithium electrode cycleability and morphology dependence on current density,” *Journal of Power Sources*, vol. 43, 1-3, pp. 27–35, 1993, doi: 10.1016/0378-7753(93)80099-B.

[72] P.-H. Chien *et al.,* “Li Distribution Heterogeneity in Solid Electrolyte Li10GeP2S12 upon Electrochemical Cycling Probed by 7Li MRI,” *The Journal of Physical Chemistry Letters*, vol. 9, no. 8, pp. 1990–1998, 2018, doi: 10.1021/acs.jpclett.8b00240.

[73] D. S. Eastwood *et al.,* “Three-dimensional characterization of electrodeposited lithium microstructures using synchrotron X-ray phase contrast imaging,” *Chemical Communications*, vol. 51, no. 2, pp. 266–268, 2015, doi: 10.1039/C4CC03187C.

[74] L. Frenck, G. K. Sethi, J. A. Maslyn, and N. P. Balsara, “Factors That Control the Formation of Dendrites and Other Morphologies on Lithium Metal Anodes,” *Front. Energy Res.*, vol. 7, 2019, doi: 10.3389/fenrg.2019.00115.

[75] J. Kasemchainan *et al.,* “Critical stripping current leads to dendrite formation on plating in lithium anode solid electrolyte cells,” *Nature Materials*, vol. 18, no. 10, pp. 1105–1111, 2019, doi: 10.1038/s41563-019-0438-9.

[76] T. Krauskopf, B. Mogwitz, C. Rosenbach, W. G. Zeier, and J. Janek, “Diffusion

Limitation of Lithium Metal and Li–Mg Alloy Anodes on LLZO Type Solid Electrolytes as a Function of Temperature and Pressure,” *Adv. Energy Mater.*, vol. 9, no. 44, p. 1902568, 2019, doi: 10.1002/aenm.201902568.

[77] W. S. LePage *et al.,* “Lithium Mechanics: Roles of Strain Rate and Temperature and Implications for Lithium Metal Batteries,” *J. Electrochem. Soc.*, vol. 166, no. 2, A89-A97, 2019, doi: 10.1149/2.0221902jes.

[78] G. Li and C. W. Monroe, “Dendrite nucleation in lithium-conductive ceramics,” *Physical Chemistry Chemical Physics*, vol. 21, no. 36, pp. 20354–20359, 2019, doi: 10.1039/C9CP03884A.

[79] H. Liu *et al.,* “Controlling Dendrite Growth in Solid-State Electrolytes,” *ACS Energy Letters*, vol. 5, no. 3, pp. 833–843, 2020, doi: 10.1021/acsenergylett.9b02660.

[80] X. Wang *et al.,* “New Insights on the Structure of Electrochemically Deposited Lithium Metal and Its Solid Electrolyte Interphases via Cryogenic TEM,” *Nano Letters*, vol. 17, no. 12, pp. 7606–7612, 2017, doi: 10.1021/acs.nanolett.7b03606.

[81] S. Wenzel *et al.,* “Direct Observation of the Interfacial Instability of the Fast Ionic Conductor Li 10 GeP 2 S 12 at the Lithium Metal Anode,” *Chemistry of Materials*, vol. 28, no. 7, pp. 2400–2407, 2016, doi: 10.1021/acs.chemmater.6b00610.

[82] S. Wenzel, D. A. Weber, T. Leichtweiss, M. R. Busche, J. Sann, and J. Janek, “Interphase formation and degradation of charge transfer kinetics between a lithium metal anode and highly crystalline Li7P3S11 solid electrolyte,” *Solid State Ionics*, vol. 286, pp. 24–33, 2016, doi: 10.1016/j.ssi.2015.11.034.

[83] X.-Q. Zhang, X.-B. Cheng, and Q. Zhang, “Advances in Interfaces between Li Metal Anode and Electrolyte,” *Adv. Mater. Interfaces*, vol. 5, no. 2, p. 1701097, 2018, doi: 10.1002/admi.201701097.

[84] Y. Ren, Y. Shen, Y. Lin, and C.-W. Nan, “Microstructure Manipulation for Enhancing the Resistance of Garnet-Type Solid Electrolytes to "Short Circuit" by Li Metal Anodes,” *ACS Applied Materials & Interfaces*, vol. 11, no. 6, pp. 5928–5937, 2019, doi: 10.1021/acsami.8b17954.

[85] Z. Shen, W. Zhang, G. Zhu, Y. Huang, Q. Feng, and Y. Lu, “Design Principles of the Anode–Electrolyte Interface for All Solid-State Lithium Metal Batteries,” *Small Methods*, vol. 4, no. 1, p. 1900592, 2020, doi: 10.1002/smtd.201900592.

[86] C. Wang *et al.,* “Suppression of Lithium Dendrite Formation by Using LAGP-PEO (LiTFSI) Composite Solid Electrolyte and Lithium Metal Anode Modified by PEO (LiTFSI) in All-Solid-State Lithium Batteries,” *ACS Applied Materials & Interfaces*, vol. 9, no. 15, pp. 13694–13702, 2017, doi: 10.1021/acsami.7b00336.

[87] R. C. Agrawal and G. P. Pandey, “Solid polymer electrolytes: materials designing and

all-solid-state battery applications: an overview," *J. Phys. D: Appl. Phys.*, vol. 41, no. 22, p. 223001, 2008, doi: 10.1088/0022-3727/41/22/223001.

[88] Y. Jiang *et al.,* "Development of the PEO Based Solid Polymer Electrolytes for All-Solid State Lithium Ion Batteries," *Polymers*, vol. 10, no. 11, 2018, doi: 10.3390/polym10111237.

[89] D. E. Fenton, J. M. Parker, and P. V. Wright, "Complexes of alkali metal ions with poly(ethylene oxide)," *Polymer*, vol. 14, no. 11, p. 589, 1973, doi: 10.1016/0032-3861(73)90146-8.

[90] S. B. Aziz, T. J. Woo, M.F.Z. Kadir, and H. M. Ahmed, "A conceptual review on polymer electrolytes and ion transport models," *Journal of Science: Advanced Materials and Devices*, vol. 3, no. 1, pp. 1–17, 2018, doi: 10.1016/j.jsamd.2018.01.002.

[91] A. Arya and A. L. Sharma, "Insights into the use of polyethylene oxide in energy storage/conversion devices: a critical review," *Journal of Physics D: Applied Physics*, vol. 50, no. 44, p. 443002, 2017, doi: 10.1088/1361-6463/aa8675.

[92] K. Nie *et al.,* "Increasing Poly(ethylene oxide) Stability to 4.5 V by Surface Coating of the Cathode," *ACS Energy Letters*, vol. 5, no. 3, pp. 826–832, 2020, doi: 10.1021/acsenergylett.9b02739.

[93] L. Meabe, N. Goujon, C. Li, M. Armand, M. Forsyth, and D. Mecerreyes, "Single-Ion Conducting Poly(Ethylene Oxide Carbonate) as Solid Polymer Electrolyte for Lithium Batteries," *Batteries & Supercaps*, vol. 3, no. 1, pp. 68–75, 2020, doi: 10.1002/batt.201900119.

[94] K. Pożyczka, M. Marzantowicz, J. R. Dygas, and F. Krok, "IONIC CONDUCTIVITY AND LITHIUM TRANSFERENCE NUMBER OF POLY(ETHYLENE OXIDE):LiTFSI SYSTEM," *Electrochimica Acta*, vol. 227, pp. 127–135, 2017, doi: 10.1016/j.electacta.2016.12.172.

[95] T. N. T. Phan, S. Issa, and D. Gigmes, "Poly(ethylene oxide)-based block copolymer electrolytes for lithium metal batteries," *Polym. Int.*, vol. 68, no. 1, pp. 7–13, 2019, doi: 10.1002/pi.5677.

[96] V. Aravindan and P. Vickraman, "Characterization of SiO2 and Al2O3 incorporated PVdF-HFP based composite polymer electrolytes with LiPF3(CF3CF2)3," *J. Appl. Polym. Sci.*, vol. 108, no. 2, pp. 1314–1322, 2008, doi: 10.1002/app.27824.

[97] J. H. Cha, P. N. Didwal, J. M. Kim, D. R. Chang, and C.-J. Park, "Poly(ethylene oxide)-based composite solid polymer electrolyte containing Li7La3Zr2O12 and poly(ethylene glycol) dimethyl ether," *Journal of Membrane Science*, vol. 595, p. 117538, 2020, doi: 10.1016/j.memsci.2019.117538.

[98] L. Chen, Y. Li, S.-P. Li, L.-Z. Fan, C.-W. Nan, and J. B. Goodenough, “PEO/garnet composite electrolytes for solid-state lithium batteries: From “ceramic-in-polymer” to “polymer-in-ceramic”,” *Nano Energy*, vol. 46, pp. 176–184, 2018, doi: 10.1016/j.nanoen.2017.12.037.

[99] B. Chen *et al.,* “A new composite solid electrolyte PEO/Li10GeP2S12/SN for all-solid-state lithium battery,” *Electrochimica Acta*, vol. 210, pp. 905–914, 2016, doi: 10.1016/j.electacta.2016.06.025.

[100] S. H.-S. Cheng *et al.,* “Electrochemical performance of all-solid-state lithium batteries using inorganic lithium garnets particulate reinforced PEO/LiClO4 electrolyte,” *Electrochimica Acta*, vol. 253, pp. 430–438, 2017, doi: 10.1016/j.electacta.2017.08.162.

[101] J.-H. Choi, C.-H. Lee, J.-H. Yu, C.-H. Doh, and S.-M. Lee, “Enhancement of ionic conductivity of composite membranes for all-solid-state lithium rechargeable batteries incorporating tetragonal Li7La3Zr2O12 into a polyethylene oxide matrix,” *Journal of Power Sources*, vol. 274, pp. 458–463, 2015, doi: 10.1016/j.jpowsour.2014.10.078.

[102] F. Croce, G. B. Appetecchi, L. Persi, and B. Scrosati, “Nanocomposite polymer electrolytes for lithium batteries,” *Nature*, vol. 394, no. 6692, pp. 456–458, 1998, doi: 10.1038/28818.

[103] B. Liang *et al.,* “Preparation and characterization of PEO-PMMA polymer composite electrolytes doped with nano-Al2O3,” *Electrochimica Acta*, vol. 169, pp. 334–341, 2015, doi: 10.1016/j.electacta.2015.04.039.

[104] Y.-C. Jung, S.-M. Lee, J.-H. Choi, S. S. Jang, and D.-W. Kim, “All Solid-State Lithium Batteries Assembled with Hybrid Solid Electrolytes,” *J. Electrochem. Soc.*, vol. 162, no. 4, A704-A710, 2015, doi: 10.1149/2.0731504jes.

[105] I. Villaluenga *et al.,* “Compliant glass-polymer hybrid single ion-conducting electrolytes for lithium batteries,” *Proceedings of the National Academy of Sciences*, vol. 113, no. 1, pp. 52–57, 2016, doi: 10.1073/pnas.1520394112.

[106] N. Wu *et al.,* “Enhanced Surface Interactions Enable Fast Li+ Conduction in Oxide/Polymer Composite Electrolyte,” *Angewandte Chemie International Edition in English*, vol. 59, no. 10, pp. 4131–4137, 2020, doi: 10.1002/anie.201914478.

[107] M. T. Irwin, R. J. Hickey, S. Xie, S. So, F. S. Bates, and T. P. Lodge, “Structure–Conductivity Relationships in Ordered and Disordered Salt-Doped Diblock Copolymer/Homopolymer Blends,” *Macromolecules*, vol. 49, no. 18, pp. 6928–6939, 2016, doi: 10.1021/acs.macromol.6b01553.

[108] Y. Cui *et al.,* “Enhancement of Nafion® based membranes for direct methanol fuel cell applications through the inclusion of ammonium-X zeolite fillers,” *Journal of*

Power Sources, vol. 294, pp. 369–376, 2015, doi: 10.1016/j.jpowsour.2015.06.078.

[109] Y. Cui *et al.,* “Porous silicon-aluminium oxide particles functionalized with acid moieties: An innovative filler for enhanced Nafion®-based membranes of direct methanol fuel cell,” *Journal of Power Sources*, vol. 403, pp. 118–126, 2018, doi: 10.1016/j.jpowsour.2018.09.090.

[110] I. Nicotera, C. Simari, M. Agostini, A. Enotiadis, and S. Brutti, “A Novel Li + - Nafion®-Sulfonated Graphene Oxide Membrane as Single Lithium-Ion Conducting Polymer Electrolyte for Lithium Batteries,” *J. Phys. Chem. C*, vol. 123, no. 45, pp. 27406–27416, 2019, doi: 10.1021/acs.jpcc.9b08826.

[111] H. Y. Liang, X. P. Qiu, S. C. Zhang, W. T. Zhu, and L. Q. Chen, “Study of lithiated Nafion® ionomer for lithium batteries,” *Journal of Applied Electrochemistry*, vol. 34, no. 12, pp. 1211–1214, 2004, doi: 10.1007/s10800-004-1767-0.

[112] J. Gao *et al.,* “Lithiated Nafion® as polymer electrolyte for solid-state lithium sulfur batteries using carbon-sulfur composite cathode,” *Journal of Power Sources*, vol. 382, pp. 179–189, 2018, doi: 10.1016/j.jpowsour.2018.01.063.

[113] A. S. Istomina *et al.,* “Li-Nafion® Membrane Plasticised with Ethylene Carbonate/Sulfolane: Influence of Mixing Temperature on the Physicochemical Properties,” *Polymers*, vol. 13, no. 7, p. 1150, 2021, doi: 10.3390/polym13071150.

[114] Y. Shi, C. Wu, L. Li, and J. Yang, “A Lithiated Perfluorinated Sulfonic Acid Polymer Electrolyte for Lithium-Oxygen Batteries,” *J. Electrochem. Soc.*, vol. 164, no. 9, A2031-A2037, 2017, doi: 10.1149/2.1281709jes.

[115] D. H. Kim *et al.,* “Infiltration of Solution-Processable Solid Electrolytes into Conventional Li-Ion-Battery Electrodes for All-Solid-State Li-Ion Batteries,” *Nano Letters*, vol. 17, no. 5, pp. 3013–3020, 2017, doi: 10.1021/acs.nanolett.7b00330.

[116] Y. Liu, S. Gorgutsa, C. Santato, and M. Skorobogatiy, “Flexible, Solid Electrolyte-Based Lithium Battery Composed of LiFePO 4 Cathode and Li 4 Ti 5 O 12 Anode for Applications in Smart Textiles,” *J. Electrochem. Soc.*, vol. 159, no. 4, A349-A356, 2012, doi: 10.1149/2.020204jes.

[117] F. Hao, F. Han, Y. Liang, C. Wang, and Y. Yao, “Architectural design and fabrication approaches for solid-state batteries,” *MRS Bulletin*, vol. 43, no. 10, pp. 775–781, 2018, doi: 10.1557/mrs.2018.211.

[118] N. J. Dudney, W. C. West, and J. Nanda, *Handbook of solid state batteries*. New Jersey, London, Singapore, Beijing, Shanghai, Hong Kong, Taipei, Chennai, Tokyo: WORLD SCIENTIFIC, 2016.

[119] E. Barsoukov and J. R. Macdonald, *Impedance spectroscopy: Theory, experiment, and applications.* [Online]. Available: http://search.ebscohost.com/login.aspx?direct=

true&scope=site&db=nlebk&db=nlabk&AN=128515

[120] S. Koombhongse, W. Liu, and D. H. Reneker, “Flat polymer ribbons and other shapes by electrospinning,” *J. Polym. Sci. B Polym. Phys.*, vol. 39, no. 21, pp. 2598–2606, 2001, doi: 10.1002/polb.10015.

[121] T. S. Pathan, M. Rashid, M. Walker, W. D. Widanage, and E. Kendrick, “Active formation of Li-ion batteries and its effect on cycle life,” *J. Phys. Energy*, vol. 1, no. 4, p. 44003, 2019, doi: 10.1088/2515-7655/ab2e92.

[122] D. Y. Wang *et al.,* “A Systematic Study of Electrolyte Additives in Li[Ni 1/3 Mn 1/3 Co 1/3]O 2 (NMC)/Graphite Pouch Cells,” *J. Electrochem. Soc.*, vol. 161, no. 12, A1818-A1827, 2014, doi: 10.1149/2.0511412jes.

[123] C. Meyer, H. Bockholt, W. Haselrieder, and A. Kwade, “Characterization of the calendering process for compaction of electrodes for lithium-ion batteries,” *Journal of Materials Processing Technology*, vol. 249, pp. 172–178, 2017, doi: 10.1016/j.jmatprotec.2017.05.031.

[124] N. Yabuuchi and T. Ohzuku, “Novel lithium insertion material of LiCo1/3Ni1/3Mn1/3O2 for advanced lithium-ion batteries,” *Journal of Power Sources*, 119-121, pp. 171–174, 2003, doi: 10.1016/S0378-7753(03)00173-3.

[125] M. Frankenberger, M. Singh, A. Dinter, and K.-H. Pettinger, “EIS Study on the Electrode-Separator Interface Lamination,” *Batteries*, vol. 5, no. 4, p. 71, 2019, doi: 10.3390/batteries5040071.

[126] M. Frankenberger, M. Singh, A. Dinter, S. Jankowksy, A. Schmidt, and K.-H. Pettinger, “Laminated Lithium Ion Batteries with improved fast charging capability,” *Journal of Electroanalytical Chemistry*, vol. 837, pp. 151–158, 2019, doi: 10.1016/j.jelechem.2019.02.030.

[127] G. Fourche, “An overview of the basic aspects of polymer adhesion. Part I: Fundamentals,” *Polymer Engineering and Science*, vol. 35, no. 12, pp. 957–967, 1995, doi: 10.1002/pen.760351202.

[128] H. Lee, “Electrospun Nanofiber-Coated Membrane Separators for Lithium-Ion Batteries,” *Ph.D. Thesis*, 2013.

[129] Z. Hou, J. Zhang, W. Wang, Q. Chen, B. Li, and C. Li, “Towards high-performance lithium metal anodes via the modification of solid electrolyte interphases,” *Journal of Energy Chemistry*, vol. 45, pp. 7–17, 2020, doi: 10.1016/j.jechem.2019.09.028.

[130] R. Wang, W. Cui, F. Chu, and F. Wu, “Lithium metal anodes: Present and future,” *Journal of Energy Chemistry*, vol. 48, pp. 145–159, 2020, doi: 10.1016/j.jechem.2019.12.024.

[131] J. Qian *et al.,* “Anode-Free Rechargeable Lithium Metal Batteries,” *Adv. Funct.*

Mater., vol. 26, no. 39, pp. 7094–7102, 2016, doi: 10.1002/adfm.201602353.

[132] C. Hwang *et al.,* “A Three-Dimensional Nano-web Scaffold of Ferroelectric Beta-PVDF Fibers for Lithium Metal Plating and Stripping,” *ACS Applied Materials & Interfaces*, vol. 12, no. 26, pp. 29235–29241, 2020, doi: 10.1021/acsami.0c05065.

[133] C. Dong *et al.,* “A robust interface enabled by electrospun membrane with optimal resistance in lithium metal batteries,” *Journal of Energy Chemistry*, vol. 55, pp. 1–9, 2021, doi: 10.1016/j.jechem.2020.06.060.

[134] X. Xu *et al.,* “The suppression of lithium dendrite growth in lithium sulfur batteries: A review,” *Journal of Energy Storage*, vol. 13, pp. 387–400, 2017, doi: 10.1016/j.est.2017.07.031.

List of publications

Manuscripts

1. B. C. Springer, M. Frankenberger, and K.-H. Pettinger, *Lamination of Separators to Electrodes using Electrospinning, PloS one*, vol. 15, no. 1, e0227903, 2020, doi: 10.1371/journal.pone.0227903.

Conference talks

1. *Electrospinning: An interesting method,* presented at FSTORE project workshop 2019, 7th of October 2019, Český Krumlov, Czech Republic
2. *Enabling Lamination for improved battery production and performance using Electrospinning,* presented at BatteryWorld 2020, 29th of January 2020, Munich, Germany

Poster presentations

1. B. C. Springer, M. Amjad, K.-H. Pettinger*; Influence of rotational speed of a drum collector electrospinning setup on polymer electrolytes*; Poster at IBPC 2019, 4th to 6th of November 2019, Braunschweig, Germany
2. B. C. Springer, M. Frankenberger, K.-H. Pettinger*; Electrospinning as production technology: Enabling Lamination for improved battery production and performance using electrospinning*; Poster at Dresden Battery Days 2019, 23rd to 25th of September 2019, Dresden, Germany

Appendix

T-cells

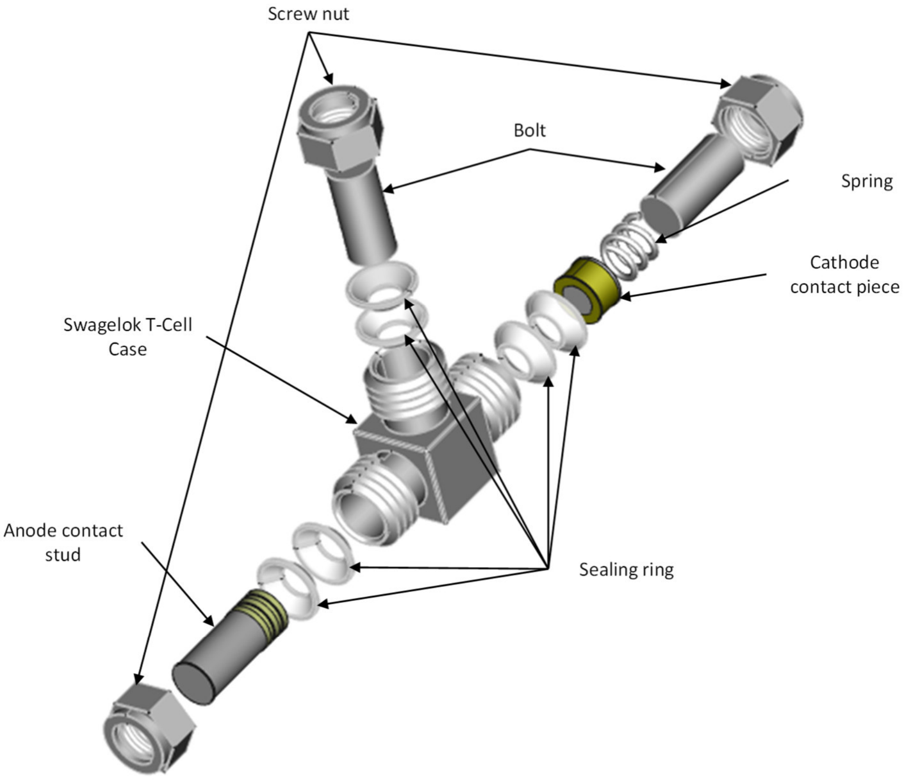

Figure 50 Exploded schematic of a T-cell used in this thesis

For cyclovoltammetry measurements of cells with either solution casted or electrospun electrolytes, Swagelok T-cells have been used. These cells are well known for half-cell measurements used in electrode characterization with liquid electrolytes and pose a good cell setup for three electrode measurements.

In this thesis, a three-electrode setup is not used, since the application of the reference electrode to the solid electrolyte is, with a classical T-cell, impracticable. Nevertheless, this cell design was chosen, since it provided better data quality for cyclovoltammetry compared to coin cells.

A schematic of the used T-cells can be seen in Figure 50. The cell basically consists of the

T-cell case, anode and cathode contacting parts and the reference contacting parts. As already mentioned, the used cells have been modified, in this case a reference electrode was not used. The bolt, sealing and screw on the reference side was only used to seal the casing shut. Within the cell case, electric isolation was used to prevent short circuiting. On the anode side, lithium metal was placed on the isolated part of the anode contact stud. The lithium was contacted by a small part of the metallic bolt which was surrounded by isolation. Onto the lithium, a solution casted electrolyte membrane was or, in case of an electrospun electrolyte, the cathode which was previously coated with the electrolyte was placed and contacted by the cathode contact piece. To provide a desired mechanical pressure to the cell, a spring was used between the cathode contacting piece and the bolt.

Area loadings of the used cathodes

The area loadings have been calculated by punching areas of the cathodes which are not coated with electrolyte by electrospinning. The samples are punched using a 14 mm ELCELL punch. Additionally, 5 aluminum samples (without any coating) were punched to enable calculating the cathode coating mass. The area loading is than calculated by multiplying the cathode coating mass with the specific capacity for the used active material (NMC_{111}; 155 mAh/g according to the data sheet given by the supplier) and the weight percentage of the active mass within the coating (0.7513 wt%; see Table 4), divided by the area of the electrode. The resulting area loadings can be found in Table 16.

Electrode sheet number	Area loading Sample 1	Area loading Sample 2	Area loading Sample 3	Average area loading (Standard deviation)
#18	0.7544 mAh/cm²	0.7612 mAh/cm²	0.7605 mAh/cm²	0.7587 (± 0.0037) mAh/cm²
#21	0.7272 mAh/cm²	0.8187 mAh/cm²	0.8263 mAh/cm²	0.7907 (± 0.0552) mAh/cm²
#26	0.7779 mAh/cm²	0.7680 mAh/cm²	0.7203 mAh/cm²	0.7554 (± 0.0308) mAh/cm²

Table 16 Area loadings of used cathodes

Additional Impedance data

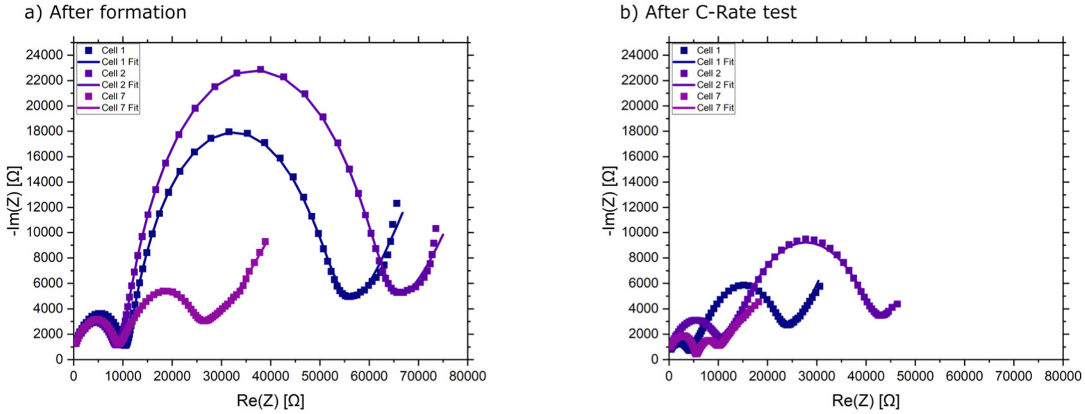

Figure 51 Impedance data with fits for cell series #17

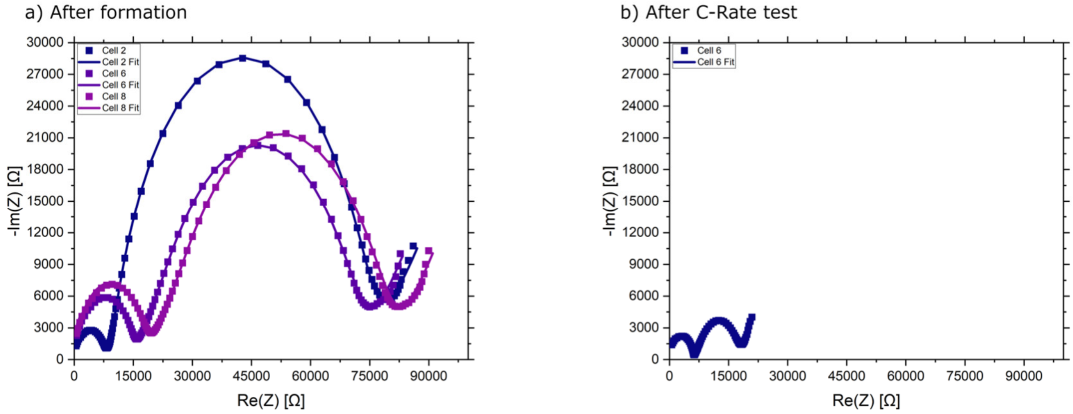

Figure 52 Impedance data with fits for cell series #24

Solution stability

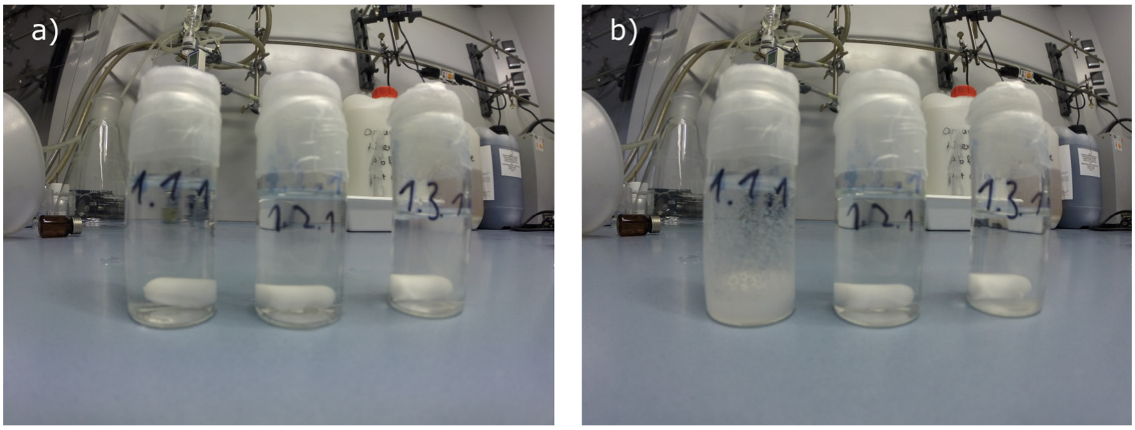

Figure 53 Solutions 1.1.1, 1.2.1 and 1.3.1 a) directly after stirring and b) after resting for 12 h at room temperature

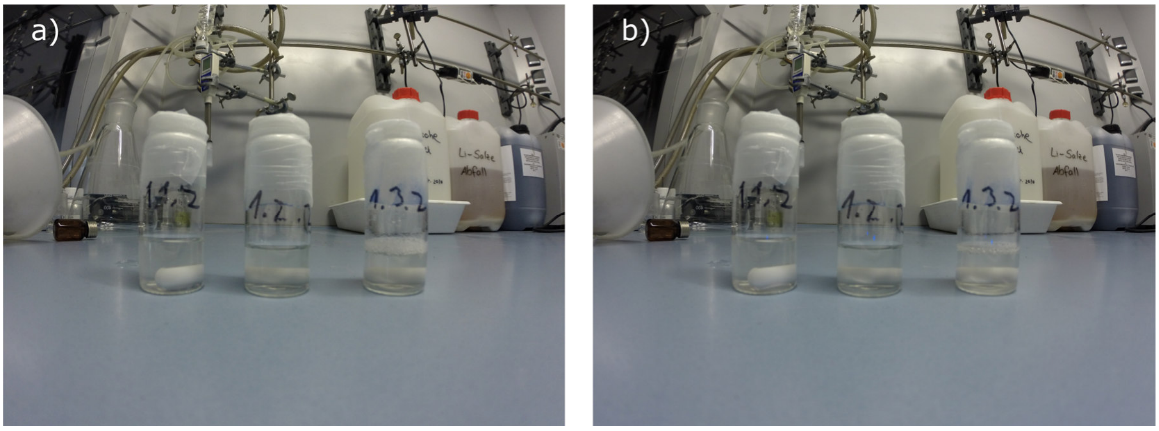

Figure 54 Solutions 1.1.2, 1.2.2 and 1.3.2 a) directly after stirring and b) after resting for 12 h at room temperature

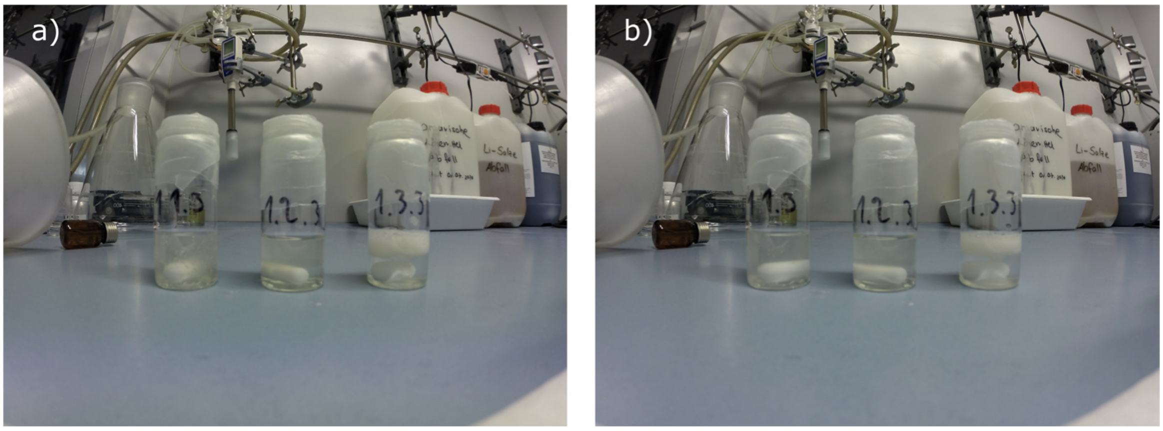

Figure 55 Solutions 1.1.3, 1.2.3 and 1.3.3 a) directly after stirring and b) after resting for 12 h at room temperature

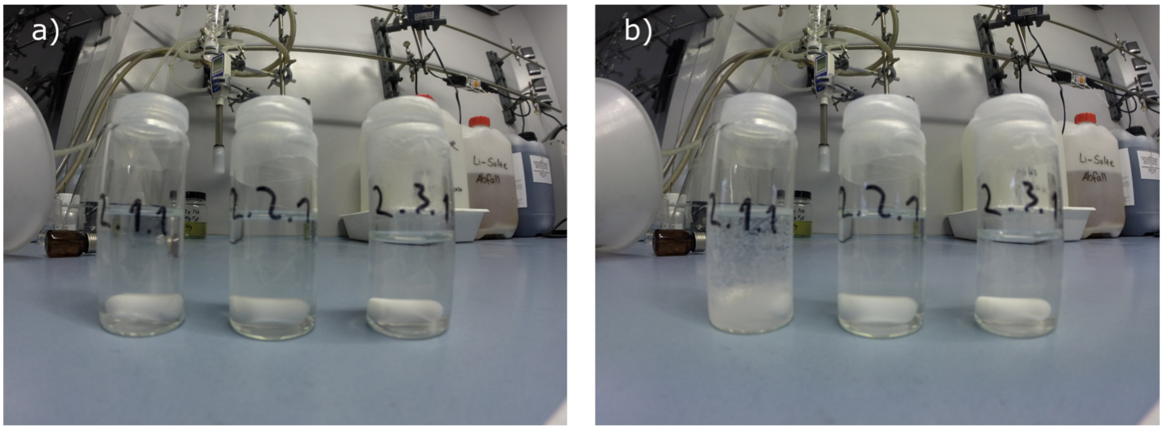

Figure 56 Solutions 2.1.1, 2.2.1 and 2.3.1 a) directly after stirring and b) after resting for 12 h at room temperature

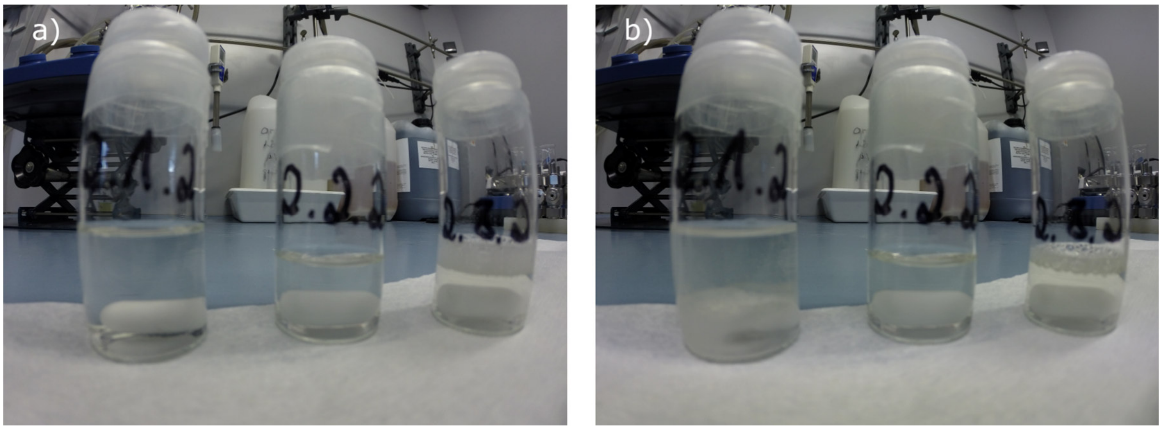

Figure 57 Solutions 2.1.2, 2.2.2 and 2.3.2 a) directly after stirring and b) after resting for 12 h at room temperature

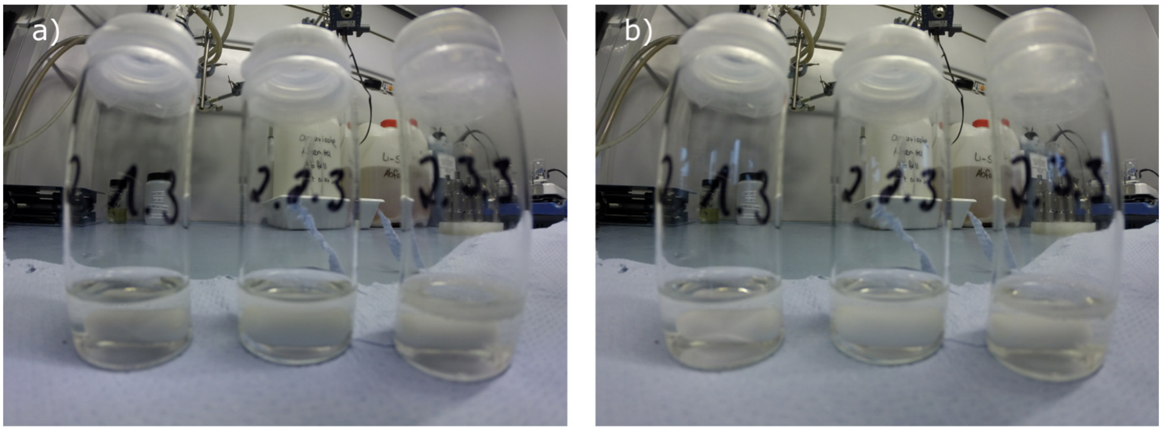

Figure 58 Solutions 2.1.3, 2.2.3 and 2.3.3 a) directly after stirring and b) after resting for 12 h at room temperature

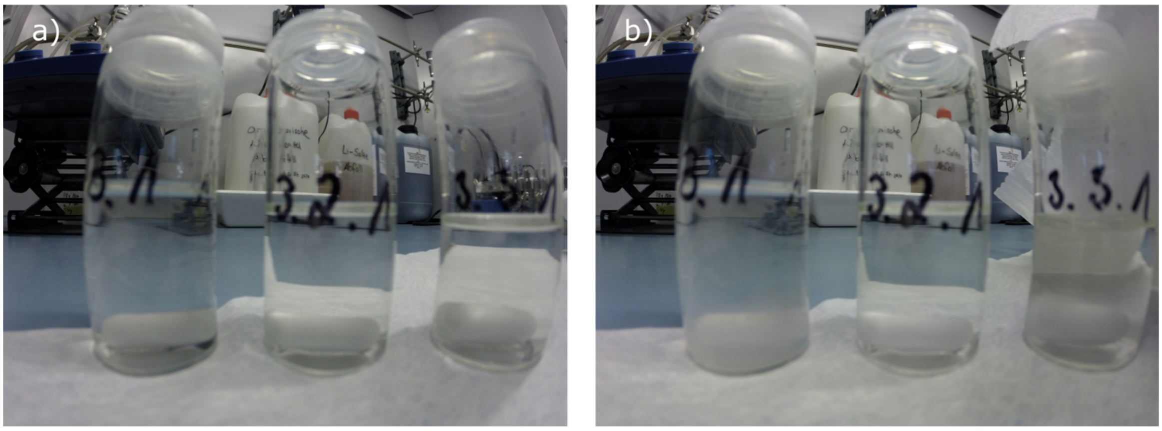

Figure 59 Solutions 3.1.1, 3.2.1 and 3.3.1 a) directly after stirring and b) after resting for 12 h at room temperature

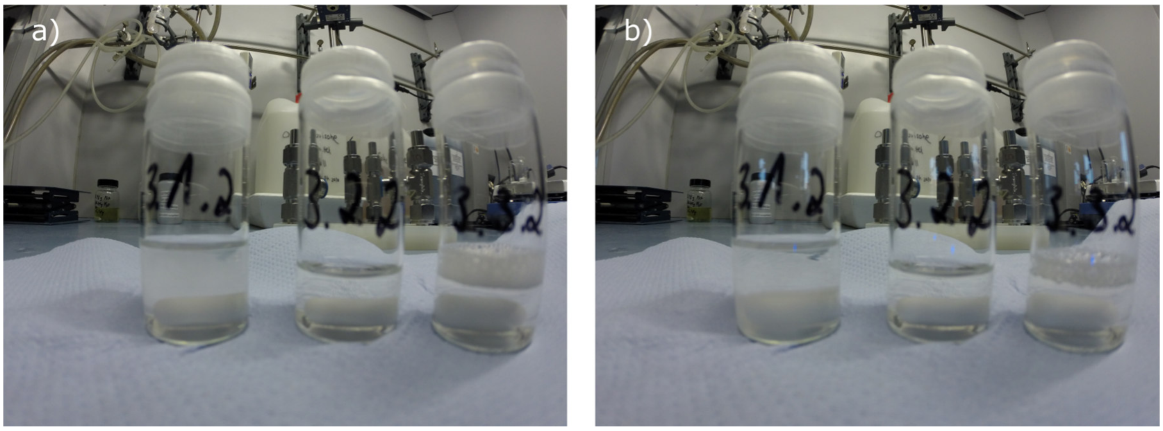

Figure 60 Solutions 3.1.2, 3.2.2 and 3.3.2 a) directly after stirring and b) after resting for 12 h at room temperature

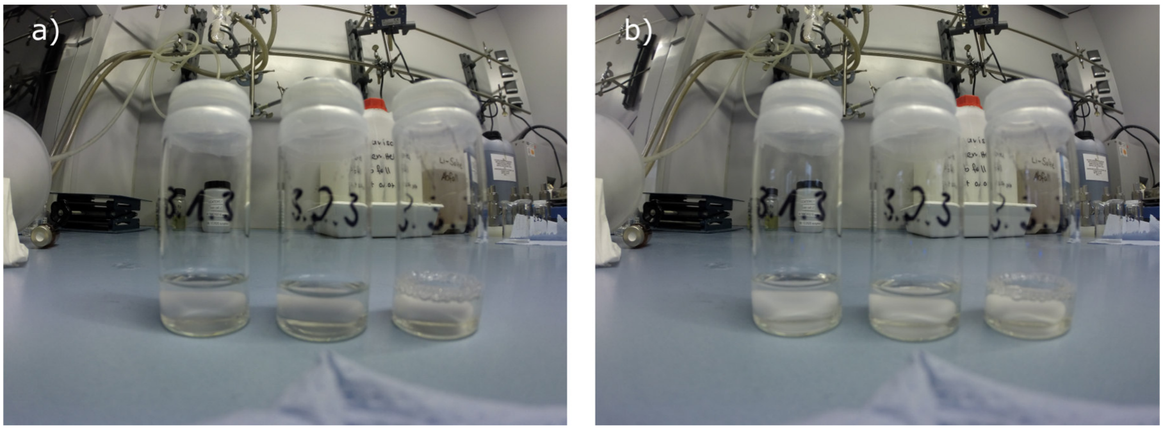

Figure 61 Solutions 3.1.3, 3.2.3 and 3.3.3 a) directly after stirring and b) after resting for 12 h at room temperature

Error calculation for transference numbers

$$\Delta t^{+} = \left\lvert \frac{\partial t^{+}}{\partial I_{SSC}} \right\rvert \cdot \Delta I_{SSC} + \left\lvert \frac{\partial t^{+}}{\partial \Delta V} \right\rvert \cdot \Delta V + \left\lvert \frac{\partial t^{+}}{\partial R_0} \right\rvert \cdot \Delta R_0 + \left\lvert \frac{\partial t^{+}}{\partial R_{SSC}} \right\rvert \cdot \Delta R_{SSC} + \left\lvert \frac{\partial t^{+}}{\partial I_0} \right\rvert \cdot \Delta I_0$$	*Eq. 8*

$$\frac{\partial t^{+}}{\partial I_{SSC}} = \frac{\Delta V(\Delta V - R_0 I_0)}{I_0(\Delta V - R_{SSC} I_{SSC})^2}$$	*Eq. 9*
$$\frac{\partial t^{+}}{\partial \Delta V} = \frac{I_{SSC}(R_0 I_0 - R_{SSC} I_{SSC})}{I_0(\Delta V - R_{SSC} I_{SSC})^2}$$	*Eq. 10*
$$\frac{\partial t^{+}}{\partial I_0} = \frac{I_{SSC} \Delta V}{{I_0}^2(R_{SSC} I_{SSC} - \Delta V)}$$	*Eq. 11*

$\frac{\partial t^{+}}{\partial R_0} = \frac{I_{SSC}}{R_{SSC} I_{SSC} - \Delta V}$	*Eq. 12*
$\frac{\partial t^{+}}{\partial R_{SSC}} = \frac{{I_{SSC}}^2 (\Delta V - R_0 I_0)}{I_0 (\Delta V - R_{SSC} I_{SSC})^2}$	*Eq. 13*

Additional SEM data of PFSA-based electrospun samples

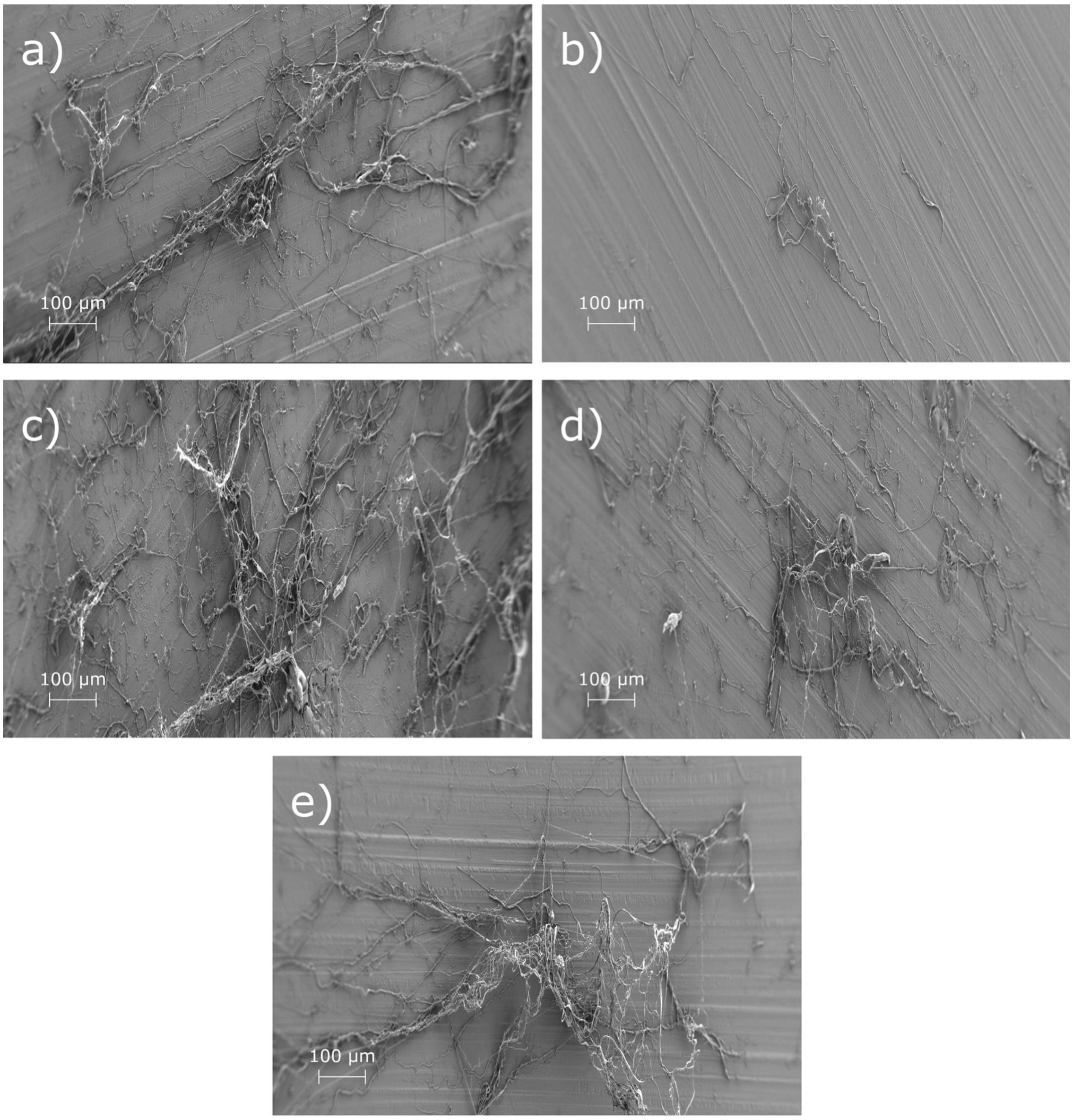

Figure 62 Additional SEM data for electrospun samples for solution 1.2.2

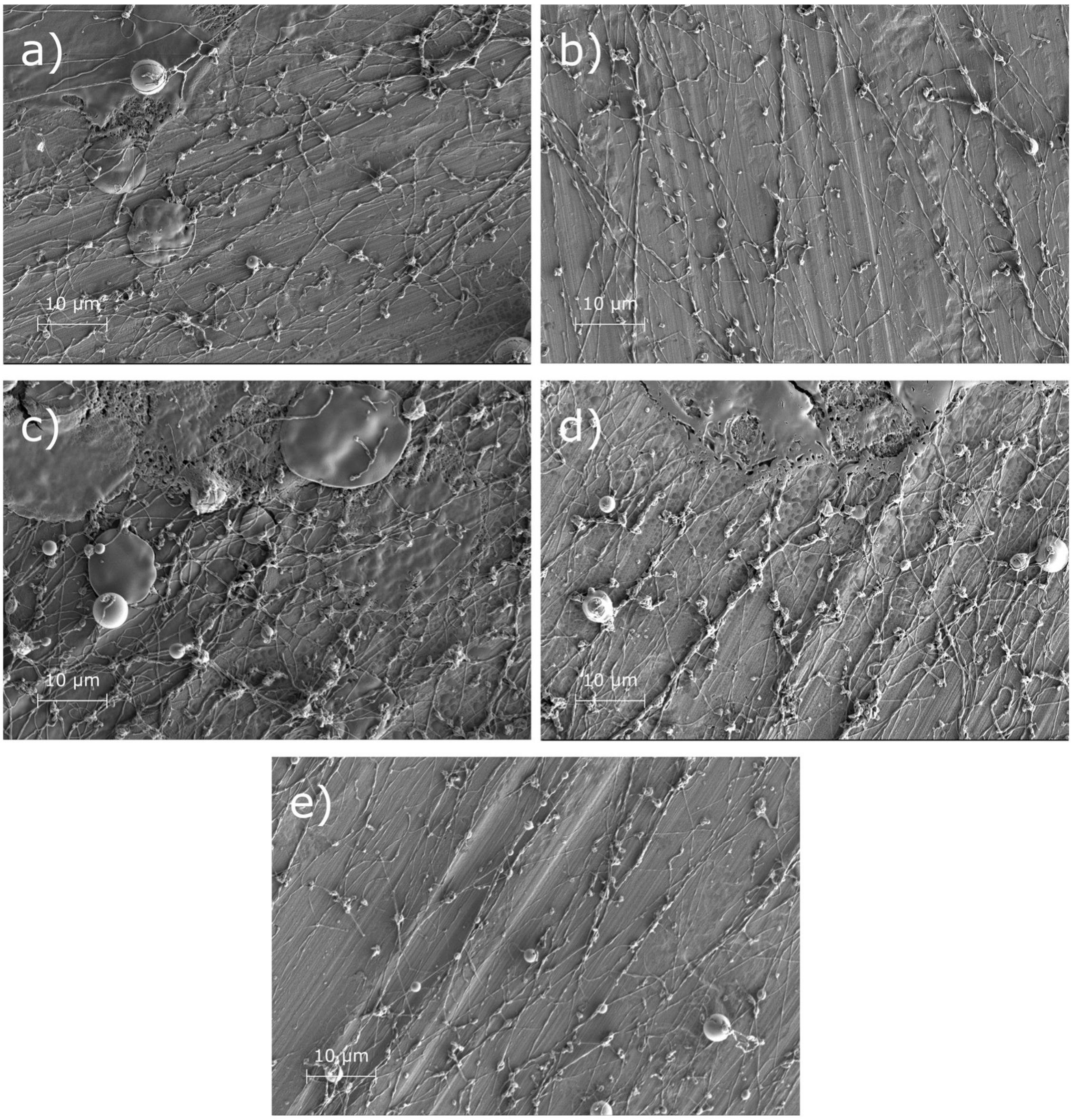

Figure 63 Additional SEM data for electrospun samples for solution 2.2.1

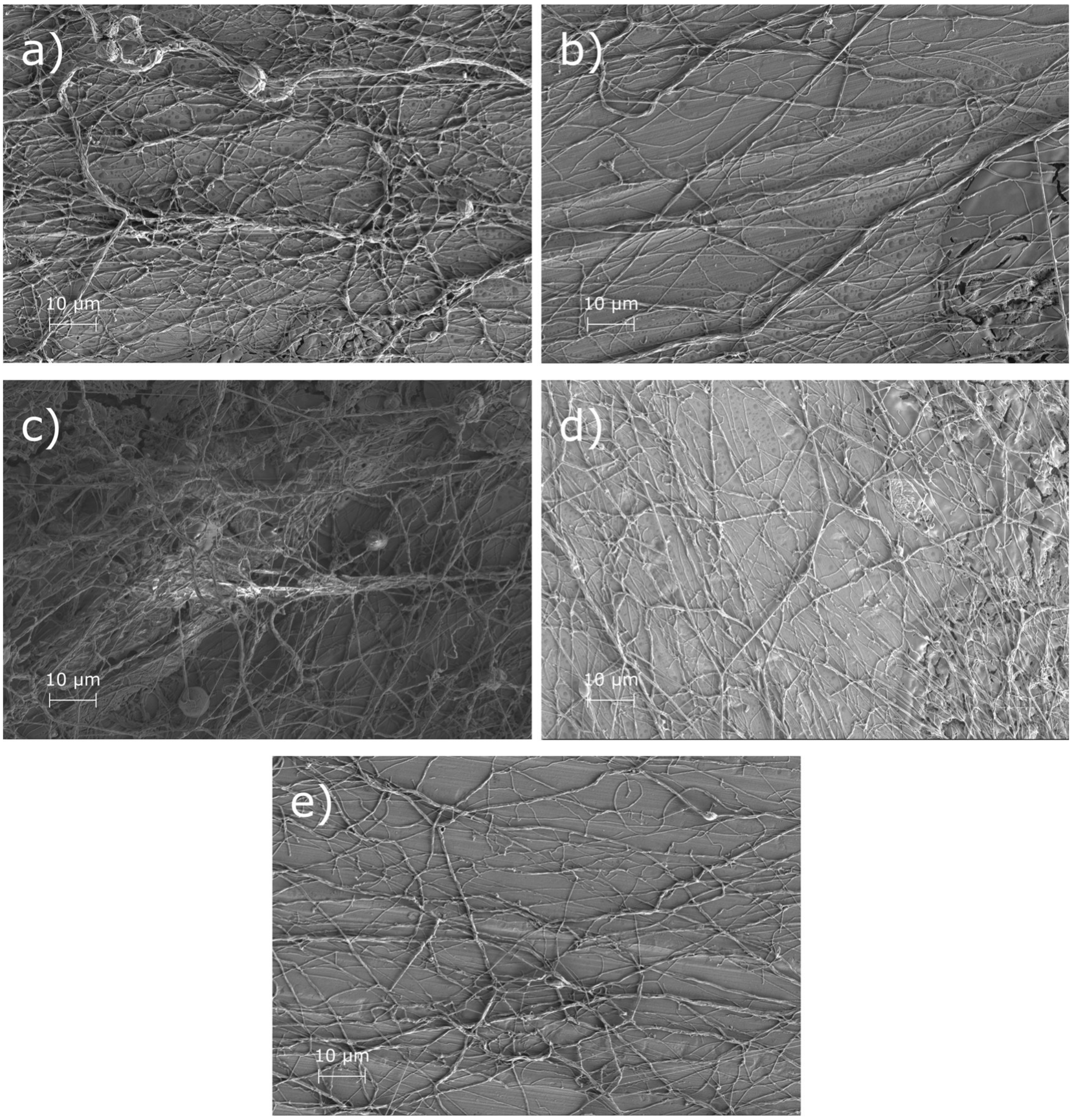

Figure 64 Additional SEM data for electrospun samples for solution 2.2.2

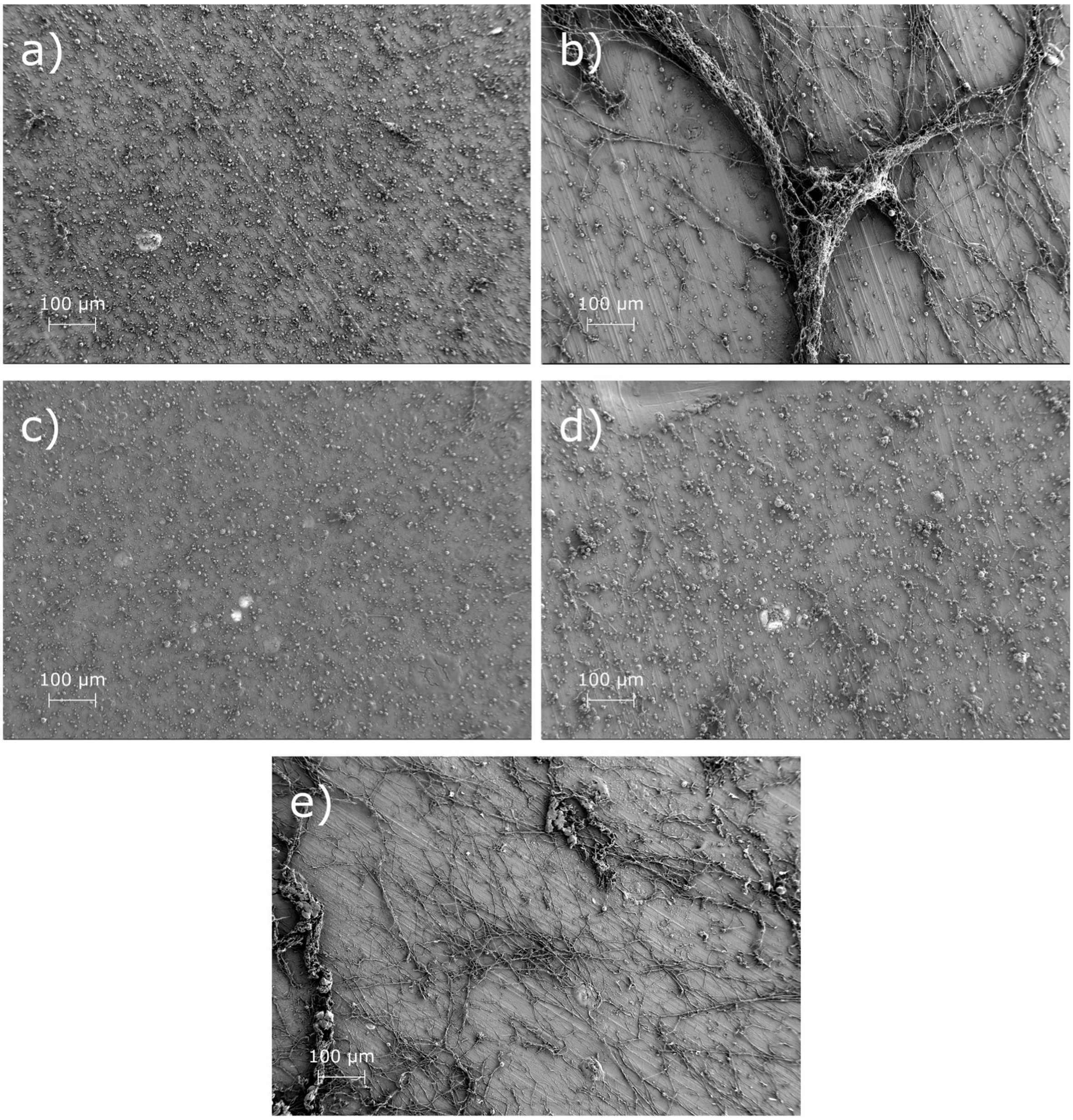

Figure 65 Additional SEM data for electrospun samples for solution 2.2.3